6-25-2010

The sintering and stability of catalytic nano-particles

Andrew DeLaRiva

Andrew DeLaRiva

Candidate

Department of Chemical and Nuclear Engineering

Department

This dissertation is approved, and it is acceptable in quality and form for publication:

Approved by the Dissertation Committee:

, Chairperson

THE SINTERING AND STABILTY OF CATALYTIC NANO-PARTICLES

BY

Andrew DeLaRiva

B.S., Chemical Engineering, University of New Mexico, 2005

DISSERTATION

Submitted in Partial Fulfillment of the
Requirements for the Degree of

Doctor of Philosophy

Engineering

The University of New Mexico
Albuquerque, New Mexico

December, 2009

DEDICATION

To my parents, Martin and Mayra, and my brothers David, Phillip, and Noel, this wouldn't have been possible without your support.

-Andrew

ACKNOWLEDGEMENTS

I would like to thank my advisor, Abhaya Datye, for all the support and guidance. I would also like to thank the catalysis group: Hien Pham, Levi Houk, Patrick Burton, Eric Peterson, Ron Goeke, Sivakumar Challa, and Barr Halevi. I would also like to thank former group members: John Gabaldon, Ayman Krarim, Thomas Hansen, and Travis Conant for their continued help and guidance. Thanks to Paul Fanson of Toyota and Karl Karas of Delphi for their support, helpful discussions, and supplied catalyst samples. Thanks also to the entire characterization group in research in development at Haldor Topsøe A/S, most notably Stig Helveg, Poul Hansen, and Jens Sehested, for mentorship and guidance. Special thanks to the company Haldor Topsøe A/S for use of their facilities for a six month period. Thanks to Edward Kunkes from the University of Wisconsin for synthesis of carbon catalyst samples. Special thanks to Lawrence Allard at ORNL for his time and expertise in ACEM.

I would also like to thank the facilities for equipment use: UNM microscopy facilities supported by NSF/EPSCOR, NSF/NNIN grants and the Department of Earth and Planetary Sciences; The Advanced Microscopy Lab at Oak Ridge National Labs. I would like to thank NSF for aid with the NSF Partnership for International Research and Education (PIRE) OISE-0730277, IREE, and IGERT Fellowship for financial support.

Finally I would like to thank my committee members Plamen Atanassov, Tim Ward, and Adrian Brearley.

THE SINTERING AND STABILTY OF CATALYTIC NANO-PARTICLES

BY

Andrew DeLaRiva

ABSTRACT OF DISSERTATION

Submitted in Partial Fulfillment of the
Requirements for the Degree of

Doctor of Philosophy

Engineering

The University of New Mexico
Albuquerque, New Mexico

December, 2009

The Sintering and Stability of Catalytic Nano-Particles

by

Andrew DeLaRiva

B.S., Chemical Engineering, University of New Mexico, 2005

Ph.D, Engineering, University of New Mexico, 2009

ABSTRACT

Studies were performed on three different catalysts in order to determine their stability and sintering behavior. Pd deposited on a flat single crystal substrate made of Al_2O_3 was characterized to determine if the mechanism of Ostwald Ripening was solely dominated by vapor phase transport of metal atoms. The atoms emitted could be determined by the rate of evaporation and an attempt was then made in order to relate the rates of emission to sintering (instability of nanoparticles). It was found that the rates of emission did not fully reflect vapor phase transport (direct evaporation). The particle-support interaction was increasing the rate of evaporation leading to the belief that adatom diffusion, caused by a weaker bound atom on the support, played a more significant role than vapor phase transport. A powder Pd/Al_2O_3 was also put under similar ageing conditions as the single crystal samples, but relating the two separate systems proved difficult. This was due to the containment of the metal on the support and changes of the powder support through ageing (loss in surface area). Support changes (decrease in the number of sites for particle nucleation) caused by the heat

treatments seemed to also be influencing the sintering behavior. The powder samples were put through two different ageing studies, one with the presence of water vapor and the other without. The presence of water vapor enhanced the rate of sintering due to the interactions with the support and particles, possibly by changing the support morphology or making hydroxyl groups on the metal particle surface or both.

A second catalyst was characterized to establish the affect support structure would have on the stability of nanoparticles. 10wt% of Pt and Re were deposited on two different Carbon supports, Norit and Vulcan Carbon. Norit Carbon was imaged to be highly roughened and as a result had a large surface area ($1000 m^2/g$). The Vulcan Carbon was imaged to be more graphitic and contain two different types of structures, one similar to larger graphitic Carbon particles, and the other to resemble a more roughened structure similar to that of Norit. The Pt and Re species appeared to be homogeneously dispersed on the Norit with both atomic species and nanoparticles. It was seen that the Pt and Re atoms preferred to adsorb onto the areas where the carbon structure appeared have an edge site.

A third catalyst was used for in-situ TEM studies to clearly identify and record the exact sintering mechanism at the early stages of exposure to reaction conditions. Previous theory and simulation were in debate on which sintering mechanism dominates and what is the cause, our in-situ studies gave direct evidence of the sintering mechanism taking place under a gaseous and heated environment. A ~14wt%Ni on $MgAl_2O_4$, used primarily for steam reforming, was put through a series of in-situ TEM experiments under high temperatures (750°C) in the presence of Hydrogen and water vapor 3.6mbar (1:1). It was found by recording images at a fast rate (every 100-200 milliseconds) the

sintering mechanism could be observed and recorded. In the later stages of heating, ~30 minutes after reaching temperature, larger particles (>5nm) were seen to be mobile on the surface, contrary to theory which suggests that larger particle should be immobile. Recorded images and movies taken at the early stages of heating revealed that smaller particles (<3nm) were immobile on the support but could ripen away rapidly. This evidence is also contrary to previous theory that suggested smaller particles would be highly mobile and coalescence once the catalyst is exposed to reaction conditions. Further investigation into the sintering events, revealed that particle adhesion decreases as both time and particle size increase. The loss in adhesion to support in larger particles and larger ratio of interaction for smaller particles, may explain why smaller particles were stable on the support but ripened, and why larger particles were recorded to be mobile.

Future work on flat samples could involve various supports in order to determine which support makes the most stable catalyst and modeling that includes particle-particle interaction could be included. The addition or subtraction of functional groups on a single carbon support could be used as a further probe on how it affects atomic dispersion and adsorption. New in-situ studies performed at atmospheric pressure could be of use as pressures may influence the rate of sintering and the stability of the metal nanoparticles.

Table of Contents

LIST OF FIGURES

LIST OF TABLES

Chapter 1

1 Introduction

1.1 Statement of Research Problem

Maintaining a highly dispersed catalyst is essential in industrial catalysis, as highly dispersed stable metal nanoparticles tend to be more active due to the high amount of active sites. As a catalyst is put under industrial reactive conditions, the surface area may be lost as the small particles grow in size due to sintering. Sintering is one of the most important causes of catalyst deactivation in heterogeneous catalysts as it affects all industrial catalysts, such as automotive exhaust catalysts and catalysts used for the production of hydrogen (used as an energy source).

An increase in understanding of the behavior of catalyst sintering has grown with advancements in technology. Most of the advancements came in the field of microscopy where the catalyst could be observed before and after reaction and in some cases during the reaction itself. Although the field was advanced for its time, limitations in computer technology made it difficult to pin point the exact mechanisms responsible for sintering catalysts. How the support structure was affecting catalyst stability and sintering behavior, along with effects from the gaseous environment, are still under heavy debate as direct observation of small nanoparticles has proven to be difficult. With further advancements in computer technology it is now possible to go beyond the limitations seen by previous researchers and observe catalysts at the atomic scale and under in-situ

conditions with an enhanced microscope resolution. Microscopy analysis of catalyst sintering is imperative in understanding fundamental mechanisms in sintering behavior.

The objective of this research is to on determine how environmental conditions and structure affect the overall stability of a catalyst and its sintering behavior. Three different catalysts will be studied to determine how each is affected by these conditions: Pd/Al_2O_3, PtRe/C, and $Ni/MgAl_2O_4$. It will also be demonstrated that direct observations are imperative in determining the exact sintering mechanism. The research approach will use current advancements in microscopy along with typical catalyst characterization techniques. With further understanding and knowledge in the field of catalyst sintering deactivation, methods can be developed to prevent, stop, or even reverse the deactivation problem.

1.2 Catalysis

A catalyst can be described as the workhorse of the chemical industry, as 85-90% of the chemicals produced are made viz catalytic processes[1]. The catalyst itself augments the chemical reaction rate and makes it more energetically favorable for the reaction to take place without being consumed in the reaction. Because a catalyst makes a reaction go faster and can be selective toward a chemical product, catalytic reactions become greatly important in industrial process. Some of the most well known industrial applications of catalysis are in the pharmaceutical and petroleum industries with products varying from catalytic converters to toothbrushes.

It has been seen over the years as computer technology increases the knowledge in the field of catalysis increases with it. Although the field has been around since the

1800's with ground breaking work by Davy and Berzelius, the understanding is still catching up to the practical uses. As shown by Chorkendorff[1] in the graph below, our knowledge in catalysis has dramatically increased thanks to advancements in computer technology, with understanding now increasing even more rapidly, approaching the knowledge in practical catalysis.

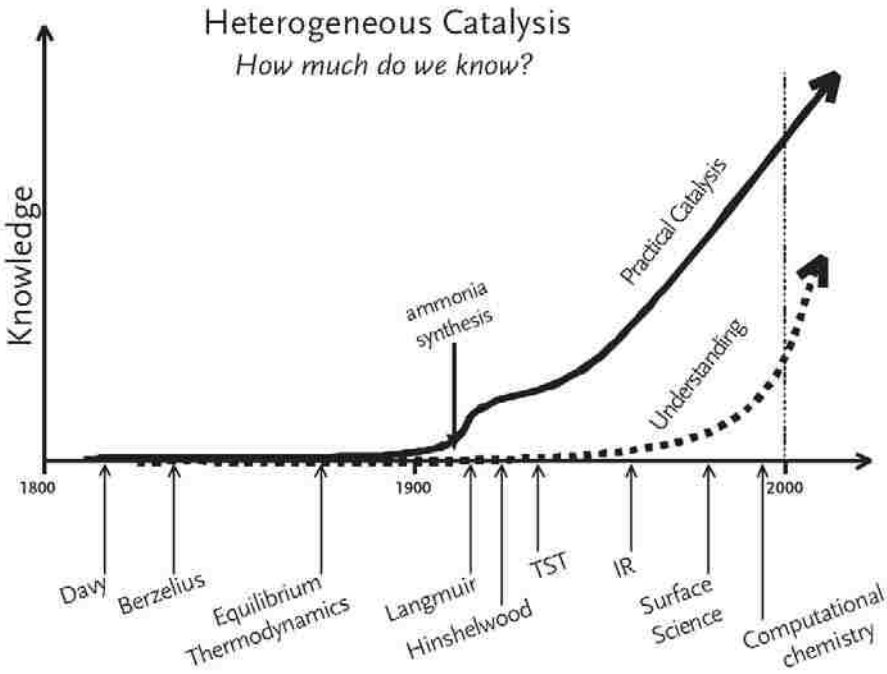

Figure 1 A graph comparing the knowledge and understanding of catalysis vs. practical applications of catlysis over the last 200 years.

1.3 Heterogeneous Catalysis

Catalysis can be broken down into two types: homogenous and heterogeneous catalysis. Homogenous catalysis refers to catalytic processes where both the reactant and the catalyst are in the same phase. This type of catalysis may run into additional steps

encountering a separation process to separate catalyst and product. Heterogeneous catalysis is the catalytic process where the catalyst and the reactant are in different phases; typically the catalyst is a solid with the reactants being a gas or liquid. Heterogeneous catalysis plays a huge role in the production of many industrial products and in many chemical reactions as shown by the examples of catalysts and reactions in the table below. In this dissertation, we will focus solely on heterogeneous catalysts, with the catalyst in the solid phase.

Table 1 A table showing a variety of catalysts used for the described industrial reaction. From Chorkendorff[1].

Reaction	Catalyst
Catalytic cracking of crude oil	Zeolites
Hydrotreating of crude oil	Co–Mo, Ni–Mo, Ni–W (sulfidic form)
Reforming of naphtha (to gasoline)	Pt, Pt–Re, Pt–Ir
Alkylation	H_2SO_4, HF, solid acids
Polymerization of ethylene, propylene, a.o.	Cr, $TiCl_x/MgCl_2$
Ethylene epoxidation to ethylene oxide	Ag
Vinyl chloride (ethylene + Cl_2)	Cu (as chloride)
Steam reforming of methane to CO + H_2	Ni
Water-gas shift reaction	Fe (oxide), Cu–ZnO
Methanation	Ni
Ammonia synthesis	Fe
Ammonia oxidation to NO and HNO_3	Pt–Rh
Acrylonitrile from propylene and ammonia	Bi–Mo, Fe–Sb (oxides)
Hydrogenation of vegetable oils	Ni
Sulfuric acid	V (oxide)
Oxidation of CO & hydrocarbons (car exhaust)	Pt, Pd
Reduction of NOx (in exhaust)	Rh, vanadium oxide

A catalyst lowers the activation energy of a step in a reaction, or it provides an alternative pathway via an intermediate steps that may be more energetically favorable.

A catalyst does not alter the thermodynamics of a reaction. If we take the example of reactants A and B reacting and going to product P, normally without a catalyst participating in the reaction, the reaction would be very slow or not be seen to take place. With a catalyst: (1) A and B can adsorb (chemically or physically) onto the catalyst surface in a spontaneous manner lowering the free energy, (2) react with each other to make a product which in this case has an energy activation barrier (lower than without a catalyst), (3) then desorb in an endothermic process with the catalyst returning to its initial state. Overall the free energy change is no different than if the reaction had taken place without the catalyst, revealing that the catalyst has no effect on the thermodynamic stability or equilibrium. So if a reaction is thermodynamically unfavorable, the reaction will not take place with or without a catalyst. This process can be more easily seen in the diagram below.

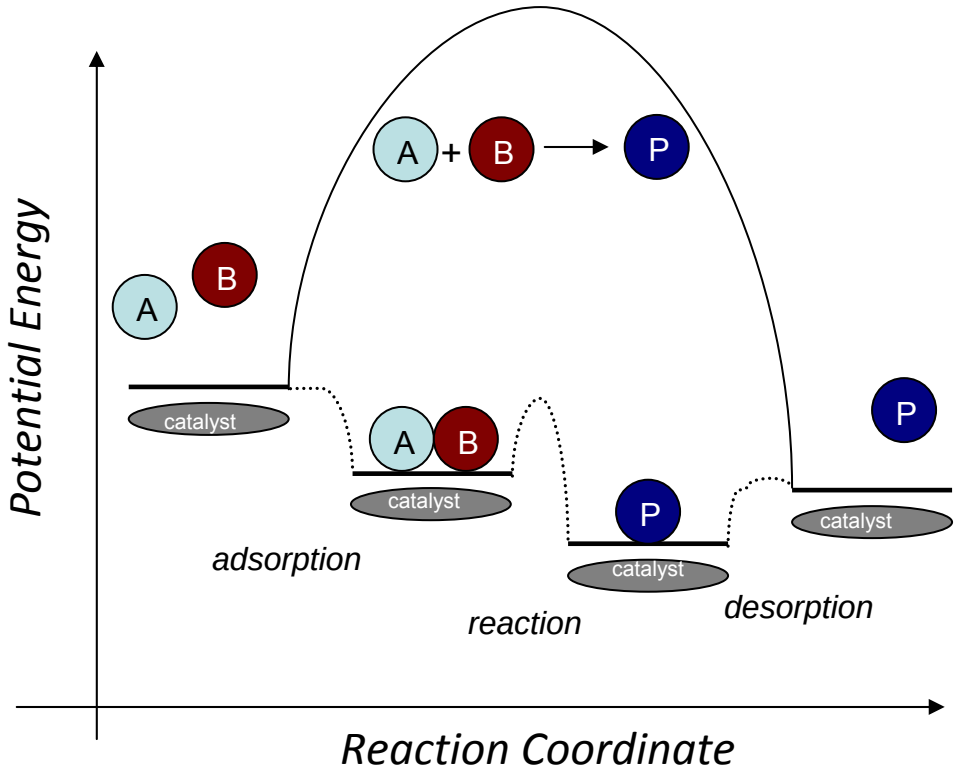

Figure 2 Schematic of a chemical reaction of reactants A and B. The reactants adsorb onto the catalyst surface, react and turn into product P, then desorb as product P leaving the catalyst to participate in an additional reaction. The activation energy barriers are much lower

1.4 The Sintering and Growth of Nanoparticles

Highly dispersed supported nanoparticles on an oxide or non-oxide support have proven to be active for many heterogeneous catalytic processes. Unfortunately the catalyst may be exposed to extremely harsh conditions in order for a reaction to occur. While enduring such harsh conditions the catalyst is susceptible to poisoning, coking, and sintering which can result in a dramatic loss in surface area[2]. Sintering, which is a

growth in particle size caused by the minimization in energy, is often seen as the major irreversible cause of catalyst deactivation and is much more rapid at high temperatures and also with the introduction of water vapor. The less stable (prone to sinter) a catalyst is on a support, the more likely it is to sinter, and hence stability and sintering go hand in hand. Maintaining a stable and a well defined particle size is desirable for a reaction to maintain its activity and selectivity, therefore a mechanistic understanding is essential for developing catalysts with longer lifetimes.

Metal particle sintering occurs via particle migration and coalescence or Ostwald Ripening, and earlier studies attempted to determine which mechanistic route determined the sintering process. The attempt of understanding sintering behavior began in the field of solutions rather than in catalytic systems, due to the complications seen in a catalyst environment.

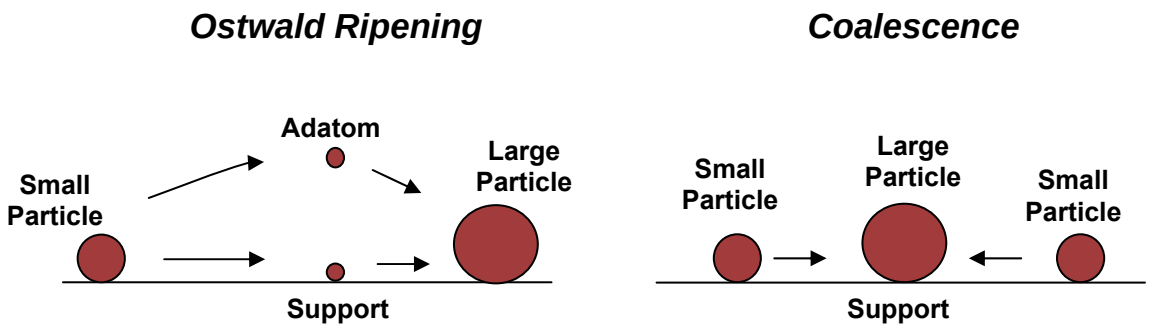

Figure 3 Schematic of particle growth by Ostwald Ripening (left) or by migration and coalescence (right).

Lifshitz and Slyozov[3] were the first to analyze and develop a mathematical mode for grain growth during precipitation from a supersaturated solution. The studies focused on the growth of grains in a solution through diffusion, once the initial solution had

produced nuclei due to super saturation. The mathematical model paved the way for future work relevant catalytic industrial systems.

Gruber[4] developed a mathematical model for the extended the work of migration and coalescence of bubbles due to swelling and gas release in nuclear fuel elements. Gruber's work removed the limitations of characterization of a size distribution through the size of the mean radius and used computer calculated results to determine the bubble size distribution as a function of time. The work included the results of coalescence by random migration and migration in a uniform biased manner. It was determined that the diffusion coefficient for a bubble migrating along the surface (fuel surface) was

$$D_p = 0.301 D_s \left(\frac{a}{R} \right)^4 \tag{1.1}$$

with *Ds* [5] as the surface diffusion coefficient calculated below, *a* as the inter-atomic distance, and *R* as the bubble radius.

$$D_s = D_o \exp\left(\frac{-Q}{RT} \right) \tag{1.2}$$

Q in this case is the activation energy for surface diffusion with Do as a constant. This gave a clear calculation of why particle migration depended so heavily on particle size when support interaction was a small influence. The diffusion coefficient could then be further implemented into a function to determine the overall bubble particle size distribution throughout time. The distribution formula for two bubbles (*i, j*) coalescing would result as

$$\Delta f_{ij} = f_i f_j \left(n_i^{1/2} + n_j^{1/2}\right)\left(n_i^{-2} + n_j^{-2}\right)\Delta\tau \qquad \textbf{(1.3)}$$

where n is in terms of the number of atoms per bubble, f is the force exerted on that atom, and

$$\tau = 91.7 a_o^4 D_s m \left(\frac{\gamma}{kT}\right)^{\frac{3}{2}} t \qquad \textbf{(1.4)}$$

m, defined as the concentration, should not have a large effect on the overall distribution. The surface tension (γ), time (t), and the temperature (T) can vary in experiment, with k being the Boltzmann constant. The results for both methods of migration (biased and un-biased) produced a bubble size distribution of log normal type, where the smaller sized bubbles decreased in number and larger bubbles were seen to increase.

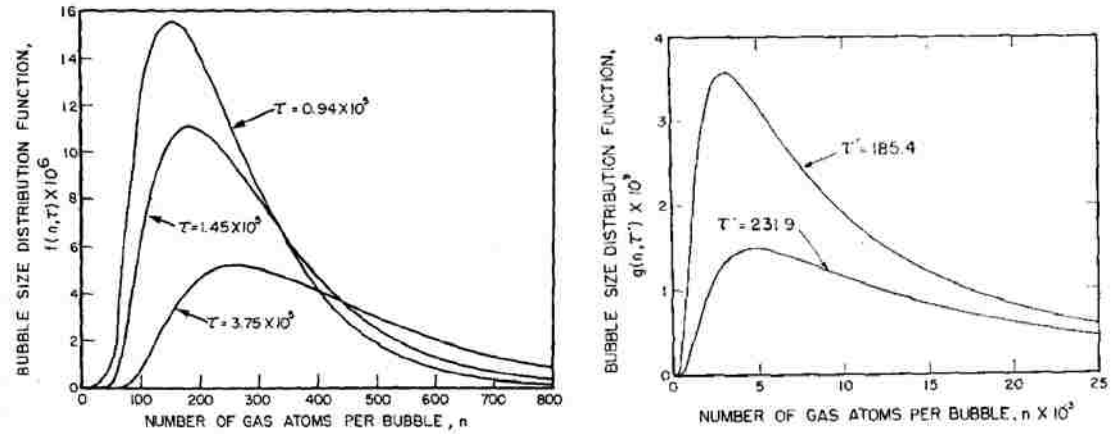

Figure 4 Bubble size distribution for an unbiased migration model (left) and a biased migration model (right). The distributions become broader and develop a longer tail towards the right as time (τ) is increased. Graphs by Gruber[4].

The calculations were shown to exhibit the same behavior as bubble migration (log normal distribution) but were not useful to the material science world as of yet. Stated by Gruber himself, the results had not yet been applied to existing experiments and may not be compared accurately to experiment due to the assumptions made in the calculations.

1.4.1 Solutions to Solids

Chakraverty[6] made the leap from precipitate growth in solutions to thin films and metal particles. The method used two rate limiting steps of growth, assuming growth by atom diffusion and capture by nuclei caused by a decrease in overall chemical potential. The chemical potential (μ) given by the Gibbs-Thompson relation is stated as

$$\mu = \mu_o + \frac{2\gamma_m \Omega}{r} \tag{1.5}$$

with Ω as the atomic volume, γ_m as the metal surface energy, and r as the radius. The particle surface energy is dependent on the support surface energy γ_s, the metal-support interaction energy γ_{ms}, and the contact angle (θ) of the metal as seen in the equation below.

$$\gamma_s = \gamma_{ms} + \gamma_m \cos(\theta) \tag{1.6}$$

The rate limiting step would either occur by atom transfer to the substrate from the nuclei or by atom diffusion along the substrate surface as depicted in the figure below.

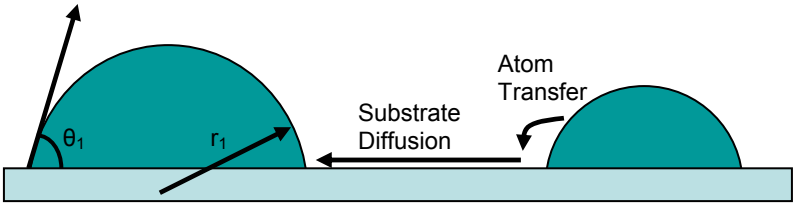

Figure 5 Illustration of the two limiting steps of atom migration and coalescence: atom transfer and atom diffusion along the substrate.

Chakraverty also introduced the concept of a critical radius into his calculations when obtaining the growth behavior of these metal particles. The critical radius, which neither decreases nor increases (mean radius), can be defined as

$$r^* = \frac{2\gamma_m \Omega}{kT \ln(s)} \text{ with } s = \frac{\bar{n}}{n_{eq}} \tag{1.7}$$

The ad-atom concentration defined by the equilibrium vapor pressure (n_{eq}) and the current atom concentration of the atom ($\bar{n}$) determine the total concentration of atoms on the surface (s). The two methods of determining the change in radius over time calculated to be

$$\frac{dr}{dt} = \frac{n_{eq}\gamma_m \Omega^2 D_s}{\log l \alpha_1(\theta) kT r^* r^2}\left[1 - \frac{r^*}{r}\right] \tag{1.8}$$

for surface diffusion rate limited and

$$\frac{dr}{dt} = \frac{2\alpha_2(\theta) n_{eq} \gamma_m \Omega^2 \beta}{\alpha_1(\theta) kTr^*} \left[1 - \frac{r^*}{r} \right] \quad \textbf{(1.9)}$$

for interface transfer rate limited. A function of the contact angle (α), the distance to the average atom concentration on the surface (l), and a probability constant (β) are added into the calculations based on the rate determining step.

The resulting calculations produced grain size distributions with tails towards smaller grains, and a cut-off on the right toward the larger grains. The calculations were compared against experimental values gathered from transmission electron microscopy (TEM, where images of catalysts could be taken) with some agreement at the mean radius value but not over the entire distribution. Experimentally, the data gives a tail toward the larger grains while the calculations have it toward the smaller grains. The theory neglects to include other modes of growth, such as the migration of large nuclei itself and other nuclei-nuclei interactions that may explain the discrepancy when compared to experimental data.

Wynblatt and Gjostein[7] took the work of both Chakraverty and Gruber a step further and removed further restrictions made by the previous authors. They applied the work of Gruber to small particles migrating and coalescing on a surface, in particular Pt/Al_2O_3. In the Pt/Al_2O_3 system particles of a size smaller than 2.5nm had an incredibly large migration distance compared to particles of a larger size. It can be calculated in the equation below how the distance traveled (X_p) decreases with increasing particle size over time (t) when the diffusion parameter D_p is dependent on size.

$$X_p = \left(4D_p t\right)^{\frac{1}{2}} \tag{1.10}$$

If the particle migration distance is equal to or less than the distance to another particle (particle interaction), particle migration and coalescence would dominate as the growth mechanism instead of ripening. It was calculated that if particle migration and coalescence did in fact occur, the migration distance and speed of the particle would determine the rate of growth as the actual coalescence event occurs very rapidly (mere seconds).

$$\tau_{cc} = 0.890 \frac{R_o^4}{B} \tag{1.11}$$

Equation (above) is what was calculated to be the time for an event of complete coalescence (cc) with R_o as the unperturbed particle radius and B defined as

$$B = \frac{D_s N_o \gamma_m \Omega^2}{kT} \tag{1.12}$$

with *No* as the number of sites on the particle. As the particles begin to coalescence and grow in size so does the distance between them and particle-particle interaction via particle migration and coalescence would decrease, leaving only atomic diffusion and capture (Ostwald Ripening) as the method of particle growth. Hence, small particles would be highly mobile on the support and sinter through coalescence while larger particles would grow by ripening, large particles meaning sizes of around 8nm.

The work by Chakraverty[6] for the ripening of particles was extended to include the transport of atomic species through the vapor phase (seen below) and to include the

growth of faceted particles, each with its own contribution of importance and own effect on sintering behavior.

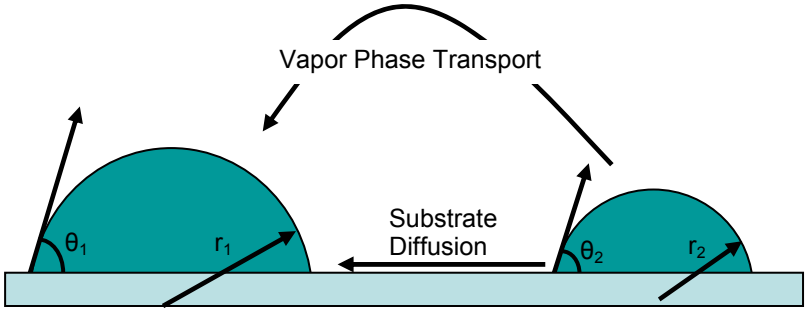

Figure 6 Schematic showing particle ripening by either atom diffusion along the substrate or by diffusion through the vapor phase.

When compared to experiment there was good agreement with the computational Gaussian distributions for initial distributions of the Pt/Al_2O_3 sample[8]. The calculations unfortunately were not in agreement with the Pt sample after it had been annealed, with blame on abnormal growth behavior. This unfortunately left the open question of what sintering mechanism is dominating the sintering process and if vapor phase transport really does contribute to the Ostwald Ripening mechanism.

Granqvist and Buhrman[9] used both controlled experiment and calculation to try and determine the growth of metal particles. Their use of a variety of metals and conditions via inert-gas evaporation gave them the ability to control and measure the rate of metal growth and agglomeration. The experimental results for each metal used in the system produced a particle size distribution (PSD) with log normal type behavior with tails towards the larger particle size. From the obtained data (PSD from TEM) they were able to produce a function with the assumption that coalescence was the only method of

particle growth. The Log Normal Distribution Function (LNDF) with particle size *x* is defined as

$$f_{LN}(x) = \frac{1}{(2\pi)^{1/2}\ln(\sigma)}\exp\left(-\frac{(\ln x - \ln \bar{x})^2}{2\ln^2 \sigma}\right) \quad \textbf{(1.13)}$$

with inclusion of the statistical median ln($\bar{x}$) and the standard deviation ln(σ).

The LNDF corresponded well when compared to the experimental results obtained, leading to the conclusion that only migration and coalescence had occurred in the system. This is the same reasoning that a PSD with a tail towards the smaller particles would give only ripening as the dominant mechanism. This would later be argued by Wanke[10] who calculated that not only can coalescence models fit log normal particle size distributions, but atomic migration models[11, 12] as seen below, can as well (Ostwald Ripening).

$$\frac{dN_i}{dt} = \left(\frac{MD_i}{\sum_{j=1}^{M} D_i} - 1\right) A\exp\left(\frac{-E}{RT}\right) \quad \textbf{(1.14)}$$

The number of atoms in a particle (*Ni*) is changed over time with the parameters *A* and *E* in the equation being adjustable, and with the particle size (*Di)*, total number of particles in the system (*M*), the gas constant (*R*), and the temperature (*T*) all as known. It was later reiterated by Granqvist and Buhrman[13] that their LNDF may have a better fit when

compared to experimental data when comparing both models. In the end both authors agreed that more intensive and conclusive TEM experiments would have to be performed in order for the mechanistic information to be accurately determined, specifically in short term, long term, and *in-situ* studies.

1.5 Modern Studies

New long term studies of a Ni/SiO_2 catalyst by Richardson and Crump[14] provided the statistical data needed of a catalyst exposed to varying thermal treatments and extended sintering time lengths (up to 30hrs). The studies found that no matter the initial PSD, after heat treatment, the PSD would approach a limited value typically in the form of a log normal distribution, with narrower PSD reaching the value faster. It was also believed that at low temperatures (673K) the ripening of particles was favored while at an increased temperature (from 723K-832K) particle migration was favored which was seen experimentally by the broadening of the PSD. Additional evidence from the calculated surface area revealed a dramatic loss in the early stages of sintering (first hour) with a slower rate of loss after longer ageing times. The loss in Ni surface area seen to decrease over 30hrs of ageing for various heated Ni samples was fitted to a power rate law (seen below) with S being the Ni surface area. It was found that n=10 for the various samples given that particle coalescence can have a value varying between n=4 and 8, and the value of n for ripening can vary between <2 and >13. Assuming that the PSD gave conclusive evidence and the power rate law was correct, this provided evidence that

atomic migration (ripening) is responsible for long term growth while particle migration is responsible for early and small particle sintering at higher temperatures (823K).

$$\frac{dS}{dt} = kS^n \tag{1.15}$$

Bartholomew [15] in his studies of Ni/Al_2O_3 and Ni/SiO_2 catalyst commented on how the rate of surface area loss was rapid at first, and slowed down in the later stages of the sintering. A fit to the data suggested that the value of the exponent *n* was decreasing with increased temperature and time, suggesting that early sintering was a result of particle migration with a shift in mechanism to ripening over time.

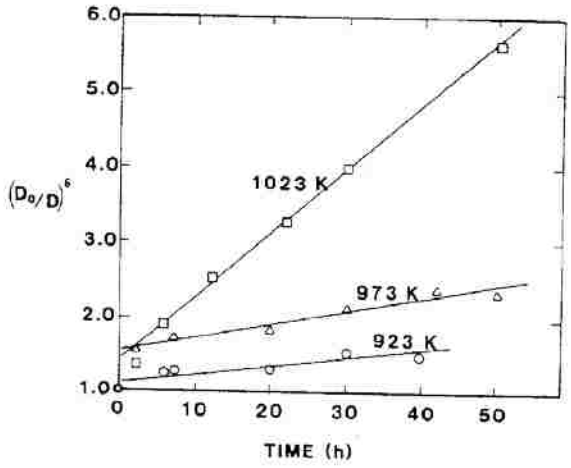

Figure 7 A linear fit to the power rate law (eq. 10) for a 15% Ni/Al_2O_3 with a value of n=7: ○ 923K; □ 973K; Δ 1023K. Provided by Bartholomew [15]

Since the diffusion of small metal particles on oxides would have a strong negative exponent on size (D varies as $size^{-n}$, with n between 4 and 7), implying that the larger particles would be effectively immobile[7]. Hence, if particle migration and coalescence

contribute to catalyst sintering, it must be at the earliest stages of sintering, when the metal particles are small, less than 10 nm. This early stage of migration and later stage of ripening was blamed on the support effects and collapse of the support oxide at those high temperatures.

With advancement in computational power, simulations have provided a faster and more mathematically intense means of predicting and determining sintering behavior of a catalyst. Sehested proposed a deterministic growth model that included only coalescence that corresponded with and accurately predicted sintering behavior of a $Ni/MgAl_2O_4$ catalyst under pre-reforming conditions [16, 17]. Teixeira and Giudici[18, 19] performed their own studies with the inclusion of both ripening and coalescence in their Monte Carlo simulations to predict sintering behavior of a Ni/Al_2O_3 catalyst. This MC simulation would give the option of choosing a coalescence route or ripening route based on the most favorable energy at the exact time step. The Teixeira model was also in excellent agreement with experimental data and had convincing data for predetermining sintering behavior. Both sets of models correctly determined the quick loss of Ni surface area (growth in particle size) at the early stages of reaction and the decrease in rate of loss after hours of ageing. The setback to both studies was the reliance of PSD of catalysts before and after they have gone through reaction (snapshots of the catalyst before and after), just as previous studies before it.

Although, statistically, the recorded experimental data had improved, the concept of determining the dominant sintering mechanism by fitting a distribution or surface area plot was still under question. Lee [20] stated that the fitting of the power rate law could not conclusively determine which sintering mechanism was occurring or dominating.

Datye[21] revealed in experiment that the sintering of supported Pt and Pd catalysts, with either ripening or coalescence as the dominant sintering mechanism, would result in a log normal distribution. The controlled study provided evidence that mechanism could still not be inferred from PSD even with improved statistical data, stressing the need of another method of determining sintering behavior. Only actual recordings and documentation of particle sintering behavior in live time inside a microscope (*in-situ)* would provide conclusive results on sintering mechanisms and behaviors.

1.6 Model Studies of Sintering Catalysts

Typically, industrial catalysts and a three way catalytic converter catalyst undergo a sintering process due to the many different interactions with the support and environment they are put under to make a reaction take place. Due to the many complications of a catalytic system (gas, heat, support, and metal-metal interactions) it becomes difficult to pinpoint which of the contributors is initiating the instability seen in the catalyst, how the sintering process may begin, which accelerates the sintering process, and which mechanism is responsible for the process. Most often used high surface area supports and highly porous powders make catalyst observation and experimental research difficult. Powders may inhibit or contribute to sintering behavior, complicating fundamental sintering studies. It has been seen that one way to analyze industrial catalysts in a simplistic form is to use model supports or flat non porous substrates. Model catalytic systems utilized by groups such as Beke [22], Goeke et al [23], and Herrera-Zaldivar [24] have limited the variables in catalyst sintering processes.

Beke analyzed the sintering (ripening) and evaporation of metals on thin films, and provided theoretical equations corresponding to his findings. His systems involved

copper on molybdenum and palladium on sapphire to name a few. The results of the work revealed particles would become unstable and sinter via ripening which was affected by the support, density of particles on the support, and the length of diffusion of the particles without any environmental interactions. Goeke used model systems consisting of Pt particles on flat oxide substrates to provide a means for improving the visibility of metal particles and to improve counting statistics. The group used a high resolution scanning electron microscopy (HRSEM) to observe the metal particles in the nano-size regime relevant to heterogeneous catalysis. The evidence revealed the importance of the support and how it may have played a role in sintering by utilizing flat models supports of Al_2O_3 and SiO_2. Herrera-Zaldivar looked at palladium coalescence events on carbon and carbon coated silica. The observations documented how the palladium was forming after a larger size was reached and also how the location itself may affect particle formation.

The groups above observed fundamental behavior on flat model systems, blaming either ripening or coalescence as the mechanism responsible for sintering behavior. While the studies provided a means to limit the amount of variables contributing to the loss in surface area, other research groups may still show disagreement to the result as it was difficult to specifically identify the contributors to instability in the system. The influence the support had and particle density seem to affect the sintering rate of the particles, as well as time, equipment used, and temperature the samples were heated to. The limitation of some the instrumentation used, more in depth questions could not be answered (such as: smaller or larger particle size, different support structures, etc.).

1.7 In-Situ Studies

It has been discussed that on industrial catalysts it is difficult to clearly determine how the catalyst becomes unstable and the mechanism at fault for sintering. It has also been discussed that model systems, although they limit the variables in a porous system, still show affects caused by the environment and support used. It is clear that actual recordings of the sintering events taking place on a porous industrial support would greatly aid in determining the mechanisms responsible for nanoparticle agglomeration. *In-Situ* Environmental Transmission Electron Microscopy (ETEM) gives us the ability to observe a catalyst at the nanoscale with the introduction of a gaseous environment and under high temperatures. In this manner, the real time sintering behavior of a catalyst can be captured at different stages of a reaction to determine which mechanism is truly responsible for particle growth.

Early *in-situ* studies performed by Baker[25] of iron particles on graphite in 5 torr of CO confirmed the migration and coalescence of particles on a support surface. Iron particles heated at high temperatures were seen to migrate across the surface randomly as temperature was increased with an increase in movement after the introduction of CO. The particles themselves became more spherical in shape after heating while the displacements of those particles were also seen to increase up to a particular particle size. After that size was reached (~10nm) the displacement distance decreased with increasing particle size as seen in Figure 8.

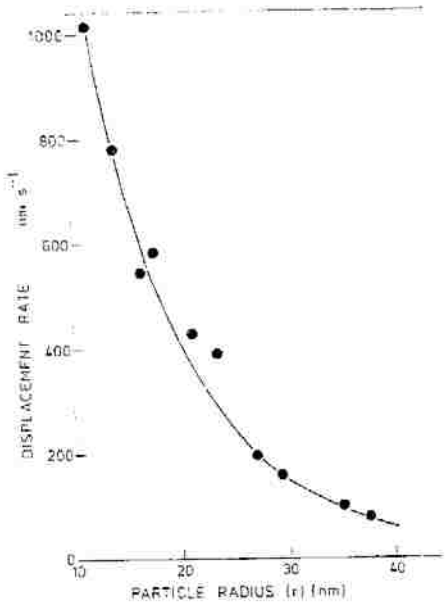

Figure 8 The particle displacement vs. particle radius for Iron particles on graphite at a temperature=740°C. Provided by Baker[25].

In additional experiments performed by Baker[26] of Platinum on Alumina, larger particles were seen not be mobile with temperatures excess of 800°C. The evidence of larger immobile Pt on Al_2O_3 particles led to the belief that smaller particles, below the capable resolution of 2.5nm, were the ones mobile on the support and had sintered in the very early stages of the heating process. Observing the motion in one experiment and not the other stressed how varying metals, supports, and heat treatments can dramatically alter sintering behavior. It also led to the conclusion that small particles (<2.5nm) that could not be resolved by the microscope were extremely mobile and fast on the support, leading to larger sintered particles.

The work provided a route to study and record sintering behavior in real time and under a controlled environment rather than having to transport a sample/catalyst in and out of TEM chamber, exposing the sample to undesirable elements and conditions.

The resolution and time increments provided by Baker would later be improved upon by the work of Bithell[27], utilizing video recordings and analysis of 3 different catalysts: Pt/Al_2O_3, $YBa_2Cu_3O_2/MgO$, and $FeSbO_4$ using *in-situ* microscopy. The *in-situ* video recordings provided a means to break down the obtained data and extract useful information that could shed light on Pt migration and agglomeration, down to times of 5 seconds in real time of particles in the 5nm range. Two key pieces of evidence from the analysis were obtained: the smallest particles on the support were not the most mobile contrary to belief and movement of particles occurred mostly in localized areas. The evidence lead to the conclusions that trap sites and support effects may play a crucial role in sintering behavior. Although the methods of obtaining sintering data had improved, the actual sintering events were often hard to completely capture and resolution was still limited.

With an increase in computing power and constant advancements in microscopy, the limitations seen by Bithell can now be overcome. Faster data collection and increased temperatures due to new holder technology have made it possible to capture sintering events down to the tenths of seconds, at temperatures excess of 600°C, with the capability of resolving particles less than 1nm. *In-Situ* studies by Hansen[28] have shown Ni particles on a $MgAl_2O_4$ support migrating on the surface after heating in hydrogen at high temperature utilizing TEM “movies”. The movies are recordings of a series of images with a high capture rate which can then be converted to a video playing format. The experiments have shown that in-situ TEM can be used to physically captured real time sintering events either it be ripening or particle mobility. His work had focused on longer ageing times, usually over 1 hour in time, still leaving the question

open on what is happening to the smaller particles (<3.5nm) at the early stages of heating and can it be recorded.

1.8 Summary

Important questions still remain and are still in debate over particle stability and dominating sintering mechanisms:

- How does the environment play a role in effecting the stability of the particles, mainly water vapor?
- If Ostwald Ripening is occurring what truly is the rate limiting step?
- How does the porous support structure affect the metal particle stability and sintering behavior?
- What is the actual sintering mechanism responsible for sintering? Can it be visually seen (recorded) and how does the size and stability of the particles affect this behavior?

Here, we will study the sintering behavior and stability of three different systems:

- Palladium on model and powdered Al_2O_3
- Pt-M (M=metals) on carbon supports and,
- Nickel on $MgAl_2O_4$ using ETEM to monitor *in-situ* dynamics of catalytic nanoparticles at high temperatures under a H_2:H_2O environment (seen in pre-reforming conditions).

We will use these systems to give evidence of how support and metal interactions affect the catalyst stability and determine the exact sintering mechanism in the $Ni/MgAl_2O_4$ system.

1.9 Hypothesis

- For our model Pd on Al_2O_3, the rate of emission should be measurable in a vacuum environment, giving us a direct correlation between emission rates and sintering rates that can be modeled.
- In our powder Pd/Al_2O_3 system, a vacuum environment should increase the rate of emission and therefore increase the rate of sintering, as no metal loss should occur.
- For the powder Pd/Al_2O_3 catalyst the introduction of water vapor into the environment should enhance the sintering rate, resulting in larger particles. The water should form hydroxyl groups on the surface making it energetically easier for atoms to detach or transfer from a smaller particle to a larger one. This should be seen no matter the ageing time as the increase in time should correspond linearly with the further decrease in particle surface area as there is nothing structurally preventing agglomeration from occurring.
- For the PtRe/C catalysts the structure of the carbon itself (steps and structure size) is providing edges and steps as adsorption sites for atoms and particles to adhere to, maintaining particle integrity and preventing large particle formation. Also the bimetallic alloy of Pt-Re keeps the particles small and active by maintaining a Re

core and Pt outer shell. This allows the Pt to interact with the reactants and maintain a maximum surface area. The combination of the large amount of adsorption sites and stable core-shell structure allows for higher amounts of Pt sites to interact without agglomerating into large particles

- In the $Ni/MgAl_2O_4$ system sintering observed *in-situ* TEM should reveal the result of larger particles (>5nm) moving along the surface and coalescing with additional particles large or small. Also, the large loss in surface area at the beginning stages of heating are the result of highly mobile small particles agglomerating on the surface, which are a result of the particles not being able to adhere well to the support structure and being unstable.

1.10 Significance

Insight into the atomic scale details and exact dominating mechanism of sintering would aid in understanding the phenomenon and give clues on hows to prevent or control it. The results of the research will also aid in determining which supports structure show more catalyst stability and give a decent pathway to catalyst design. Future catalyst design will use supports with well defined nucleation or adsorption sites for metal deposition which can help control the stability, size, and performance of metal catalysts. Improvements in stability which results in an increase in lifetime of a catalyst will aid in reducing cost of supported catalysts.

Chapter 2

2 Characterization Techniques

2.1 Characterization

The characterization of our catalyst is vital to this work and to catalysis in general. Without characterization, knowledge of the catalyst structure, shape, size, and composition would not be available. In our study the use of many forms of Electron Microscopy, X-Ray Diffraction, and Energy Dispersive X-Ray Spectroscopy to give conclusive results to our catalysts behavior. Electron Microscopy plays a heavy role in our experiments as it gives direct observation of our catalysts before, after, and in some cases during the working state. This chapter will give a brief overview of the characterization methods used and the theory behind them.

2.2 Electron Microscopy

Microscopy is typically known as a familiar area of science, as most people think of microscopy and the use of a microscope as the direct magnification of an object to small to see with the naked eye. The most familiar type of microscope is an optical microscope or light microscope, where light (photons) pass through a series of lenses and produce a enlarged image of the object. Electron Microscopy can be thought of as the same way, but the light source is not light at all, but rather accelerated electrons.

The smallest object that can be resolved using a light microscope can be calculated using the Rayleigh formula below

$$\delta = \frac{.61\lambda}{\mu \sin \beta} \qquad \textbf{(2.1).}$$

The Rayleigh formula contains the refractive index of the medium (μ), the semi-angle of reflection (β), and the wavelength of the source (λ). The wavelength of visible light can vary from 400-700nm, and for a wavelength in the middle of 550nm, the resolution would be calculated to 300nm. This type of resolution would not be sufficient for our studies, as we are studying particles in the 1nm range. If we use electrons as the source instead of light, the wavelength becomes extremely small, much smaller than the wavelength of light. The wavelength for an electron source can be calculated using the de Broglie's equation which determined

$$\lambda \sim \frac{1.22}{E^{1/2}} \qquad \textbf{(2.2)}$$

with E as the energy of the electron. For an electron source of 100keV it was calculated λ would be 4pm, which is extremely small in length[29]. The higher resolution is the main reason why we will use electron microscopy in our study, although the lenses and aberrations seen in a real working electron microscope hinder resolution.

2.2.1 Transmission Electron Microscopy

Transmission Electron Microscopy (TEM) can be compared in a simplified way to an optical microscope where the light source is now an electron source. The electrons

are accelerated through the column and sample to produce a 2-D image of 3-D sample. In our case the high energy electrons are generated with a field emission gun (FEG). The gun itself can be thought of as a cathode with two working anodes: one anode to pull the electrons out of the gun tip and the second anode to accelerate the electrons through the column. The transmitted electrons then pass through a series of lenses in order to produce an image. The condenser lens will turn the transmitted electrons into a parallel beam which can impede on the sample. The objective lens (immersion lens) post-field seen in the figure below focuses the projected image while the intermediate lens magnifies this projected image on a fluorescent screen, known as a Bright Field Image (BF). The image is produced by the differences in the phase of the electrons as a result of passing through the sample, known as phase contrast. This contrast is what gives detailed information about the sample at the atomic level. A CCD camera is typically installed below the screen to collect the variations in the transmitted beam to record the transmitted image. A ray tracer diagram can be seen below showing how the electrons are passing through the TEM column to produce a final image.

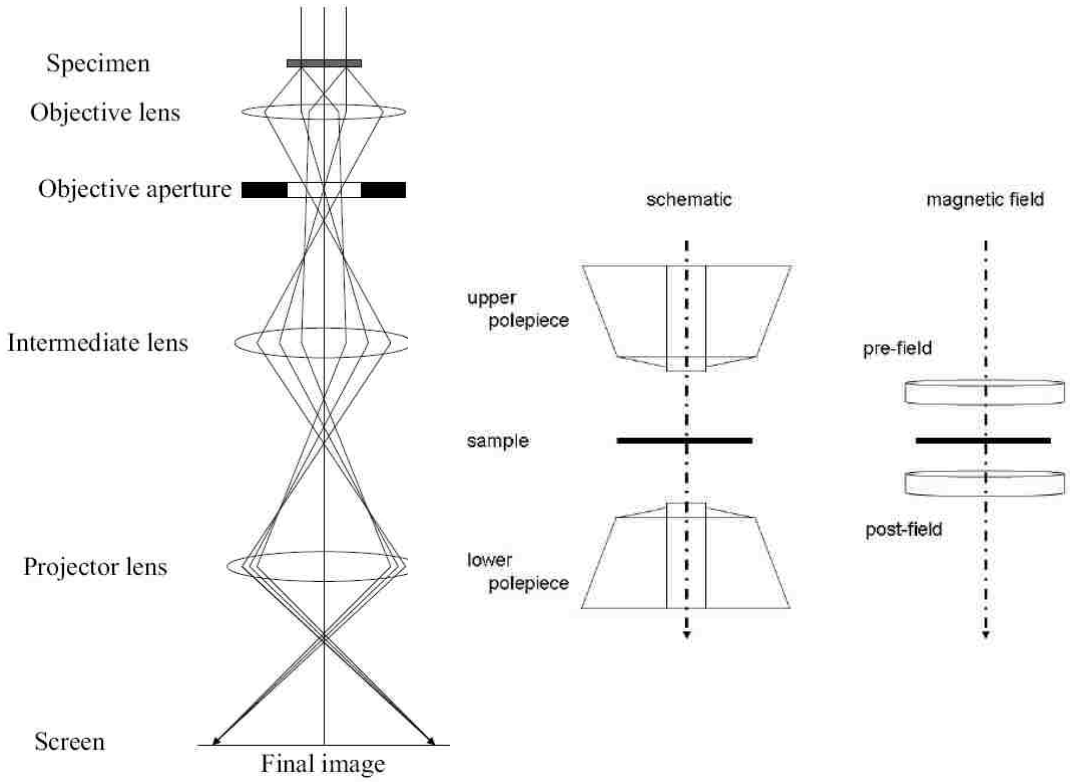

Figure 9 Left: A ray tracer diagram revealing how the electrons are passing trough the microscope column producing a final image of the specimen above. Middle: Schematic of the upper and lower pole pieces around the inserted sample. Right: The Pre and Post-Field of the objective lens. For TEM imaging the post-field is more important while the pre-field is more vital for STEM imaging which uses a scanning probe.

The amount of intensity you get from your sample depends on the sample thickness. As the mass thickness increases the amount of diffracted electrons also increases. As a result the sample area with smaller thickness will show up lighter on the screen while the area with a higher thickness will show up darker in TEM mode.

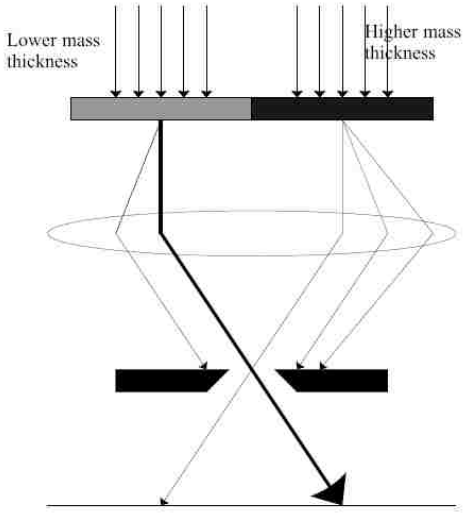

Figure 10 Schematic of how the sample thickness can change the amount of diffracted electrons. Notice more electrons are diffracted for a thicker sample than for a thinner sample, which result in their capture by the aperture. Provided by Wagner[30].

2.2.2 Scanning Transmission Electron Microscopy

Previous imaging was the result of the transmitted electrons passing through the sample with limited high angle diffraction. It is also possible to produce an image using only the highly angled diffracted electrons as well. This type of image is known as a dark field image (DF). It is produced by focusing the emitted electrons into a small probe that scans the sample in a raster like pattern, known as scanning mode. As the sample is scanned with the probe, the electrons pass through either highly diffracted or not and again are collected by a detector. The transmitted electrons that area not highly diffracted are collected by an axial detector, while the diffracted electrons are collected by an annular detector. High Angle Angular Dark Field (HAADF) imaging is the method of collecting the electrons diffracted at high angles as shown in figure 11. The collected

electrons are then put through a photomultiplier tube in order to produce the scanned image.

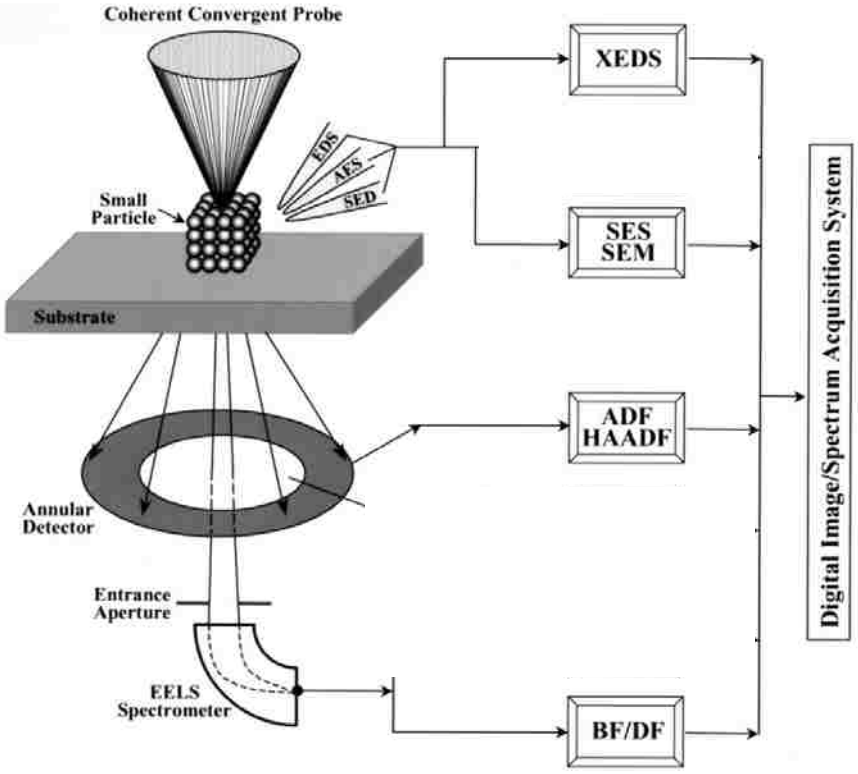

Figure 11 Schematic of the signals produced when using a convergent probe as used in Scanning Transmission Electron Microscopy. Energy Dispersive X-Rays (EDS) and Secondary Electrons (SE) for spectroscopy and microscopy are produced and diffracted off the sample without completely going through, while the High Angle Angular Dark Field (ADF) and Bright/Dark Field (BF or DF) imaging are produced from the transmitted beam. Provided by Liu[31].

When using STEM mode, the probe size determines the resolution of the image which is determined by the spherical aberrations and diffracting aperture. Spherical aberrations can be cut down by using a smaller aperture, but the smaller aperture the more detrimental to the probe size. The minimum probe diameter controlled by diffraction can be calculated using

$$d_D = \frac{1.22\lambda}{\alpha} \quad \textbf{(2.3)}$$

with λ as the wavelength of the electrons and α as the angular diameter of the aperture. The minimum probe diameter controlled by spherical aberrations can be calculated using

$$d_s = C_3 \frac{\alpha^3}{2} \quad \textbf{(2.4)}$$

with C_3 being the third order spherical coefficient. The total probe diameter is determined by a combination of these effects shown as

$$d_{tp} = \left(d_s^2 + d_D^2\right)^{1/2} \quad \textbf{(2.5)}.$$

In this study we have used a series of microscopes to obtain conclusive results on the stability and sintering behavior of heterogeneous catalysts. A JEOL 2010F at the University of New Mexico at the Earth and Planetary Sciences Department was used for imaging of small particles for particle size distributions and for compositional analysis using the EDS system discussed later. The probe size produced by the 2010F is 1nm in size with a beam intensity of 200keV.

Figure 12 Image of the JEOL 2010F Scanning/Transmission Electron Microscope at the University of New Mexico.

2.2.3 Aberration-Corrected Scanning Transmission Electron Microscopy

An improvement in the probe size will give a significant improvement in the resolution of the microscope. By improving upon the aberrations in the microscope (specifically spherical aberrations) the probe size can be focused down to sizes below .1nm, well capable of resolving individual atoms.

With advancements in computer technology, the spherical aberration is now corrected (C_3) upon by improving the focus of all the rays being transmitted; hence the rays focus on a smaller point limiting the spherical aberration[32]. An aberration-corrected microscope was used at the Advanced Microscopy Lab (AML) facility run by the High Temperature Materials Laboratory (HTML) at the Oak Ridge National Labs

(ORNL). The JEOL 2200FS has a CEOS hexapole aberration corrector on the probe-forming side giving a probe size of .08nm, capable of resolving single atoms with the capability of obtaining both BF and HAADF images simultaneously. An EDS detector was also recently installed to give compositional information of the imaged sample.

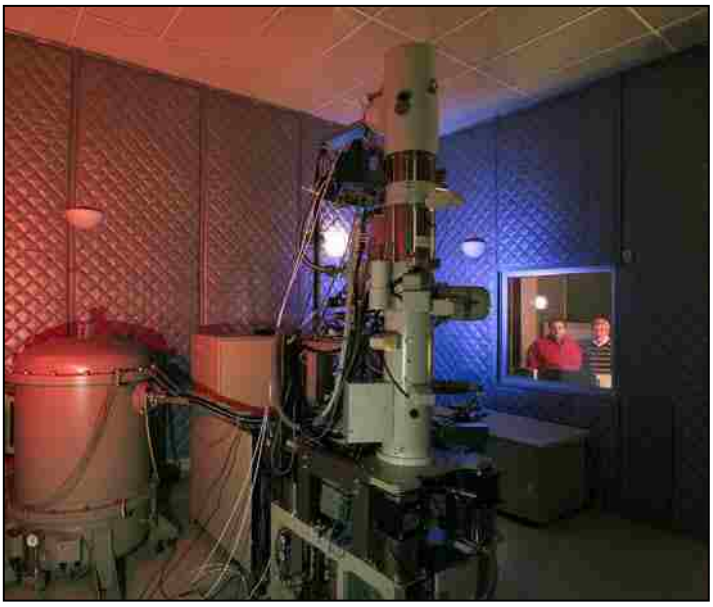

Figure 13 The JEOL 2200FS Aberration-Corrected Microscope at Oak Ridge National Labs. The corrector sits above the sample and adds almost 2 feet in height to a normal TEM. The user controls the microscope in another room (users in back) as to limit any vibrations and interactions with the microscope physically.

With the an aberration-corrected STEM we can analyze the exact sites and areas catalyst particles are occupying and use the ability to over lay the BF images with the DF images to enhance this analysis. The high resolution of the microscope will also give us information at the atomic scale, revealing individual atoms on the catalyst support.

2.2.4 *In-Situ* Transmission Electron Microscopy

In catalysts characterization, it has been observed that different environments may alter the catalyst shape, structure, and size and specific environments may react with the catalyst differently. Researchers will use characterization machinery under environmental conditions or *in-situ* in order to expose their catalyst to a controlled environment without the need for exposure to undesirable conditions[33]. *In-situ* TEM involves the introduction of gases into the TEM sample chamber in order to observe gas-catalyst interactions directly. The amount of gas let into the chamber (up to 20mbar) can be compared to as small when looking at industrial conditions (100bar), due to the fact that transmitted electrons interact with the introduced gas causing a loss in the resolution. It is also dangerous to have a high amount of gas in an operating TEM as the electron source (in our case the FEG) may become contaminated and burn out. Thanks to innovations in pumping design and technology, the gas can be exposed to the sample without damaging the gun. In-situ TEM experiments have been performed before by Baker[25, 26] observing catalyst under a heated gaseous environment and by Boyes[34] which improved Baker's resolution due to design from 2nm to .23nm.

Our *in-situ* measurements were done using a Philips CM300 FEG ETEM working at 300keV. The microscope was fitted with a GIF200 and Tietz F114 camera for both normal imaging and Energy Filtered imaging and for low intensity image collection. It was possible to perform TEM imaging at pressures of up to 5mbar under *in-situ* conditions and temperatures of up to 900°C while obtaining a resolution of .14nm, lower than .23nm. A schematic of the microscope can be seen below in Figure 14, showing

where the additional pumps and piping are placed in order to achieve this type of resolution under these conditions.

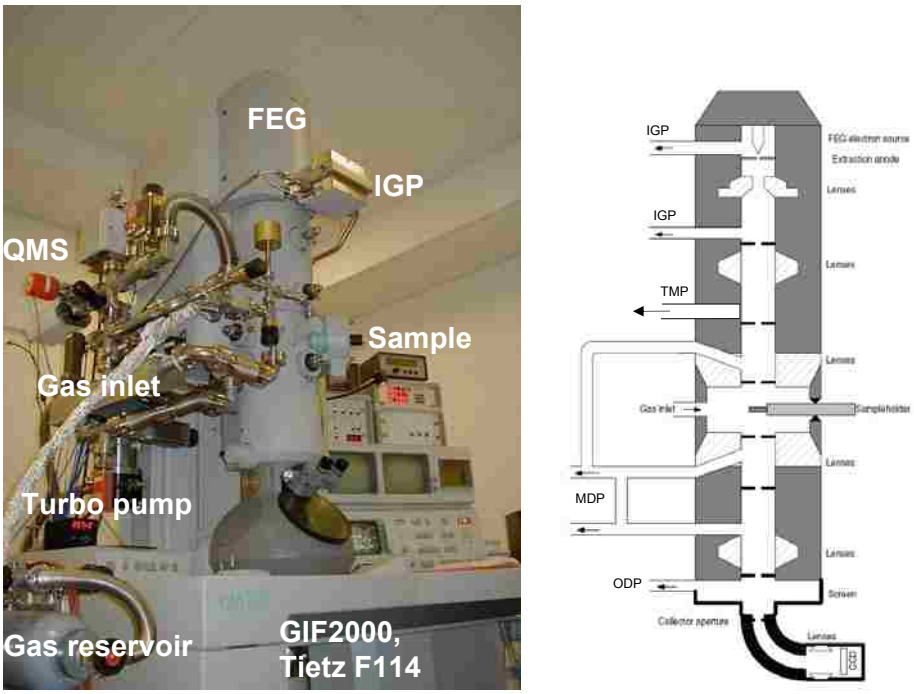

Figure 14 Left: Image of the Philips CM300 FEG ETEM at Haldor Topsøe A/S constructed as a joint project between Haldor Topsøe A/S and Philips. Right: Schematic of the microscope pumping design (cell adopted from Boyes[34]). The top two outlets go to Ion Getter Pumps (IGP), the pump above the C2 aperture is a Turbo Molecular Pump (TMP), the sample chamber is pumped with a Molecular Drag Pump (MDP), and the screen area is pumped by a Oil Diffusion Pump (ODP).

The inlet system for the gases was designed to introduce two gases at one time, with the option of adding water vapor to either or both. For the discussed experiments we only use hydrogen as the introduced gas with all other valves and filters closed off. How the gas was introduced into the cell can be seen in Figure 15. The H_2O holding chamber went through at least 3 repeated freeze thaw cycles before use and being released into the system via a needle valve.

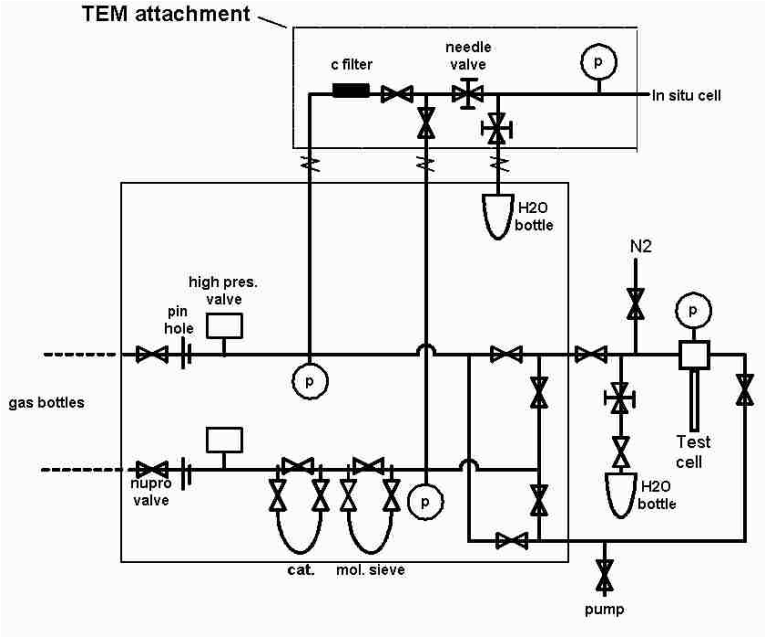

Figure 15 Schematic of the gas inlet system prior to the TEM microscope inlet. The lower inlet without the carbonyl filter was path of primary use.

In addition *in-situ* TEMs have the ability to heat up samples due to specially designed holders capable of reaching temperatures of up to 1000°C. For these experiments heating was controlled with a GATAN heating holder designed for the microscope. The holder heating element was controlled with a controller box, capable of reading out the grid temperature and executing a desired ramp rate. The holder was also equipped with connections to a small water pump for cooling and maintaining a stable temperature. This *in-situ* TEM will provide experiments to observe a catalyst under harsh conditions as in industry, and will give conclusive evidence on what sintering mechanism is dominating during the heating process.

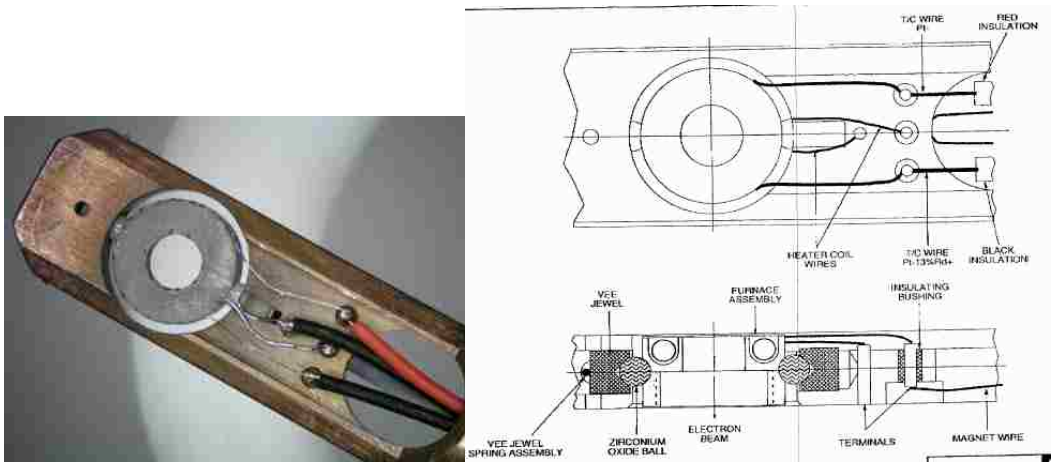

Figure 16 Image and Schematic of the GATAN sample holder used for heating *in-situ* experiments. The sample, which is on a TEM grid, is placed in the cup and secured with a spacer ring.

2.3 Scanning Electron Microscopy

Scanning Electron Microscopy (SEM) is similar to TEM but the characterization technique uses a smaller dosage of electrons (around 2keV) on the sample compared to a TEM (200keV). This lower electron voltage gives a more surface characterization of the sample, which will give the morphology and topographical structure of the support. There are two different methods to use on the SEM, either using Secondary Electrons (SE) or Back Scatter Electrons (BSE). The BSE mode allows the user to see elements of higher atomic number due to the larger scatter of the electrons (larger scatter is due the weight of the atoms).

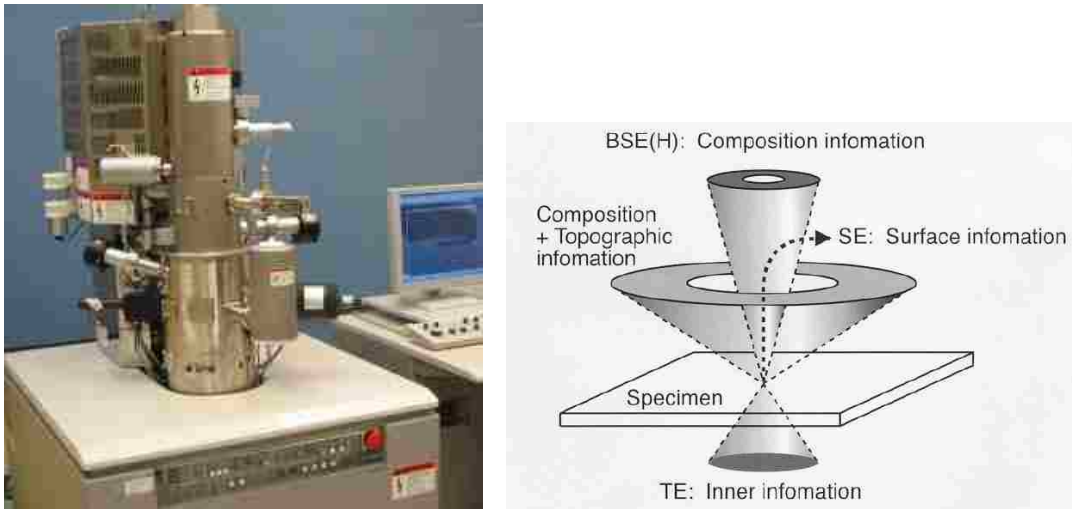

Figure 17 Left is the Hitachi S-5200 Scanning Electron Microscope at the University of New Mexico. Right is a schematic showing the collected Back Scattered Electrons (BSE) and Secondary Electrons (SE) produced by the microscope beam and sample.

2.4 *Energy Dispersive X-Ray Spectroscopy*

Using microscopy to obtain elemental information or analytical microscopy is beneficial as the incident beam emitted can give multiple detectable signals as seen above in Figure 11. Energy Dispersive Spectroscopy (EDS) is one of the most commonly used analytical techniques used with a microscope. As the electron beam bombards the sample ground state electrons get excited and are ejected leaving a "hole" in the atomic shell. An outer shell electron may fill that hole and in doing so releases an amount of energy, which is the difference between the vacant shell and the shell with the contributing electron. The energy released is in the form of X-Rays and are characteristic as the energy levels in elements are element specific.

The STEM JEOL 2010F microscope at UNM is equipped with an EDS detector, capable of detecting a signal in both regular TEM mode and in STEM mode. While in

TEM mode, the detector can be used to collect an overall analysis of particles in the micron range. While in STEM mode the detection can be much more specific. With a focused probe of 1nm, it is possible to get elemental data from small particles as performed previously[35]. This small probe size allowed us to measure the chemical composition of particles on our catalyst in addition to small areas of the support which may or may not be resolved during the imaging process.

2.5 *X-Ray Diffraction*

As discussed above, X-Rays can carry characteristic information about a catalytic sample and is one of the oldest techniques used in catalysis. X-Ray Diffraction (XRD) uses X-Rays to obtain information of the bulk sample by identifying crystalline phases by means of lattice structural parameters. XRD is caused by the elastic scattering of X-Ray photons by atoms in a periodic lattice. The diffracted X-Rays in phase give constructive interference and the lattice spacing can be derived using Bragg's relation[36] below

$$n\lambda = 2d \sin\theta \tag{2.6}$$

where λ is the X-Ray wavelength, d is the distance between the two lattice planes, and θ is the angle between the X-Rays and the normal to the reflecting lattice plane (n = order of reflection =1,2,..). The angle and measured spacing can be seen in the schematic in Figure 18.

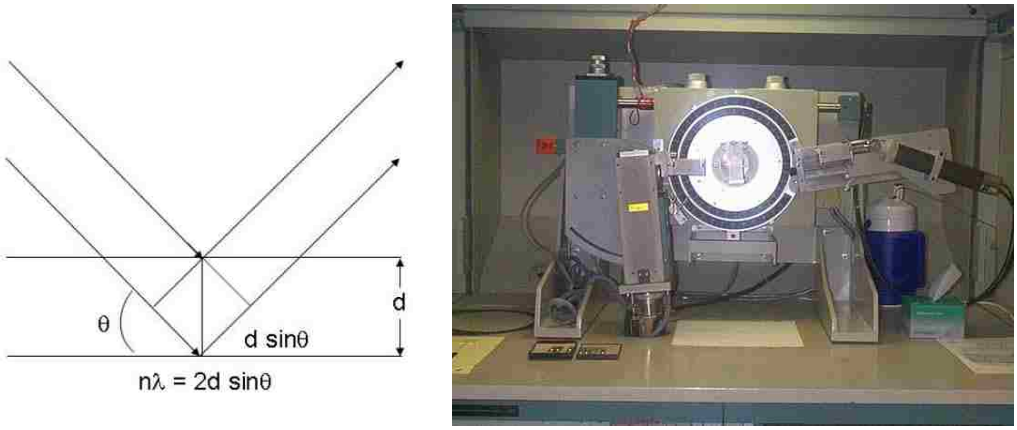

Figure 18 Left: Depiction of the scattered X-Rays giving rise to constructive interference. Right: Image of the XRD machine used at the University of New Mexico.

A diffraction pattern of a supported catalyst is formed only by a small fraction of the particles. The sample then has to be rotated to increase the number of particles that contribute to the XRD measurement. A problem arises though as only sufficient long range order produces clear diffraction peaks and shapes. The peak shapes themselves provide information on the dimension of the planes; however particle sizes below 100nm produce a shape where line broadening may occur due to destructive interference. Peak shape can be related to particle size by using the Scherrer formula below

$$\langle L \rangle = \frac{K\lambda}{\beta \cos\theta} \qquad \textbf{(2.7)}$$

where $<L>$ is the dimension of the particle perpendicular to the reflecting plane, K is a constant (usually =1), λ is the wavelength of the X-Rays, β is the peak width, and θ the Bragg angle. With this technique we can get a bulk analysis of our catalyst sample complimentary to our site specific analysis performed by TEM.

Chapter 3

3 The Stability of Palladium on Al_2O_3

3.1 Introduction

All industrial catalysts, and especially automotive catalytic converter catalysts, suffer from loss of activity after use. While many factors contribute to catalyst deactivation, sintering of the nanoparticles leading to a loss in surface area represents one of the dominant causes. In a working automotive catalyst, there are many components such as various oxide phases that provide redox capabilities making it difficult to characterize catalytically active metallic phase. One approach has been to simplify the study of such catalysts and to use model supports that are composed of non porous flat substrates. Such model catalytic systems utilizing metals seen in automotive catalysts discussed in the previous chapter by Beke1 [22], Goeke [23], and Herrera-Zaldivar [24] limited the variables that contribute to the catalyst sintering processes, but may have not accurately made a comparison to industrial supports or clearly identified the direct route ripening follows: vapor phase transport or diffusion along the support. This study will try to investigate the underlying mechanisms of Ostwald Ripening that determine the rates of metal sintering which should aid in the future development of strategies to prevent sintering using both model and porous supports.

Previous work has showed that the catalyst support will affect sintering rates. Ageing studies performed on model samples of Al_2O_3, ZrO_2, and YSZ revealed a different amount of particle growth after 12 hours of heating at 900°C under a N_2 gas

environment as shown in the table below. Unfortunately the exact route of atom transport can not be clearly identified in a system with a gaseous environment.

Table 2 The size (diameter) of Palladium particles on 3 different flat model supports aged under N_2 at 900°C for 12 hours. It is seen that Al_2O_3 was measured to have the largest increase in particle size with ZrO_2 having the least. The SEM images and PSD can be seen in Appendix A.

Palladium on Model Supports Aged in N_2 for 12 hours		
	Pd Particle Size Before Ageing	**Pd particle Size After Ageing**
Al_2O_3	**11nm**	**69nm**
SiO_2	**11nm**	**49nm**
ZrO_2	**14nm**	**18nm**

Our flat model research will focus on one support, Al_2O_3, and determine the exact contributing factor to particle growth. Once a relating factor determining sintering can be extracted, the supports can then be varied. From additional previous studies we have learned the growth of Pd particles at 900°C follows the characteristics expected from the Ostwald Ripening mechanism. As seen in the figure below, microscopic studies of the same area of the sample show loss of small particles, while the larger ones appear to be immobile. Also, the rate of sintering does not appear to slow down at long times, and instead the catalyst dispersion follows sintering kinetics $D \propto t^{-n}$ where D is dispersion and n is an exponent, close to 2. These results indicate that in these systems at these temperatures only ripening should occur either by vapor phase transport or by atom diffusion along the support.

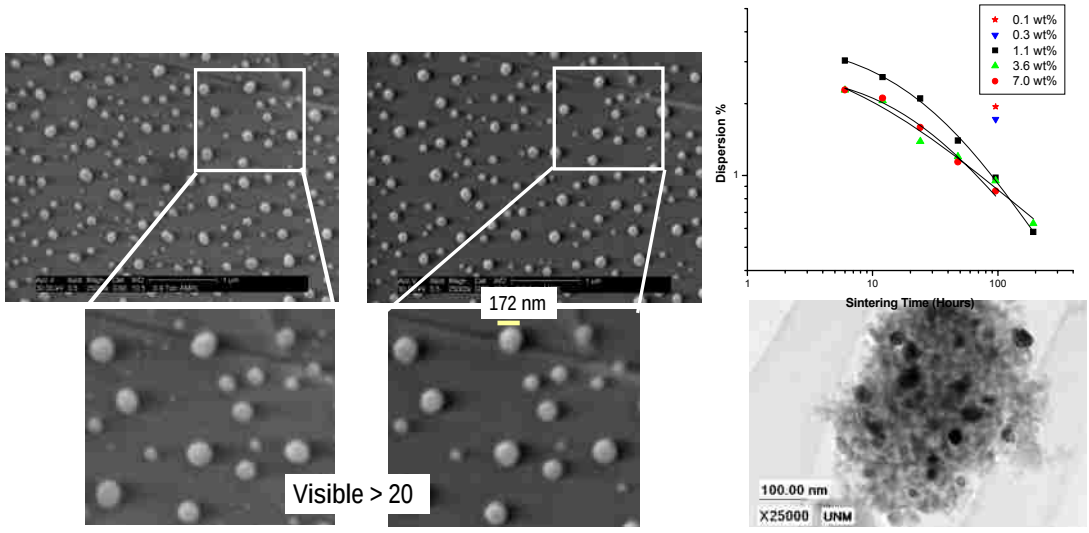

Figure 19 Left: Image of Pd particles after 24hrs of heat treatment at 900°C in a N_2 atmosphere. The magnified images of the specific areas reveal the loss of the smaller particles while the larger particles are stationary[23]. Right: Powder samples of Pd aged in 10%H_2O+N_2 reveal kinetics consistent with Ostwald Ripening provided by Qing Xu.

Parameters that determine the rate of Ostwald Ripening can be

- *Emission* of adatoms (vapor phase) or the
- *Diffusion* of adatoms on the surface as discussed in chapter 1 (transfer or diffusion rate limited).

As a first step, we propose to determine the rates of metal atom emission using the loss of metal from our model catalysts to test our hypothesis that the differences in sintering rates are caused by differences in emission rates (the vapor phase plays a role in ripening). The studies reported here use model catalysts based on flat supports since they allow us to measure the rate of emission of Pd atoms. While porous supports are more realistic, there is little loss of metal since emitted atoms are readily captured by the pore walls due to the high sticking probability of the metal atoms. The high vapor pressure of Pd (~1E-7 Torr) makes it easy to measure the loss of Pd at our ageing temperatures

(900°C) using flat samples. Once we have measured the rates of Pd loss, we can determine how the emission rates correlate to the observed rates of sintering in real (powder) catalyst samples.

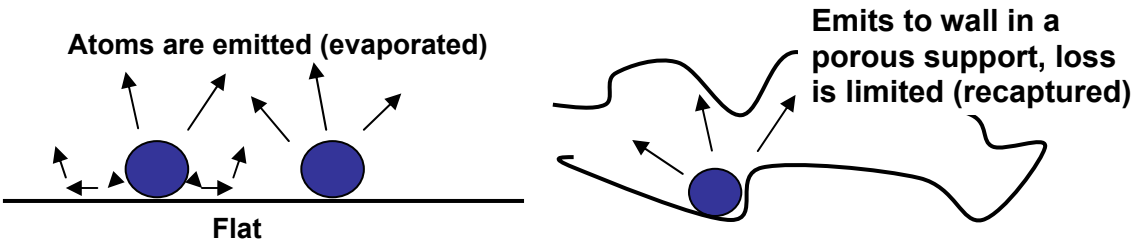

Figure 20 Schematic of how a flat support will allow the emission of atoms into the surrounding environment while a porous powdered support will suppress this action and maintain the metal inside.

3.2 Experimental

3.2.1 Pd/Al_2O_3 Flat Model System

A 1.5nm layer of metal Pd was deposited via evaporation onto a flat sapphire substrate (Al_2O_3 – (0001)) 5x5mm in size with a .5mm depth. Deposition is measured with a quartz crystal monitor and is accurate up to 0.1nm. The Pd layer is oxidized in air at 700°C for 1 hour followed by a reduction in vacuum at 900°C to give a uniform distribution of particles. We can control the density of particles by altering the reduction step as seen in the figure below.

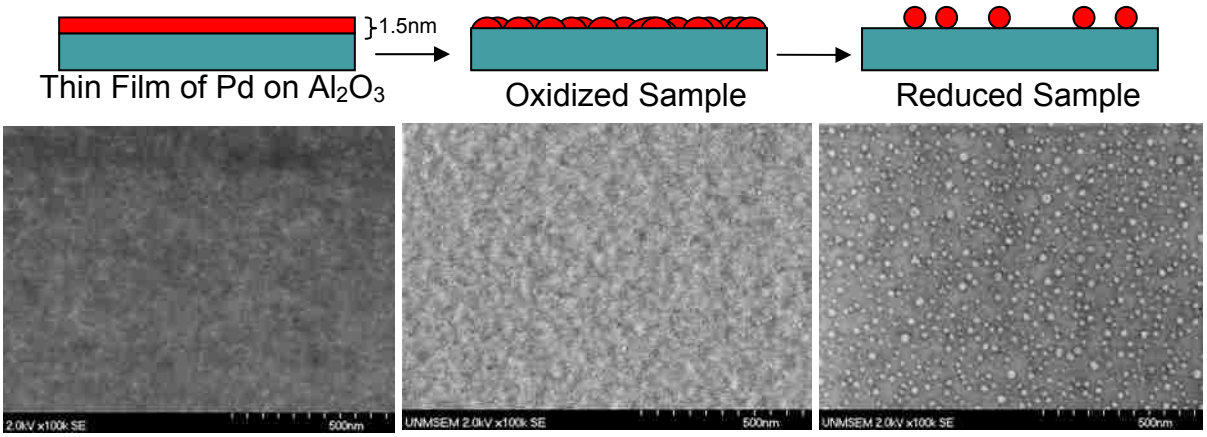

Figure 21 Left: A Scanning Electron Microscope (SEM) image of the Pd/Al_2O_3 model catalyst with thin film only. Middle: The Pd after an oxidation treatment. Right: The reduced sample reveals a distribution of Pd particles. The average particle size was ~13 nm.

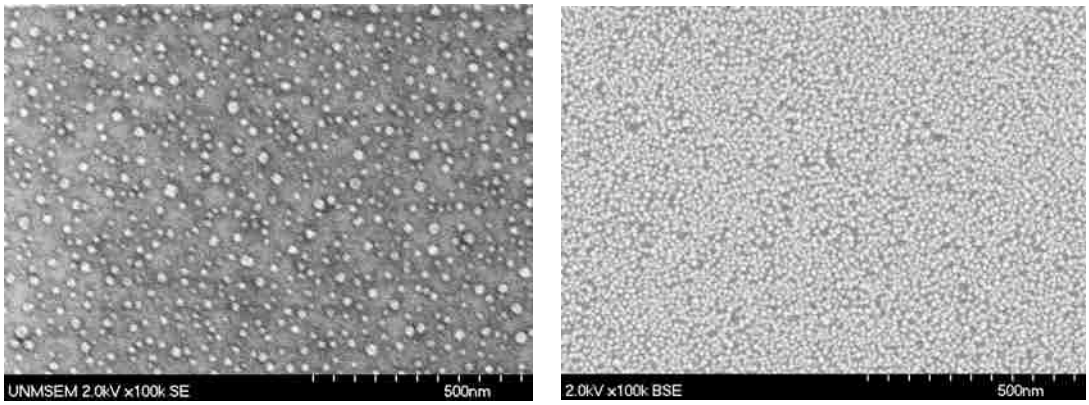

Figure 22 Left: A SEM image of the Pd/Al_2O_3 model catalyst with low particle density (~500 particles per square micron, average diameter 13nm). Right: A SEM image of the Pd/Al_2O_3 model catalyst with high particle density (~3000 particles per square micron, average diameter 9nm).

The Pd samples were put through an ageing process (high temperatures ~ 900°C) in vacuum to determine the evaporation from the amount of metal loss. The ageing studies followed a series of steps; heating to 900°C to form particles, heat treatment at 600°C, and a final heat treatment at 900°C all at a ramp rate of 20°C/min. Cooling of the samples was carried out in vacuum.

The model samples were imaged using a Hitachi S-5200 Scanning Electron Microscope at the University of New Mexico. A sample boat was designed to specifically hold the flat model samples minimizing contact between the boat and the sample. This allowed us to look at the same sample again and again without physically touching the face of the flat sample and also prevented scratching. Imaging of the sample used two modes of collection: Secondary Electron collection and Back Scatter Electrons collection. BSE allowed the counting of the Pd particles in an easier fashion due to the high difference in contrast caused by the difference in the weight of the material. SE allowed us to image the Al_2O_3 support easily and to observe the changes that may have occurred. Particles were counted using the Spirt Software, capable of counting many particles at one time. The images first went through a smoothing process, reducing the noise of the image. The smoothed imaged was then made into a binary image producing an image with a clear distinction between particles and support. The binary image was then analyzed and a particle size distribution (PSD) can then be produced. The plots of the PSD used particle per square micron in order to give an absolute value to our particle counts.

3.2.2 Pd/Al_2O_3 Porous Powder System

The porous 7wt% Pd/Al_2O_3 powder samples were provided by Dr. Karl Kharas at Delphi. Heat treatments in vacuum allowed us to closely match the initial particle size measured on our flat samples (~13nm). The catalyst samples were put through the same

vacuum ageing conditions as the flat samples with additional experiments carried out in N_2 gas with 10% H_2O vapor. After the powder samples were heated in N_2 or N_2 + 10% H_2O for a designated time period they were immediately quenched in liquid nitrogen to prevent any additional ageing. The JEOL 2010F Scanning Transmission Electron Microscope at UNM was used to measure the particle size and produce a PSD. The samples were put in a pestle and mortar with ethanol and a Holey-Carbon Cu TEM grid was dipped into the ethanol solution. X-Ray Diffraction was also performed on the samples to get average particle size for the bulk of the powder sample. It was measured that the XRD and STEM sizes closely matched.

3.3 Results

3.3.1 Pd/Al_2O_3 Flat Supported Model Samples

Initial heat treatments in vacuum used a lower temperature than 900°C due to the unknown amount of Pd that would evaporate off the sample. The sample was heated to 600°C for 30 minutes with only an increase in size seen to change. The sample was then reheated at 900°C for 30 minutes, with a large loss seen in Pd metal and in particle size.

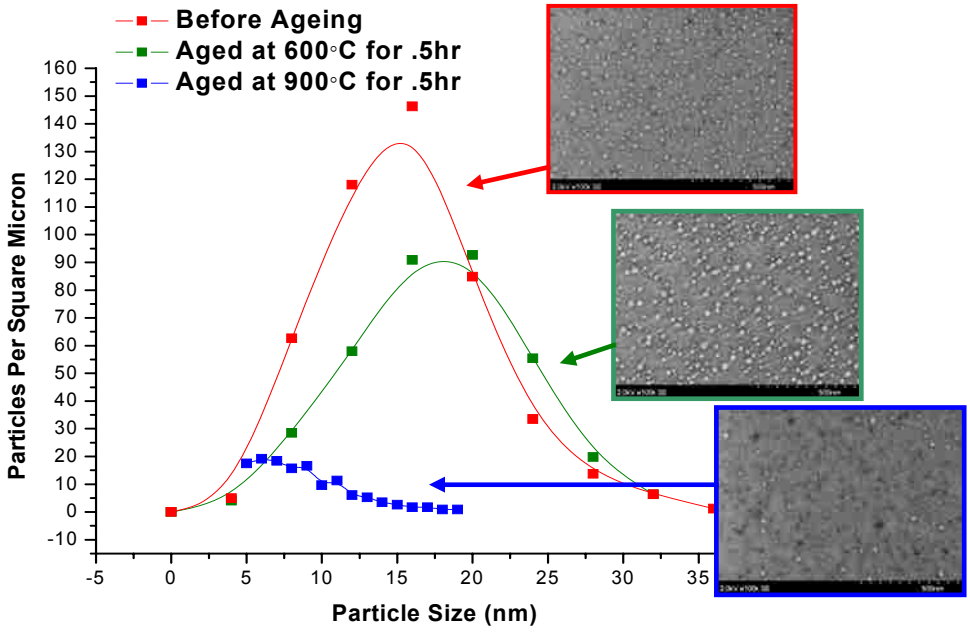

Figure 23 Top: Model Sample showed uniform distribution of particles (average diameter ~ 12.5nm). Middle: After ageing the sample in vacuum for 30 minutes at 600 °C only a slight shift in particle size is observed (average diameter ~ 13nm). Bottom: Ageing for 30 minutes at 900°C in vacuum revealed a dramtic loss in both Pd particle size and amount (average diameter ~ 10nm).

This rate of particle loss has been modeled using Langmuir's[37] equation of evaporation

$$m = \sqrt{\frac{M}{2\pi RT}} \cdot p^* \qquad (3.1)$$

with m being the rate of evaporation (g/m^2-sec), M the molecular weight of Pd, R the gas constant, T equal to temperature in Kelvin, and p^* the vapor pressure of Pd at temperature T. p^* for Pd at 900°C was found to be 8E10^{-6} Pa. Although this evaporation model would work for an unsupported bulk metal, it would not work for Pd nanoparticles

as they have a higher vapor pressure. With this known, an additional term was added to equation 3.1, including the Gibbs-Thompson effect as shown below in equation 3.2

$$m = \sqrt{\frac{M}{2\pi RT}} \cdot p * \cdot e^{\frac{2\gamma\Omega}{rkT}} \tag{3.2}$$

The added term includes the surface energy (γ) and atomic volume (Ω), along with radius of the nanoparticle (r) at the temperature T. Recent work by Campbell[38] has suggested that γ is not constant with radius and can increase with decreasing particle size, but we will ignore this for now. To relate the rate of evaporation of Pd metal to particle size we have used the relation

$$m \cdot SA = \rho \cdot \frac{dV}{dt} \tag{3.3}$$

with SA being the surface area of a sphere, ρ the density of Pd, and dv/dt the change in volume of a particle over time. With a simple substitution we can relate the change in particle radius to the rate of evaporation shown in equation 3.4.

$$\frac{dr}{dt} = \frac{m}{\rho}$$

$$\frac{dr}{dt} = \frac{m}{\rho} = \frac{1.05428 \cdot 10^{-26} \frac{kg}{s \cdot nm^2}}{1.2023 \cdot 10^{-23} \frac{kg}{nm^3}} = .000877 \frac{nm}{s} \cdot e^{\frac{2\gamma\Omega}{rkT}} \quad \textbf{(3.4)}$$

The only variable in the equation would be the particle radius, which could be substituted into the equation. When equation 3.4 was fitted with our gathered data it showed a much lower loss in particle size than the actual event, under predicting the large loss in Pd seen below.

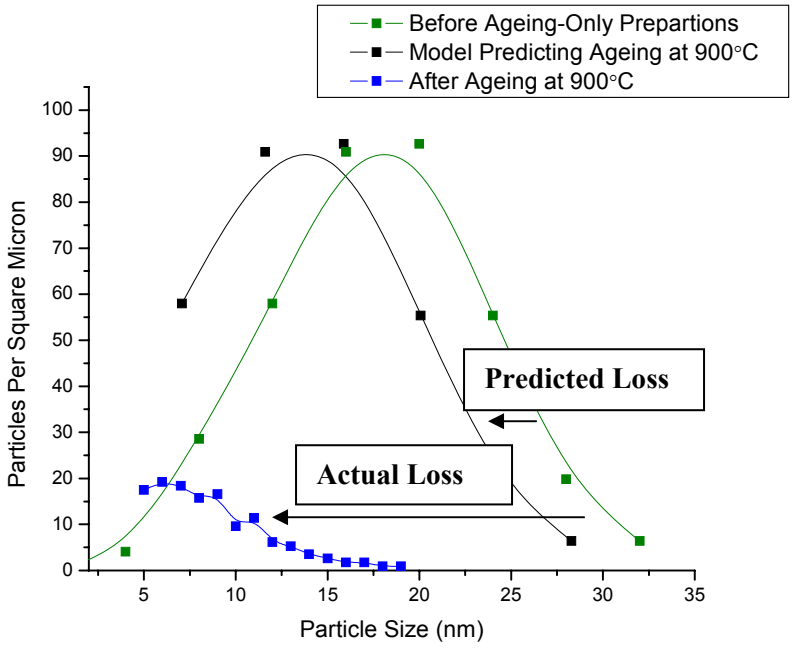

Figure 24 The predicted particle size distribution (equation 3.4) after applying this model to the observed initial particle size distribution. The actual loss is much more severe.

Clearly, direct evaporation from the metal particle into vacuum is not the only pathway for atom emission. We also need to consider the loss of metal via diffusion along the support followed by metal evaporation.

An alternative model for metal loss needs to take into account enhanced emission from the particle due to diffusion along the support. This alternative model provides an additional area around the Pd particle from where atoms can be emitted, as seen in the figure below.

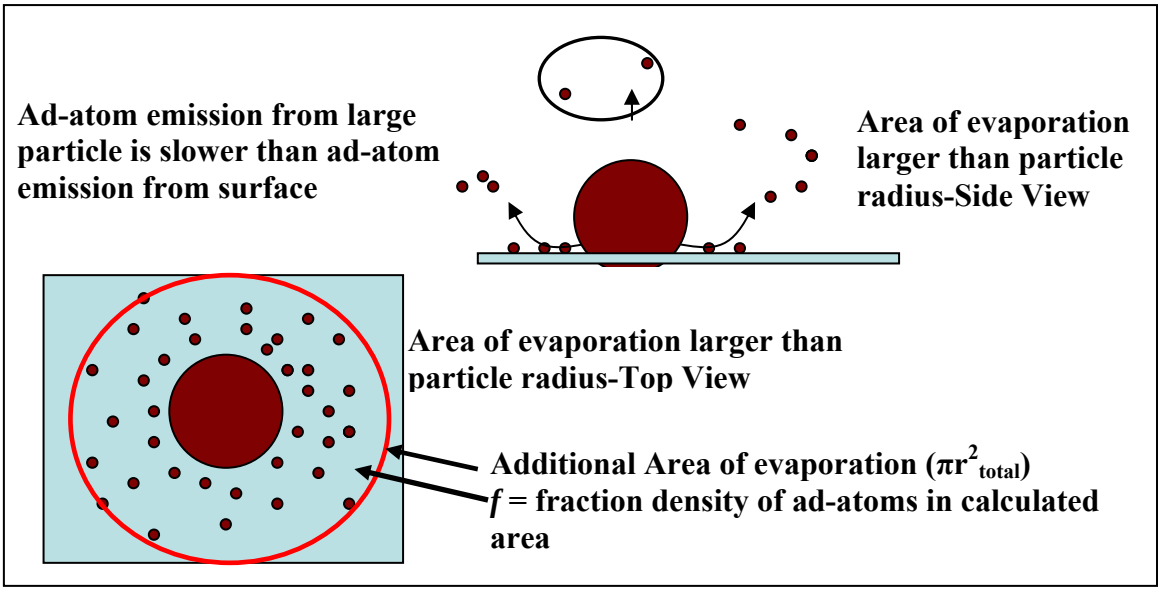

Figure 25 Schematic of a particle and the surrounding area occupied by adatoms on the surface.

There are two additional parameters in this proposed model, both of which are unknown – the distance that the adatoms (πr^2) travel or occupy before they evaporate, and the surface coverage of these adatoms (*f*). We can determine the best combination of these two parameters (calculations in Appendix A) by fitting the model to the experimentally observed metal loss using equation 3.5.

$$m \cdot \left[2\pi r^2 \cdot (\pi r^2{}_{total} - \pi r^2{}_{particle}) \cdot f \right] = \rho \cdot 2\pi r^2 \cdot \frac{dr}{dt} \quad \textbf{(3.5)}$$

The model does show better agreement with our experimental results, showing a much higher loss in particle size compared to the previous direct evaporation model.

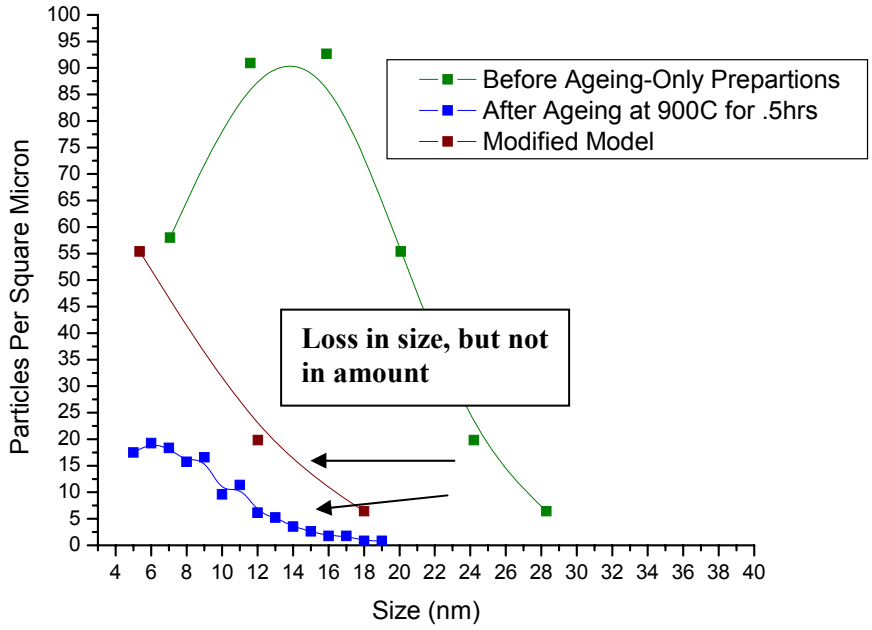

Figure 26 The modified model including additional area around the particle for adatom evaporation. The model shows a much higher loss than compared to the original model. Notice the only change calculated is in size and not in number of particles.

The shift to the left in the model, using a fractional coverage of f=.05, led us to believe that surface diffusion and a highly dense adatom concentration is the dominant contributor for particle loss, as direct evaporation from the particle alone can not account for the metal lost.

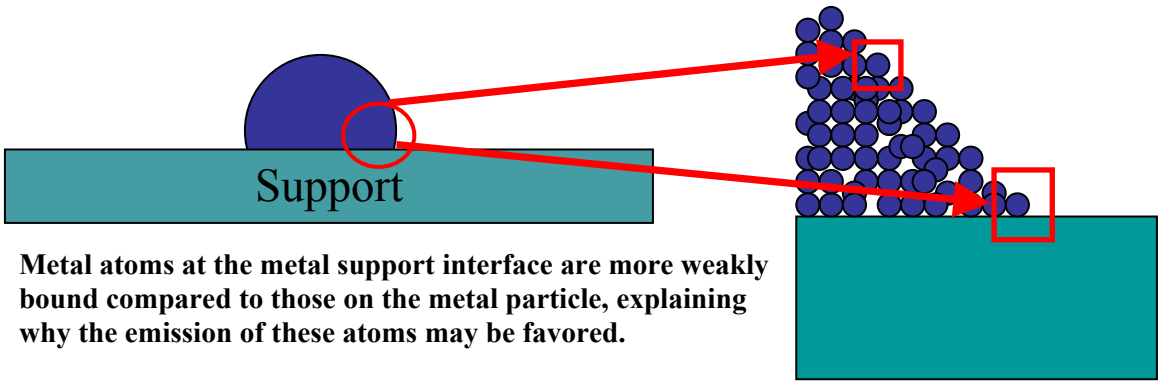

Figure 27 Schematic of a particle on the support describing the location of a more weakly bound atom and a more strongly bound atom. The weakly bound atoms would increase the rate of evaporation of the metal particle.

It must also be noted that defects or impressions were left by once present Pd particles after ageing treatments concluded. This gave even further evidence that the metal support interaction may be highly affecting the sintering behavior, diffusion of adatoms, and the mechanistic route. Additional vacuum studies seen in Appendix A on ZrO_2 revealed a much slower rate of evaporation, with the average particle size maintaining its value. This adds even more evidence on how the particle diffusion lengths and adatom concentrations can be highly dependent on the support which can affect stability and sintering behavior.

3.3.2 Pd/Al_2O_3 Powder Samples

Using transmission electron microscopy we have examined Pd on porous Al_2O_3 powder to provide a comparison with our flat substrates. The samples have followed the same ageing treatments as the flat samples (in vacuum as well as in the presence of flowing gas (N_2 and N_2+10%H_2O) in order to relate the extent of metal volatilization to the rate of sintering. All powder samples initially resulted in an average particle size of

~13nm, the same number average as our model samples. The sample was then split and put through its additional ageing treatment: in vacuum, in 1atm N_2, or 1atm N_2 with 10% H_2O vapor. The results showed an overall increase in particle size for all the samples over time. Below is typically what was seen for our samples, an increase in particle size with a log normal type size distribution.

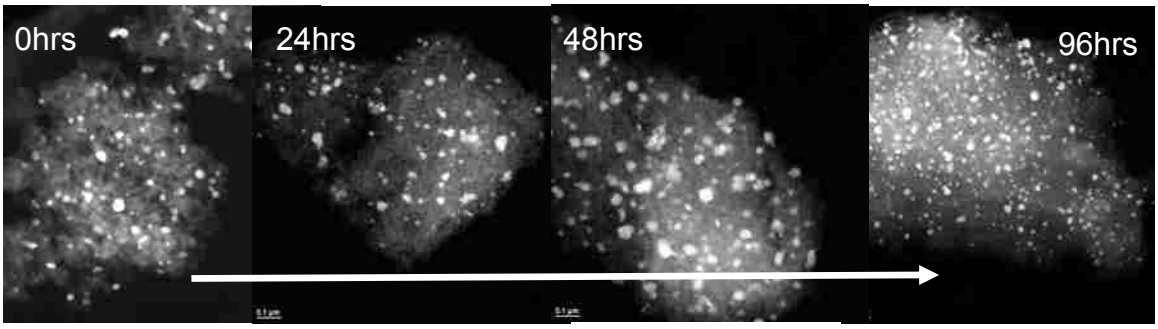

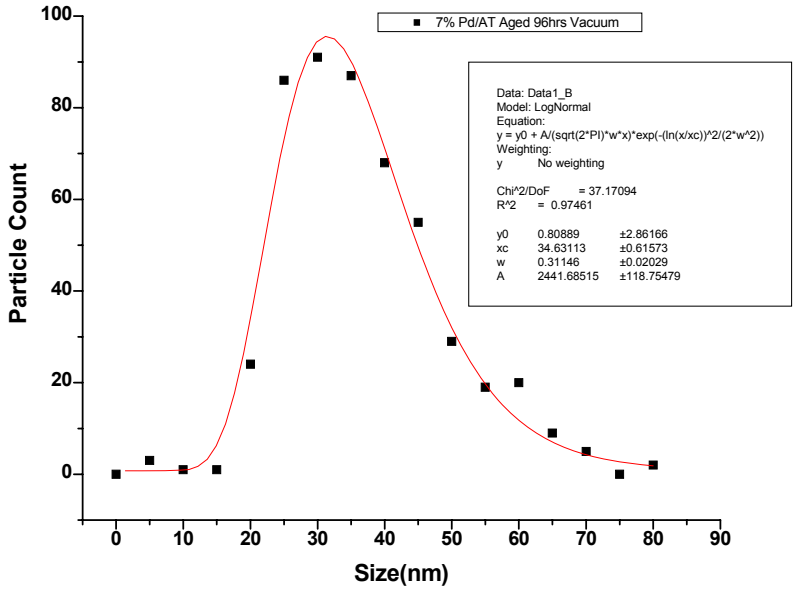

Figure 28 Above is a series of images of our 7wt% Pd/Al_2O_3 aged for varying amounts of time in vacuum. The size was seen to increase and the PSD was seen to agree well with a Log-Normal fitting (below) after heating for 96hrs with no loss measured in Pd metal.

When comparing the particle sizes over time for the three different environments it was observed that the sample aged in vacuum sintered the least while the sample with 10%H_2O in N_2 sintered the most.

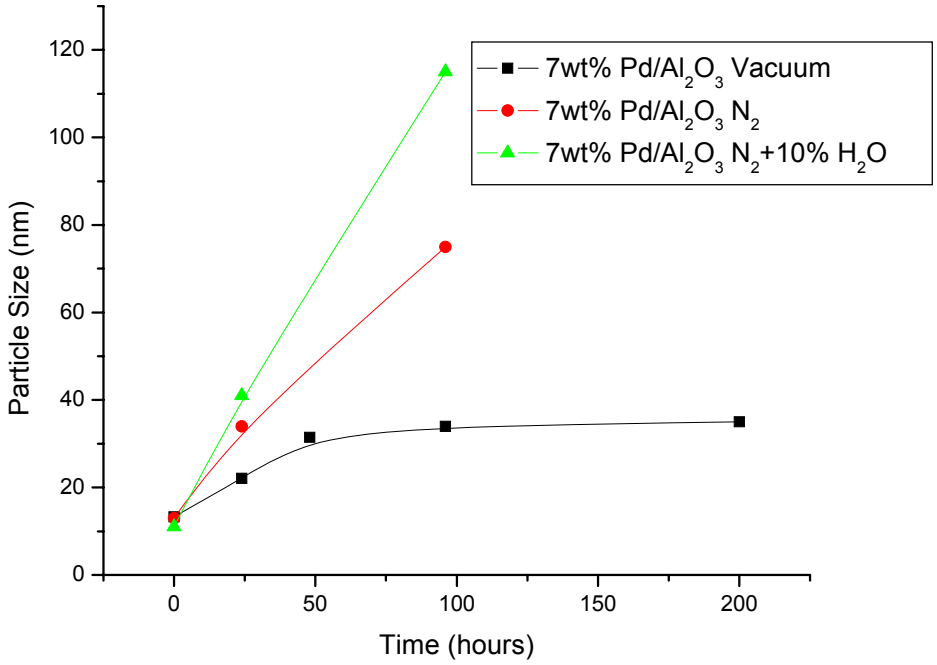

Figure 29 Plot of size vs. time for our 7wt%Pd on Al_2O_3 heated in different environments. The samples heated in N_2 and 10% H_2O were seen to have the largest gain in particle size, while the sample heated in vacuum had the least and had eventually leveled off.

These results contradict our expectation that the rate of metal emission should be enhanced in vacuum and should therefore lead to faster rates of metal particle growth. In a vacuum, the rate of sintering should increase dramatically due to the longer mean free path for metal atoms (mean free path is essentially~∞ in vacuum on a flat material, with the pore walls being the furthest distance in a porous material), while in the presence of a gas, the mean free path is limited. However, a simple calculation of the rates of metal atom emission suggests that all of the Pd atoms should be in the vapor phase over this sintering period. Note most of the Pd is lost from the surface within 2 hours from the

model catalyst. This suggest that the observed particle sizes after vaccuum treatment simply reflect the re-nucleation of metal particles from the vapor during cooling. If the support itself is changing as a function of time, during the heat treatments, it may change the particle nucleation sites and lead to the observed size differences. The leveling out of our distribution curves and eventual stop of Pd particle growth suggests that we are not studying a sintering process when the experiments are performed in vacuum on our powder supports but rather observing changes in the number of support sites for particle nucleation.

When comparing the results between the sample heated in Nitrogen gas and the sample with Nitrogen gas and water, it is evident that water vapor is increasing the sintering rate. This could be the result of either of two interactions: Pd particles making a Pd-OH species capable of being highly mobile or changes in phase to the Al_2O_3 support caused by the H_2O vapor[39, 40]. A sample heated in N_2+H_2O for 96hrs at 900°C then reheated in vacuum for 48hrs a 900°C showed no decrease in particle size. This gave further evidence that a change in support may have occurred (loss in sites), as heating in vacuum would have redistributed the Pd on the nucleation sites as all the Pd would have been in the vapor phase during the vacuum heating. The equipment and experiments performed cannot distinctly isolate the two (change in support or surface Pd species), making it difficult to determine the exact cause for the increase seen in sintering rate.

3.4 Discussion.

The studies themselves focused on the importance of atom emission which could then help determine the rate limiting step in Ostwald Ripening. Measurement of vapor phase atoms is extremely difficult, and hence evaporation studies were used instead to

measure metal lost by vapor phase transport. Initial studies of the flat model samples revealed palladium evaporation is dependent on adatom diffusion, and hence support dependent. A predictive model using the approach outlined by Langmiur for direct evaporation did not accurately predict (under predicted) the experimental evaporation study of palladium for the support. This gave the indication that in addition to direct evaporation, surface diffusion, a large density of adatoms on the surface, or even atom capture by present particles could be occurring on the surface simultaneously. The role of surface diffusion provides clues to the role of the support and its effects on noble metal particles. Further analysis of the samples revealed support defects caused by the palladium-support interaction after reaching 900°C in vacuum, stressing how the particles themselves can affect the support . In the image below it can be seen how the once uniform support now has bumps or cavities caused by the particles adhering to the support, giving a change in image contrast.

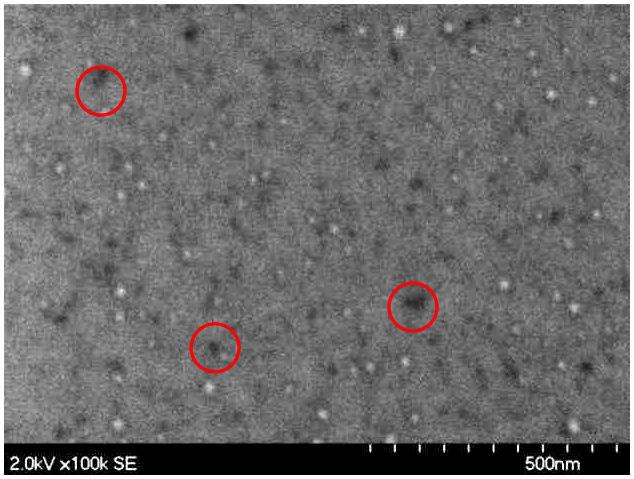

Figure 30 SEM image of flat wafer with Pd after it has gone through 30 minutes of ageing in vacuum at 900C. Notice the darker regions (a few circled) are areas where particles were once present but have been since evaporated.

Studies of powder catalysts were performed to confirm the relation between sintering and support compared to the flat model systems. These powders were put through the same type of ageing and sintering conditions as the model systems. The experiments on powder catalyst supports show that the rate of particle growth slows down in vacuum, suggesting that we are in fact not studying metal sintering, but support changes. This adds restrictions to what can be said about comparing model samples and powder samples, and has limited our study.

Ageing in the presence of water vapor produced larger particle sizes at a faster rate, indicating a role of hydroxyls on the particle surface or changes to the support that may be enhancing sintering behavior. The relation between both the model samples and powder supports is currently under question.

Further studies can reaffirm the results with repeated experiments and modifications can be made to the predictive loss model for better agreement with experimental outcomes. Variations in particle density and support still have to be made in order to determine each of its own affect on sintering rates. Attempts to model or simulate the Pd atom binding at the metal-support interface can provide direct insight into the role of metal-support interactions. Additional studies can vary the support and determine the effects on the sintering process along with DFT modeling to determine the most stable species.

Chapter 4

4 The Stability of PtRe on Carbon Supports

4.1 Introduction

Carbon supported platinum catalysts are used for a variety of reactions, most notably in Proton Exchange Membrane (PEM) fuel cells, but also in hydrogen transfer as well as decarbonylation reactions. A carbon support is necessary for reactions carried out in corrosive environments, where oxide supports would be unsuitable. Unlike oxides which have complex surface chemistry and are populated with hydroxyl groups, carbon supports, particularly pristine graphite, lack surface features that can anchor and support metal particles. Hence, carbon supports often have to be functionalized to create sites for adsorption of metal species. The structure of the carbon support and the functional groups determine the activity, selectivity, and overall stability of the noble metal particles in each type of desired reaction [41-44].

The goal of these experiments is to understand the nature of the surface structure responsible for the dispersion of the noble metals and for helping maintain their stability in reaction environments at the atomic scale in order to investigate the hypothesis proposed in chapter 1. Previous work, via EXAFS, has provided an overall average view of metal-carbon binding[45]. TEM has also been performed to determine how stable platinum particles are on a carbon support after heating[46] but understanding the atomic scale details of metal-carbon interactions is vital to achieve improvements in our ability to develop novel carbon based catalysts. Understanding of the fundamentals of metal

nucleation and growth on carbon can help in design of catalysts with lower metal levels. In this work, we will use a newly available characterization technique known as Aberration-Corrected Transmission Electron Microscopy (ACEM) along with regularly used TEM and EDS to study Pt-Re carbon supported catalyst that have been proven useful for low temperature processes[47-49]. ACEM will be able to determine where the Pt and Re atoms are located on the support and in the particle structure and the nature of the carbon surface structures which are responsible for providing enhanced stability and improved performance. This information will make it possible to understand how we should manipulate, manufacture, and produce carbon supports for specific applications and to optimize reactivity of the catalyst.

4.2 Experimental

4.2.1 Catalyst Preparation

The 10wt% (1:1) PtRe catalyst we use was prepared by incipient wetness impregnation of activated carbon with relatively concentrated solutions of Perrhenic Acid ($HReO_4$) and Chloroplatinic Acid (H_2PtCl_6). The activated carbon used was Norit SX1G- purchased directly from NORIT corp. This carbon has an incipient wetness factor of 1.0g/g (1 g of impregnating solution is required per gram of carbon support to reach incipient wetness). The Pt and Re salt solutions are mixed with water to produce the impregnation solution. The impregnation solution is added to the support drop wise over a period of ~30 min. During this period, the support is stirred and crushed vigorously with a spatula in a ceramic dish. All visible "clumps" were crushed very thoroughly. Subsequently, the catalyst is dried overnight at 120-130°C. Prior to any reaction

experiments or any imaging the catalyst was reduced in-situ at 450°C in flowing hydrogen with a 14 hour ramp to 450°C with a 3 hour hold.

Samples could also be put through a Sorbitol reaction consisting of a 60wt % Sorbitol solution flowed at 0.04 cc/min at 230°C under 250 PSIG for 3-5 days, and in some cases longer. The PtRe Vulcan carbon catalyst was made in the same way and put through the same reaction conditions, but the ratio of impregnation solution to carbon was 1.7 to 1. The BET surface area gathered for Norit was calculated to be 1000m^2/g and 230m^2/g for the Vulcan carbon. This catalyst preparation was used to limit the amount of additional reactive species the carbons may have, such as an -OH group on the surface, in order for the study of the carbon structure to be more comparable.

4.2.2 TEM and EDS Experiments

In order to determine the composition of the particles and answer the question if the Pt or Re species were dispersed on the support and how the metals were alloyed in the bulk of the particles, UNM's JEOL 2010F was used with its EDAX (energy dispersive x-ray spectroscopy) system. The microscope was used in both TEM and STEM modes running at 200keV. Both modes were used in order to get a bulk chemical composition of the large carbon agglomerates containing the PtRe particles and also of individual PtRe particles along with small areas of carbon support alone with no resolved particle species. At low magnification, in TEM mode, we get large count rates and can quantify the overall composition of the sample.

Using a nominal 1 nm analytical probe we analyzed individual particles with some loss in image clarity. The beam was rastered in a box centered on the particles with a dwell time was 10 ms per pixel. Using the same 1 nm analytical probe, we performed analyses of regions that were devoid of metallic particles, once again by scanning the beam in a box that defined the area to be analyzed. In some cases, the analysis was repeated over multiple time intervals to see if the composition changed with time, which would provide evidence that the beam was causing sputtering or preferential loss of individual metal components. The compositional analysis was performed using the Microanalysis Suite from Oxford Instruments. Both the M and L characteristic X-Ray emissions energies were analyzed for the samples, with the L emissions shown in this chapter.

Each PtRe/C powder sample was crushed in a pestle and mortar with 100% ethanol as the solution. A drop of the sample was then placed on a Copper Carbon Coated Holey Grid, which was place and secured in place in a standard TEM holder. A new grid was used for each new sample and this TEM grid could be reused or reproduced for additional imaging.

4.2.3 Aberration-Corrected STEM Experiments

The Aberration-Corrected STEM measurements were performed utilizing the JEOL 2200FS working at 200keV located at the Advanced Microscopy Lab (AML) at ORNL. The camera equipped on the microscope had the capability of obtaining both

Dark Field and Bright Field images simultaneously at a resolution of .08nm. The sample prep was performed the same way as for the 2010F microscope.

Before imaging optimum imaging could be performed on a sample a known correction sample, Au particles on carbon, was imaged in the microscope and an aberration correction was performed. The performed correction alignments were saved and the correction sample was taken out. The inserted sample was beam showered for at least 15 minutes to reduce the possibility of contamination. All images were obtained using Digital Micrograph for both microscopes with size distributions of particles counted by hand.

4.2.4 Labeling and Naming of PtRe Species

It has been highly debated on how to label and name powders and species in the field of nano-characterization [50]. The terms aggregate and agglomerate could have different meanings from field to field, with up to 7 different definitions seen in previous literature [50]. The naming of carbon species themselves has also been defined by individual companies, such as the Cabot Corporation with its definitions below [51].

Agglomerates-Collections of carbon black aggregates; range in size from 100-1000 nm.

Aggregates-Fused primary particles of carbon black; aggregates range in size from 50-400 nm.

Primary Aggregates-The smallest dispersible unit (or working unit) of carbon black.

Primary Particle-Principal unit, or building block, of carbon black; carbon black

primary particles are near spherical particles with diameters in the size range of 10 to 75 nanometers.

In this experimental case, the terms above will be used to describe the carbon species that are found. For the deposited dispersed metal species, the terms atoms and particles will be used, with the term particle describing any Pt, Re, or PtRe species found larger than an atom in size that were imaged to be stable.

4.3 Results

4.3.1 Aberration-Corrected STEM-10wt% PtRe on Norit and Vulcan Carbons

The carbon supported PtRe catalysts were initially imaged before going under reaction conditions but after going through a reduction cycle in Hydrogen at 450°C. Images taken in STEM mode on the JEOL 2200FS at ORNL revealed a fairly different particle dispersion and structure for the two different carbons. It was proven to be too difficult to produce a Particle Size Distribution (PSD) of the PtRe particles on the un-reacted samples of both the Vulcan and Norit Carbon as the average size was below 1nm, and no distinct spherical shape of the PtRe particles could be measured. It must also be noted that the image contrast could not give clear evidence of whether the atoms or particles were Pt or Re, as the captured contrast is extremely similar.

4.3.1.1 PtRe on Vulcan Carbon

The Vulcan Carbon contained a more heterogeneous distribution of Pt and Re particles compared to the Norit Carbon as shown below.

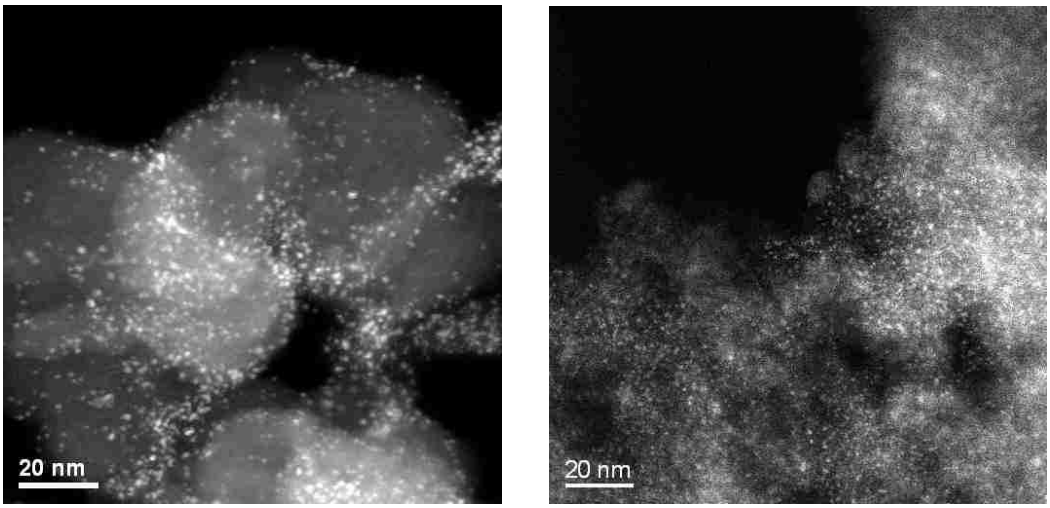

Figure 31 STEM image of 10wt%PtRe on Vulcan Carbon (left) and Norit Carbon (right). The particles are more highly dispersed on the Norit Carbon while the Vulcan Carbon is less homogenous.

The Vulcan Carbon consisted mainly of two different structures: spherical stacked particles on the size of ~60nm (primary particles) and the other with a lower degree of stacking with a higher distribution of edge sites. The primary particles supported very few particles of PtRe on the surface. The few particles imaged on the primary particles were seen at the edges of the large spheres as shown in the figure below. The areas of Vulcan Carbon support containing a rougher and less stacked structure were imaged to have a majority of the PtRe particles deposited.

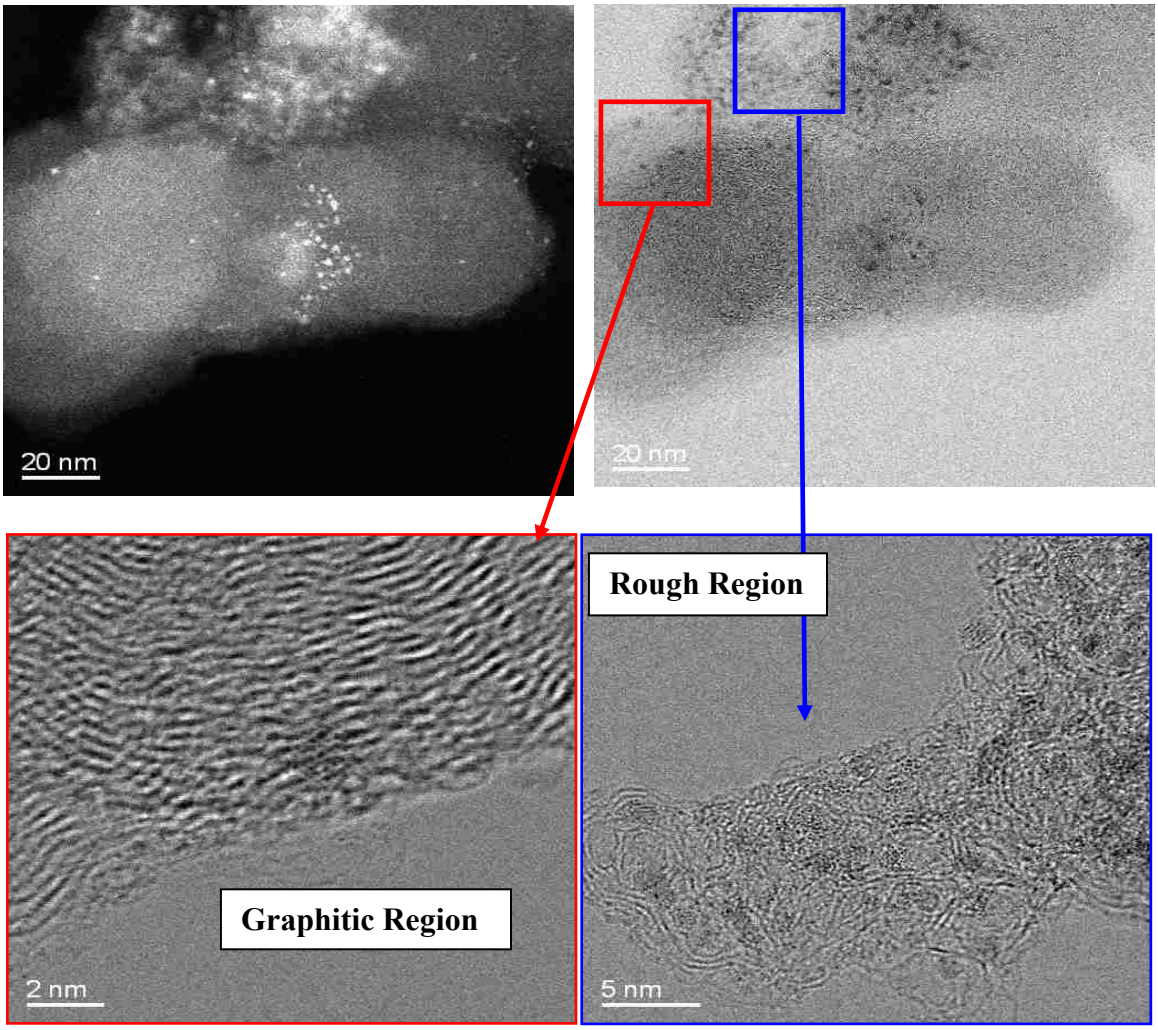

Figure 32 10wt%PtRe on Vulcan Carbon sample: The Dark Field Image (Top left) reveals the PtRe particles more clearly and the Bright Field Image (Top Right) enhances the resolution of the carbon structure. The highly stacked region of the carbon has fewer particles of PtRe than the less stacked region of carbon.

4.3.1.2 PtRe on Norit Carbon

The Norit Carbon consisted of a broken up structure similar to that of a finely chopped onion (many edge sites) with PtRe particles and atoms homogeneously distributed. The small structures could vary in length from .4nm up to 2nm with spacing

between them as small as .25nm. These regions of Norit Carbon were heavily disordered with no particular direction or preferred alignment.

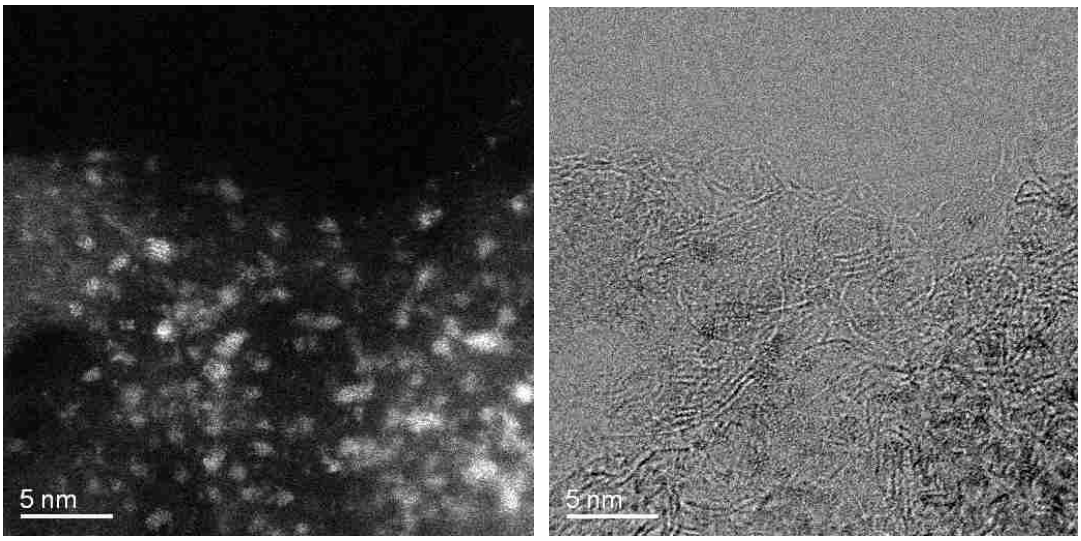

Figure 33 10wt% PtRe on Norit Carbon: The Dark Field Image (left) and Bright Field Image (right) reveal the homogenously dispersed PtRe particles as well as the carbon structure.

Due to the microscopes ability to capture both BF and DF images simultaneously, it was possible to overlay the images and determine the location of the PtRe particles and atoms on the carbon structure. This type of analysis was only performed on the Norit Carbon sample as the Vulcan Carbon sample had limited or no single atomic species on the surface making it easier to determine where the PtRe particles were sitting on the surface. In the figures below it is possible to see that the atomic species and particle species of PtRe are forming at the ends of the short carbon structures (edge site). The particles appear to form in areas where a multiple amount of these carbon edges are meeting, producing an area where nucleation can start due to the large amount of adsorption sites in one area. As the Vulcan Carbon does not contain the same type of structure, those

adsorption sites are not available, making it easier for the particles to sinter and grow together, as more sites should lead to a more highly dispersed metal on the carbon support.

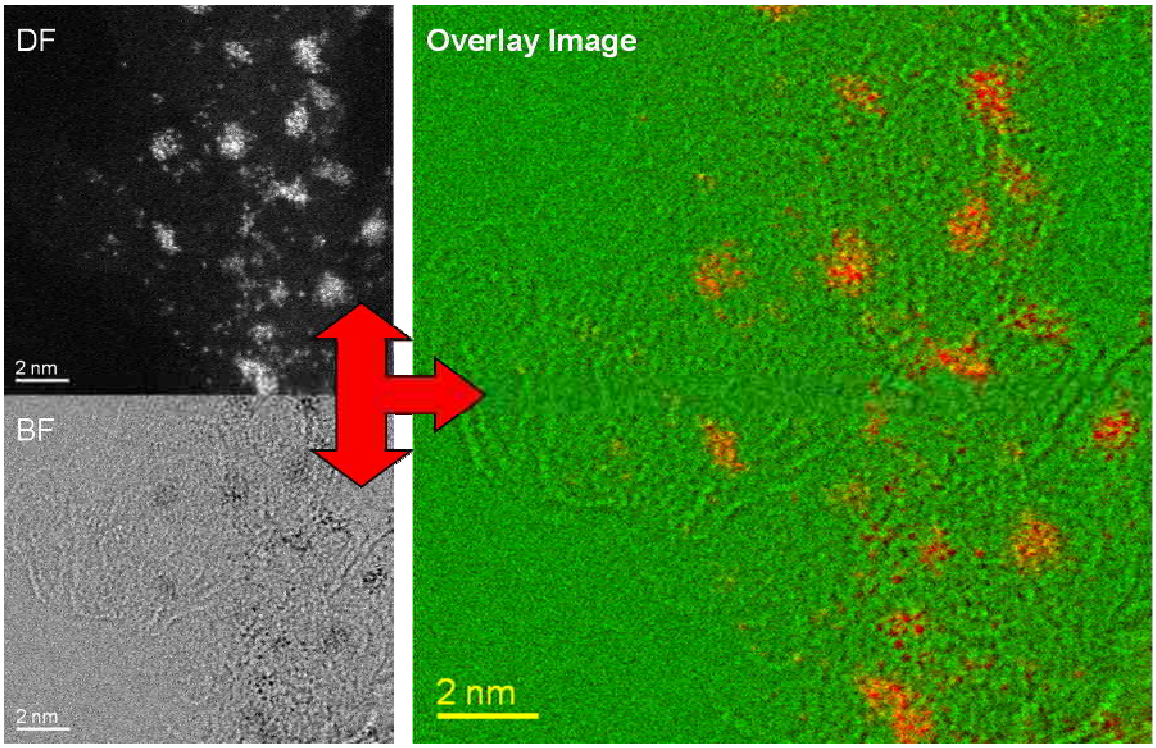

Figure 34 10wt% PtRe on Norit Carbon before reaction (fresh). The overlay image is a combination of the Dark Field (DF) Image and Bright Field (BF) Image enhancing the areas of carbon occupied by the PtRe species. The PtRe are shown colored red in the overlay image.

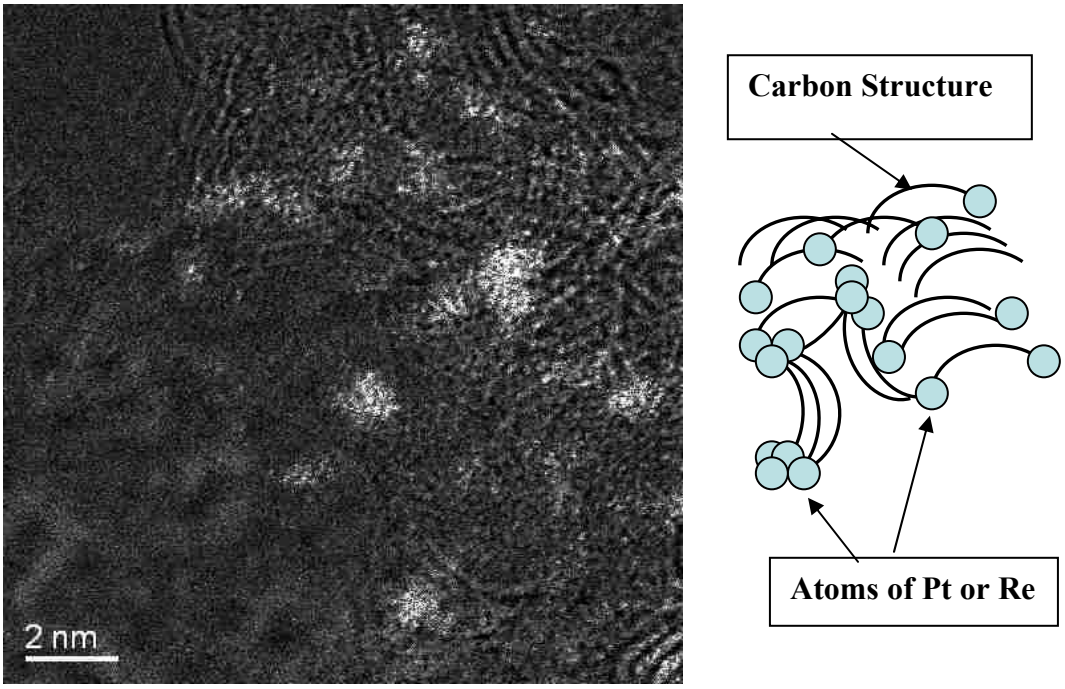

Figure 35 10wt% PtRe on Norit Carbon before reaction. Left is the image overlay of an area revealing Pt and Re species (white spots). Right is a schematic of where the atoms are seen to occupy the carbon structure.

An additional overlay image can be seen above with the white spots indicating PtRe metal. The metal was seen in both atomic and particle form with the particles forming at the areas with many edge sites meeting, as drawn in the schematic above. Although both catalysts supported fairly small particles of PtRe, both samples would have to be put through reaction conditions in order to determine which type of carbon structure would preserve the highly dispersed atomic metal species and small metal particles and also to determine via EDS the composition of the metal particles/atoms imaged.

4.3.2 STEM and EDX Analysis - Norit and Vulcan Carbon

Energy Dispersive X-Ray Analysis was performed on the Norit and Vulcan Carbons on three separate occasions: without any deposited metal, after going through

reaction with PtRe, and after heating with the deposited PtRe. A typical EDS spectrum for Pt and Re can be seen below, showing the corresponding X-Ray energies for Pt and Re. In our analysis we will use the L lines of the spectra, as Pt and Re M line peaks are close in proximity and can interfere with the analysis (in addition, sulfur is also close to the Pt and Re M lines).

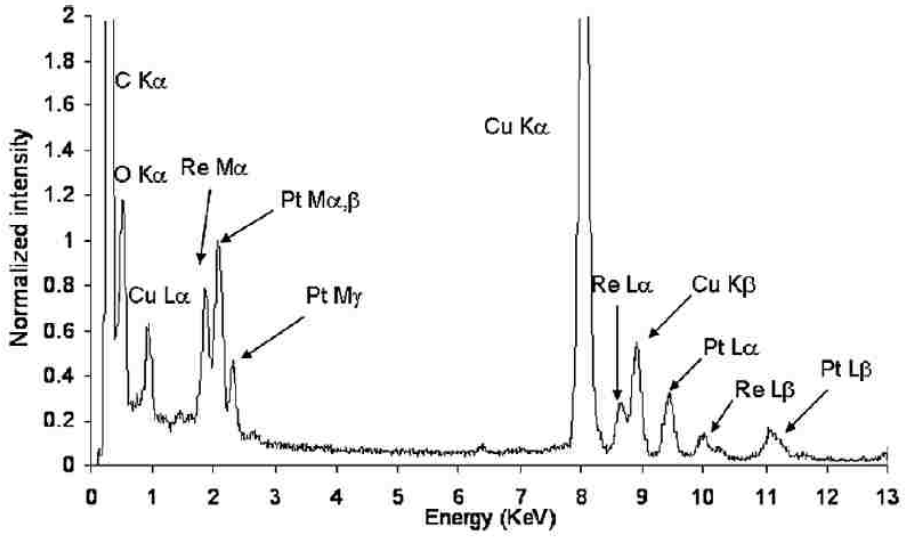

Figure 36 An example of an EDS spectrum revealing the Energies of the elemental peaks (C, Pt, and Re) we will be analyzing in our study. Provided by [47].

4.3.2.1 EDS Analysis-Carbon Only

Compositional analysis was performed on the both the carbons without any added metal to determine what elements these carbons had before impregnation. The Vulcan Carbon was seen to contain a small amount of contaminating elements, with sulfur having a consistently large peak, corresponding to roughly ~.05wt%. This sulfur content

has been observed before in Vulcan Carbon and came as no surprise from our analysis[52].

Element	C	O	Si	S	Cl	K
Average	92.54	7.359	0.013	0.044	0.002	0.001

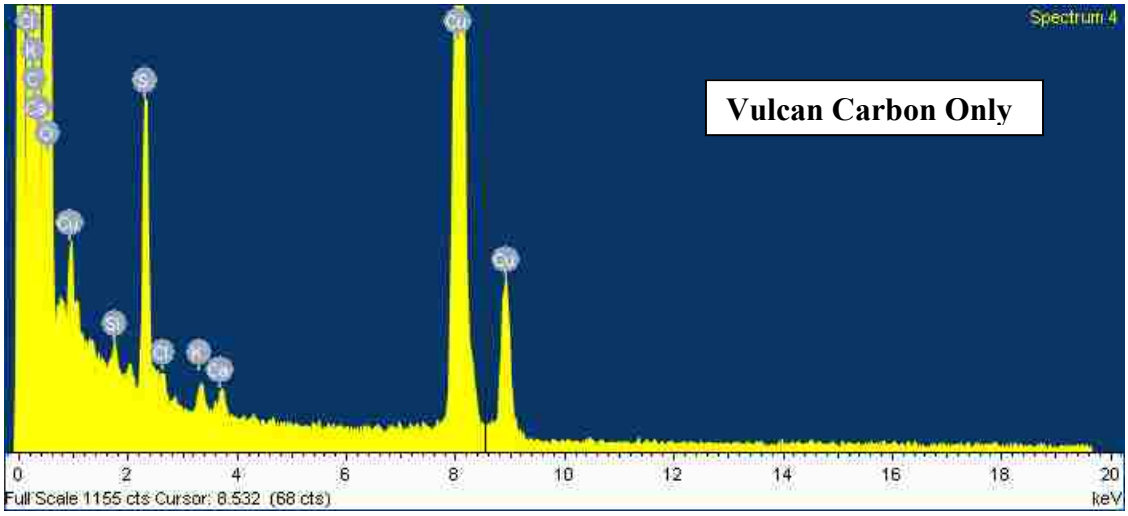

Figure 37 The elemental spectra obtained for Vulcan Carbon only with no metal added. The sulfur content is about ~.05wt%.

EDS analysis performed on the Norit Carbon revealed a small amount of elements, most likely contaminants. The sulfur content was lower than that of the Vulcan Carbon, close to 20% of that value.

Element	C	O	Si	S	Cl	Cu
Average	91.91	8.02	.02	.02	.01	.02

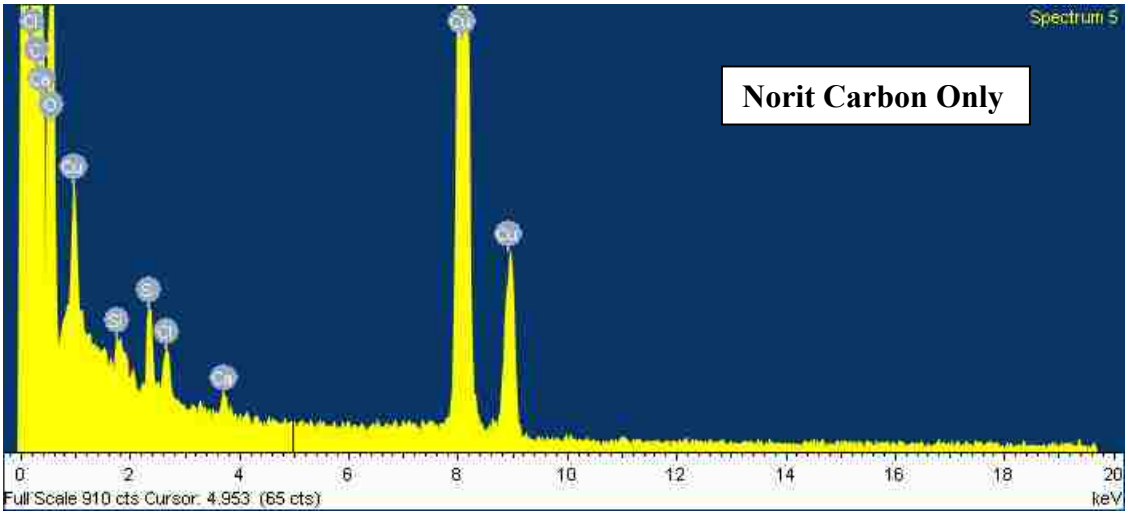

Figure 38 The elemental spectra obtained for Norit Carbon only. The sulfur content is about ~.01wt%, about a fifth of the amount seen in Vulcan.

The only difference seen compositionally between the two carbons was the sulfur content. This amount does not seem to affect the structure of the carbons nor the way the atomic and particle species of PtRe are dispersed on the carbon, but the composition may affect the reaction in selectivity and/or activity.

4.3.3 STEM and EDX Analysis - 10wt% PtRe *Vulcan Carbon* After Reaction

The 10wt%PtRe on Norit and on Vulcan carbon were both put through reaction conditions consisting of 60wt % Sorbitol at 0.04 cc/min at 230°C under 250 PSIG. The

PtRe Vulcan was put under these conditions for 5 days, while the PtRe on Norit was left in reaction conditions for 72 days. Additional experimental research was the reason for the difference seen in the amount of time the samples were under reaction conditions.

The 10wt% PtRe on Vulcan Carbon after reaction (or spent) was seen to contain small PtRe particles occupying the same areas where PtRe particles were imaged before in ACEM. The particles sintered and grew in the areas of less stacked carbon while the primary particles of carbon remained more or less clean of metal as seen in the figure below, causing a heterogeneous distribution of PtRe particles with a number average of 1.5nm. The PSD shown below was fitted to a log normal distribution function given as

$$y = y_o + \frac{A}{\sqrt{2\pi}wx} e^{\frac{-\left[\ln\frac{x}{xc}\right]^2}{2w^2}}, \qquad \textbf{(4.1)}$$

with the parameters for A, w, and C given in Appendix A. The program Origin made it possible to fit the data easily with 100 iterations.

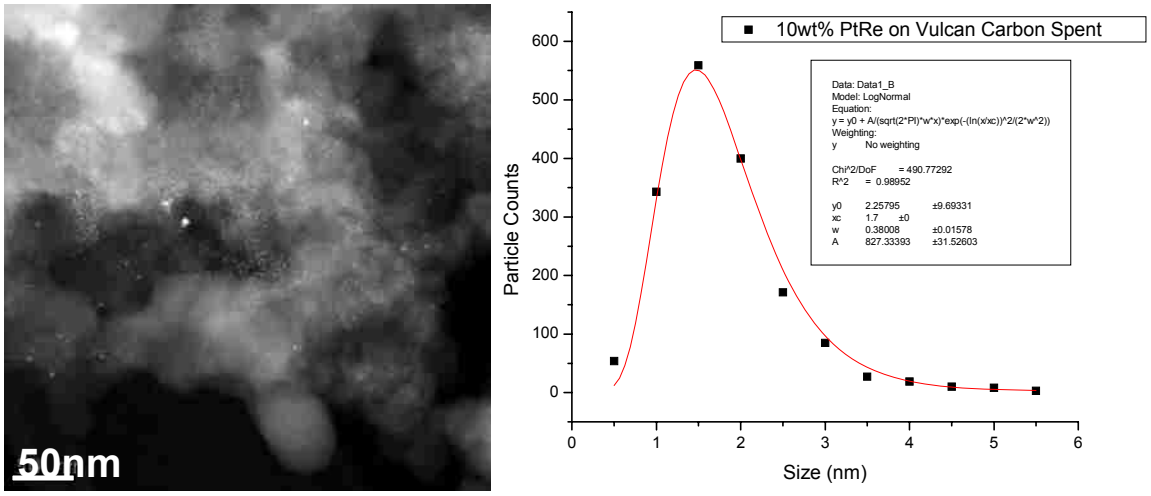

Figure 39 Left is an image taken by the STEM at UNM of the 10wt%PtRe on Vulcan Carbon after going through reaction for 5 days. Right is the Particle Size Distribution for the PtRe on Vulcan.

From the compositional analysis at low magnification (TEM mode, not STEM mode), EDS on Vulcan Carbon pieces in the ~5μm in size, an increased measurement of contaminants was recorded with both Ni and Fe present. The contaminants (Ni and Fe) were later found to be caused by residue from the reactor system which was made out of stainless steel. When only Pt and Re were included in the EDS analysis it was measured that the original amount of Pt deposited was still on the support (~5wt %) while the Re had decreased to half it's deposited amount (~2.5wt %). The loss in Re could be due to the Re sintering into large particles only seen on some areas of the carbon which were not included in the analysis, or due the Re becoming volatile and leaving with the reactants and products of the reactions.

Elements	C	Re	Pt
Average	92.9	2.8	4.3

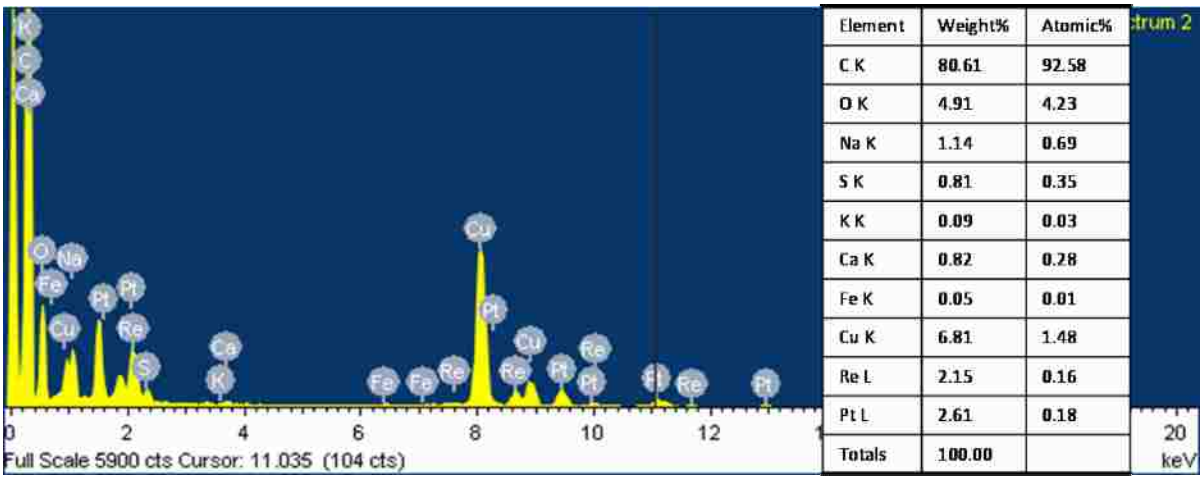

Figure 40 Spectrum of a carbon particle ~5µm in size on the 10wt% PtRe Vulcan Carbon Sample after reaction. Many elements are detected.

At higher magnifications in STEM mode particles went through an analytical analysis to get compositional information made possible by the small probe size. The average of the overall analysis revealed that that a majority of the particles (~1.5nm) were either rich in Pt or near 1:1 Pt:Re in composition. In some instances, as seen in the figure below, large particles (>3nm) of pure Re would be found on the support, but this case was rare in occasion. The Vulcan Carbon support by itself with no resolved metal species generally showed no traces of Pt, and very little Re.

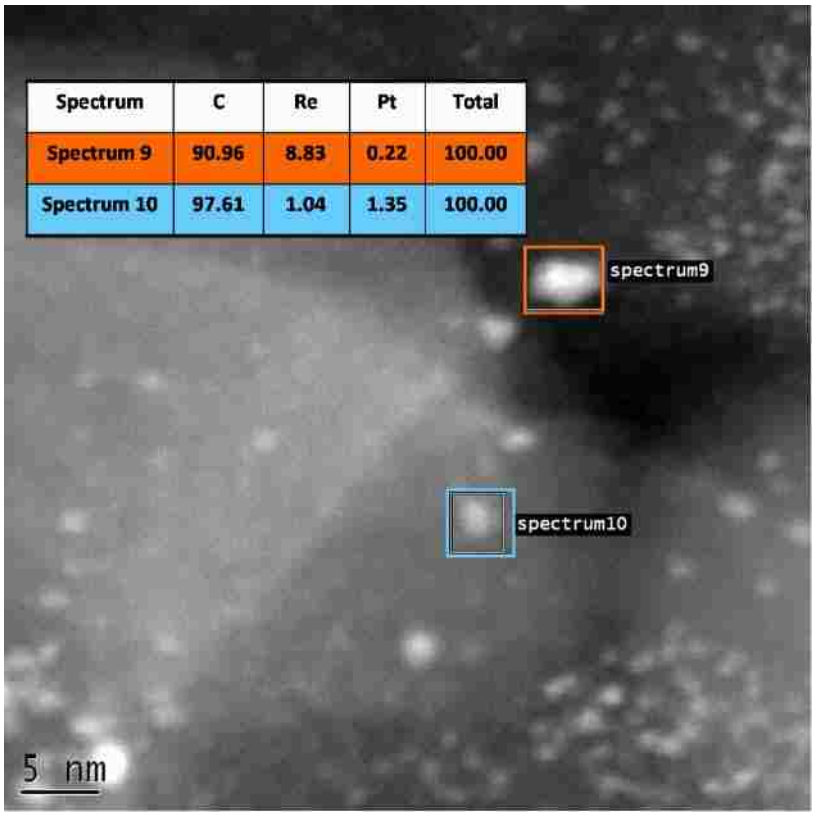

Figure 41 Compositional data gathered from 10wt%PtRe on Vulcan Carbon after reaction conditions. A majority of the particles were Pt rich (in blue), and some Re rich (orange).

The amount of X-Rays collected for an individual particle was low due to the weaker signal the beam generated off of an extremely small area. The low signal was the cause for the average wt% of Pt to decrease at high magnification, while overall analysis at low magnification detected the entire Pt deposited with the stronger beam.

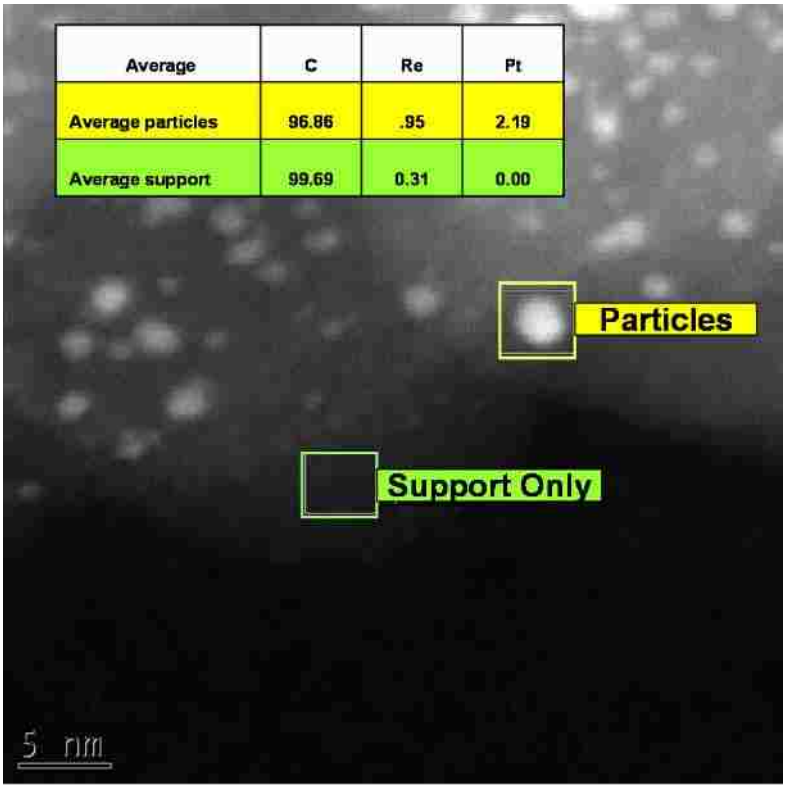

Figure 42 10wt% PtRe on Vulcan Carbon showing the different areas captured by EDS analysis. The green square contains only support while the yellow square contains an entire particle. On average the particles were rich in Pt, with only small amounts of Re and no Pt seen on the support alone.

4.3.3 STEM and EDX Analysis - 10wt% PtRe on *Norit Carbon* After Reaction

The 10wt%PtRe on Norit, as discussed above, was put through reaction conditions consisting of 60wt % Sorbitol at 0.04 cc/min at 230°C under 250 PSIG for 72 days. A similar type of EDS analysis was performed by first analyzing the sample in TEM mode (low magnification) of large micron size carbon pieces. The spectra revealed the presence of several possible contaminants – S (small), Fe, Nb, and possibly some Ni. When only the elements of interest were included in the analysis, Pt, Re and C, the

overall metal loading of 10-12 wt% was calculated (see table below). The overall analysis was different than the Vulcan Carbon, as Norit Carbon appeared to have no loss of Re at all, giving an indication Norit Carbon was keeping the metal on the surface and hence could already be an improved support.

Element wt%	C	Re	Pt	Total
Average	**88.2**	**5.3**	**6.3**	**100.0**

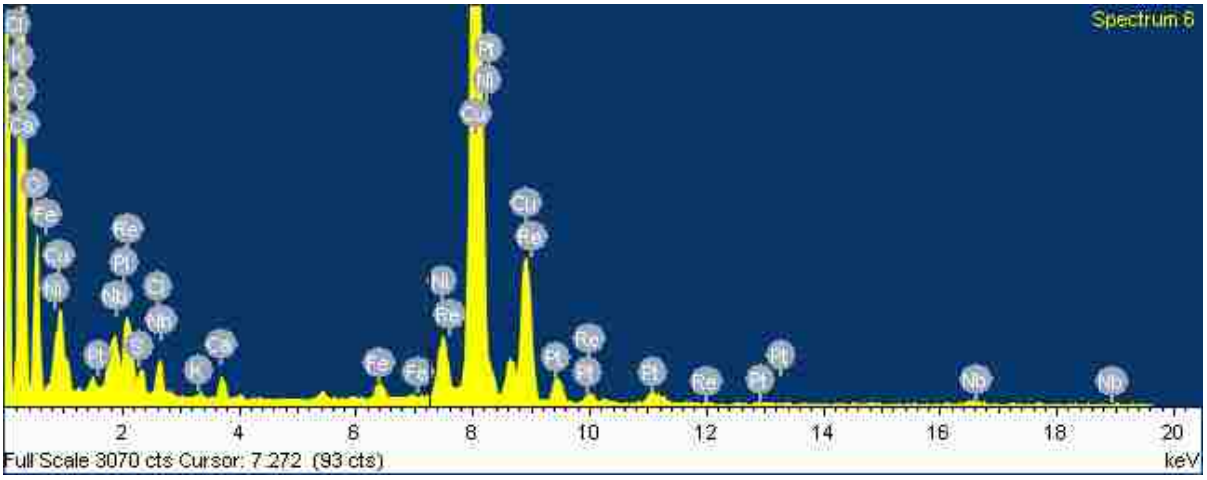

Figure 43 Spectrum of a 10wt% PtRe on Norit Carbon after reaction at low magnification, carbon particles ~5µm in size.

When analysis was performed in STEM mode, imaging revealed small metal particles had formed with an average size of ~1.5nm with a small increase in stacking seen of the Norit Carbon support. The PtRe particles were imaged to be homogeneous in dispersion on the Norit unlike the Vulcan Carbon. Increased magnification and EDS spectra determined large white spots (large particles >10nm) imaged were contaminants such as Ni and Fe due reactor residue.

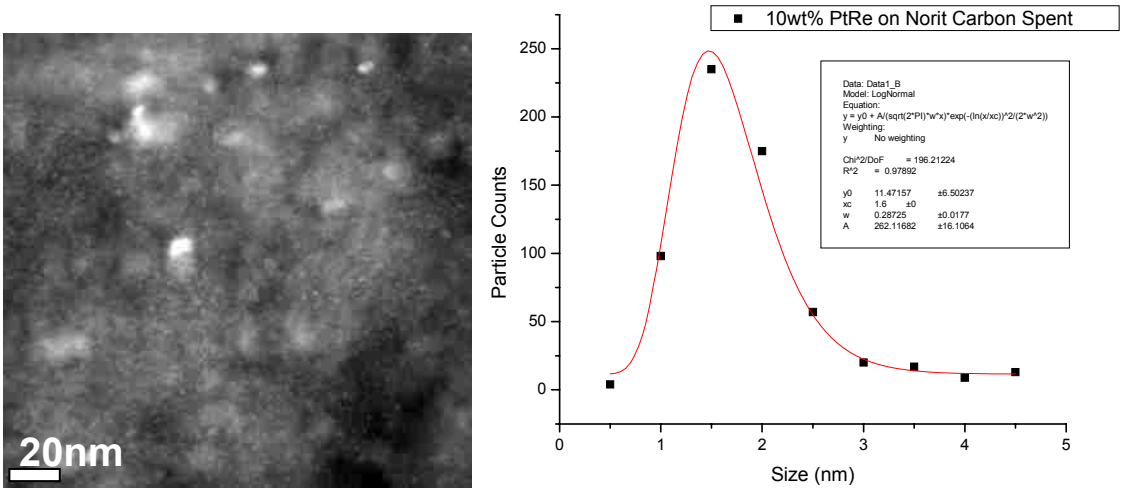

Figure 44 Left is a STEM image taken at UNM of the 10wt%PtRe on Norit Carbon after going through reaction for 72 days. Right is the Particle Size Distribution for the PtRe on Norit, with a number average size of ~1.5nm fitted with a Log Normal Function.

EDS performed on particles (~1.5nm) revealed mostly Pt and a lower amount of Re. Analysis of the carbon support in the vicinity of the metal particles, where no obvious metal particles are seen, showed significant amounts of Re present. Putting the two analyses together, we can account for the location of the Pt and Re in this sample, with the Pt and half the Re being in particle form with the remaining Re dispersed on the support.

Average Overall	88.2	5.3	6.3	100.00
Average Particles	91.43	3.58	5.00	100.00
Average Support Only	95.7	3.5	.22	100.00

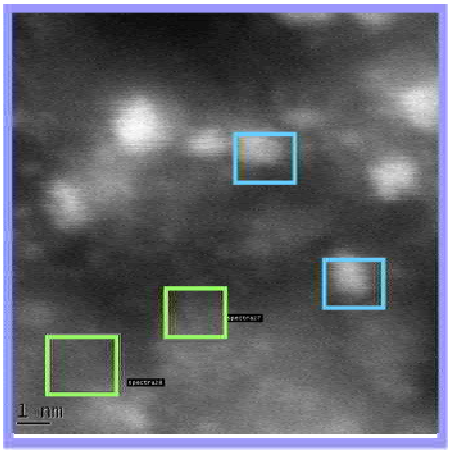

Figure 45 10wt% PtRe on Norit Carbon showing the different areas captured by EDS analysis. The green squares contain only support while the blue squares contain entire particles. The blue squares have mostly Pt while the green have mostly Re.

The Norit carbon showed significant amounts of Re unresolvable to the JEOL FEG STEM but imaged in an Aberration Corrected STEM. The differences in dispersion and the ability to maintain Re on the Norit can be attributed to carbon structure with dispersion seen to increase with the increasing amount of edge sites provided by the support.

4.3.5 STEM and EDX Analysis-10wt% PtRe on Norit Carbon Heated to 700°C and 900°C

4.3.5.1 Heated to 700°C

Both samples of PtRe on Vulcan and Norit after reaction (spent) were heated to 700°C at a rate of 10°C/min under 3%H_2 (balance N_2) and held there for 10hrs in order to test the stability of the atomic and particles species on the support and to observe changes in support structure due to exposure to the heat. It was measured on the heated PtRe Vulcan sample that the Pt to Re ratio (2:1) had remained the same, with in increase seen

in measured particle size. Since no significant difference was measured for the Vulcan sample, focus was turned onto the Norit Carbon, where atomic Re species had first been detected and seen by the ACEM.

The overall low magnification (TEM mode) EDS analysis of the PtRe on Norit focused on carbon pieces on the size of ~5μm with an average of 1:1 wt% of Pt:Re. As shown in the image below the PtRe metal particles had grown significantly in size with only minimal carbon support visible, thus increasing the overall calculated wt% of the metal.

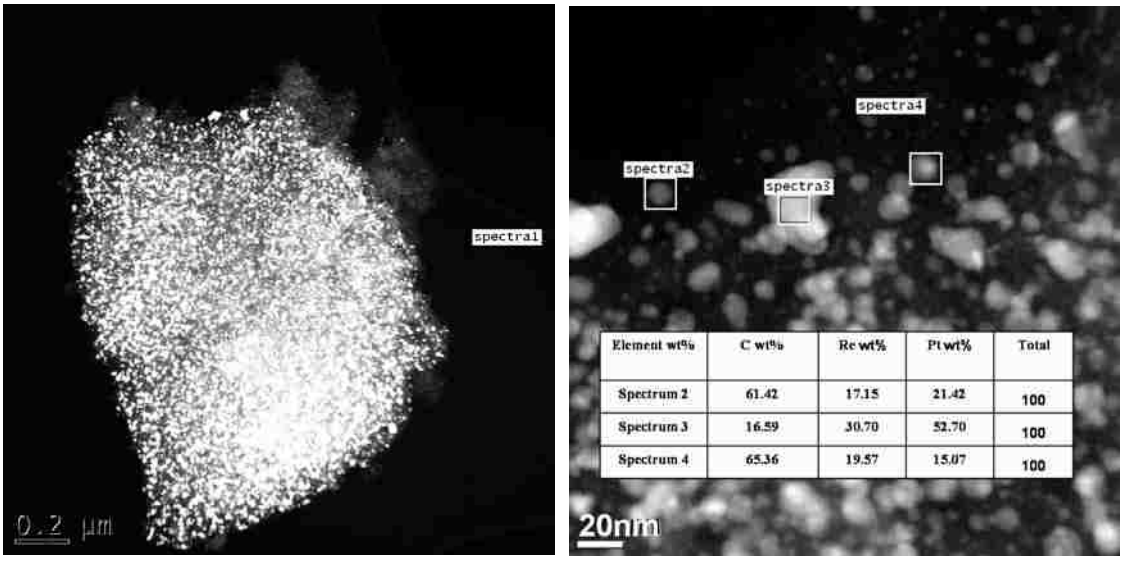

Element wt%	C wt%	Re wt%	Pt wt%	Total
Spectrum 2	61.42	17.15	21.42	100
Spectrum 3	16.59	30.70	52.70	100
Spectrum 4	65.36	19.57	15.07	100

Figure 46 10wt% PtRe on Norit Carbon after reaction and after heated at 700°C for 10hrs. The left image is a low magnification image of the sample revealing the large PtRe particles on the sample. The right image is the EDS spectra of three different particles, all heavy in metal species, with the larger particles (>20nm) measured to be slightly Pt rich.

It appeared that the Re was becoming more and more unstable as the carbon support became more and more stacked due to the heat treatments. As the Re species became less stable on the carbon structure, it sintered with the already present Pt particles.

4.3.5.2 Heated to 900°C

Further heat treatments at 900°C for 24hrs under similar conditions (3%H_2 balance N_2) increased the particle size once again with an overall 1:1 ratio for Pt to Re, with large micron pieces of Fe and Ni now appearing in the sample. This was the overall averaged ratio, but STEM probe analysis provided evidence that smaller particles (<20nm) were either rich in Re or 1:1 in composition, while larger particles (>20nm) appeared to be rich in Pt as seen below.

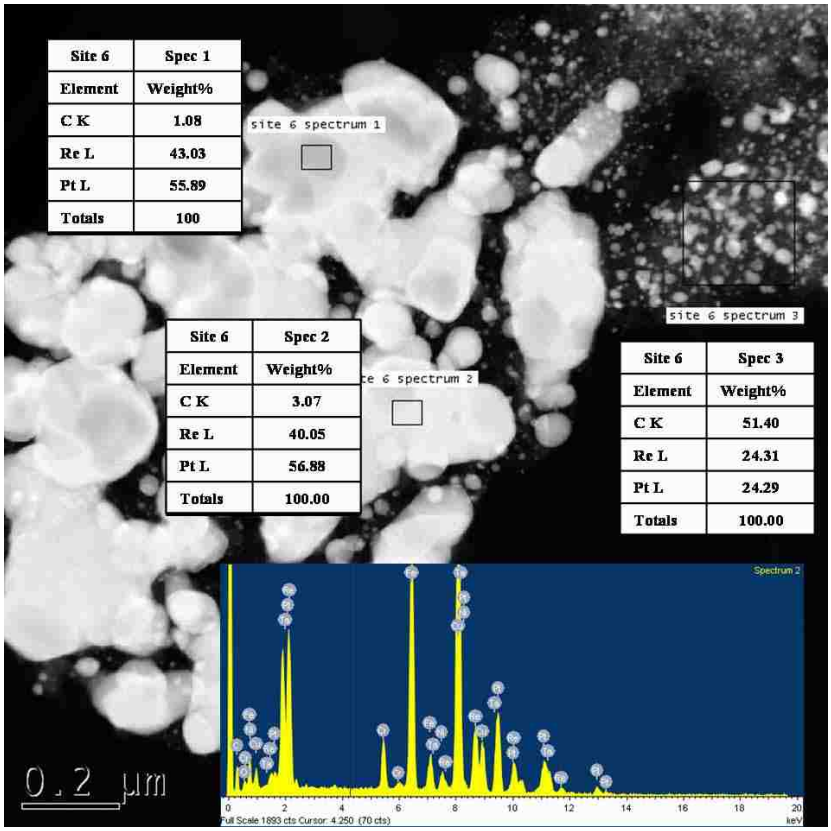

Figure 47 STEM image of the 10wt% PtRe on Norit Carbon after reaction and after heated at 900°C for 24hrs. The very large bright particle in the middle is Pt rich with large amounts of Fe and Ni to be found. The more dispersed particles on the top right are more 1:1 Pt:Re in composition.

The 1:1 average ratio for the metal gave evidence that no metal was being lost, but the continued increase in particle size revealed the carbon itself may be continually losing its initial structure and edge sites that maintained the atomic species. The large chunks of Fe and Ni appeared to be contamination or pieces from the reactor sintering after being exposed to the high temperature. Further analysis revealed no remaining atomic Re species on the support and all the metal was in particle form.

Line scanning performed by EDS revealed that the particles were overall homogeneous in nature with both Pt and Re species not distinctly separated, but distinct lines in contrast could be observed. This type of composition is not typically seen as previously measured and displayed in the phase diagrams of Pt-Re below. According to both diagrams, there is a miscibility gap directly where our PtRe particles lie. The reason for composition of our particles may be due the size and how they were formed during heating.

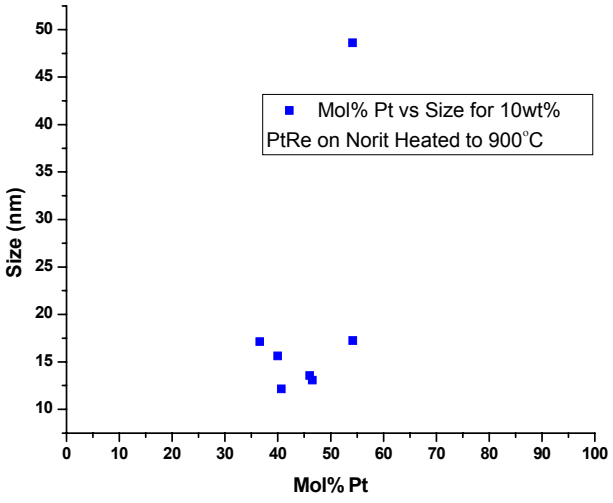

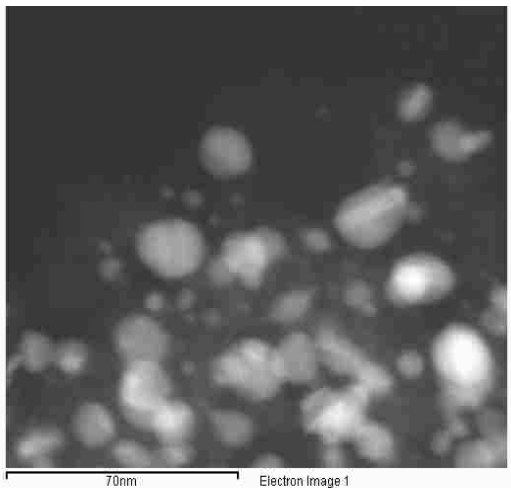

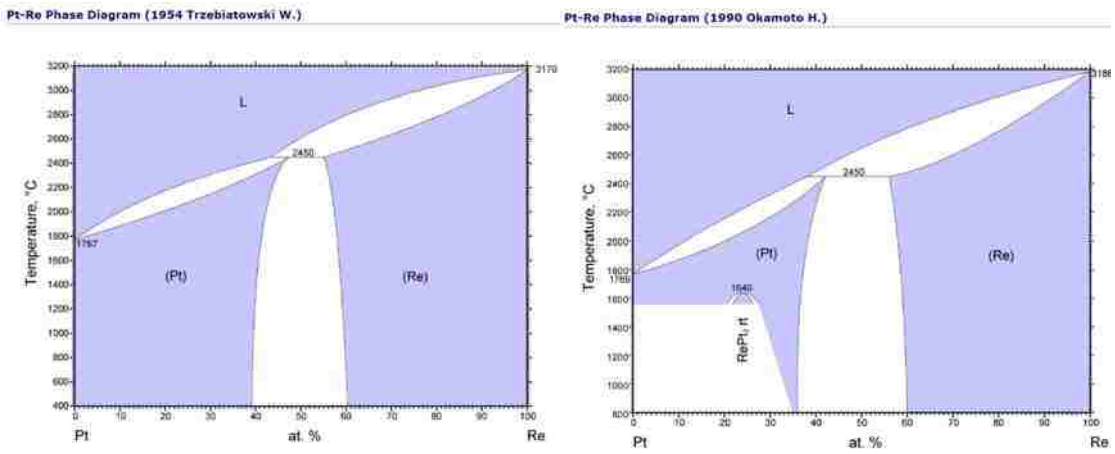

Figure 48 Graph (above left) of Size vs. Composition for our measured particles of PtRe on Norit heated to 900C. Above to the right is an image of the sample revealing the contrast seen in the PtRe particles. The phase diagrams (below)[53, 54] reveal a miscibility gap where are PtRe particles are measured to exist.

Further analysis of this sample was performed by ACEM in order to determine the reason behind the differences in contrast seen in the PtRe particles. ACEM STEM images revealed the difference in contrast of some particles was due to a change in the crystalline structure of the particles or twinning, as seen before by Gontard[55] for Au particles. It was also recorded that the carbon structure had also changed, becoming more amorphous than structured, giving additional evidence to why the Re may become less stable on the support at higher temperatures.

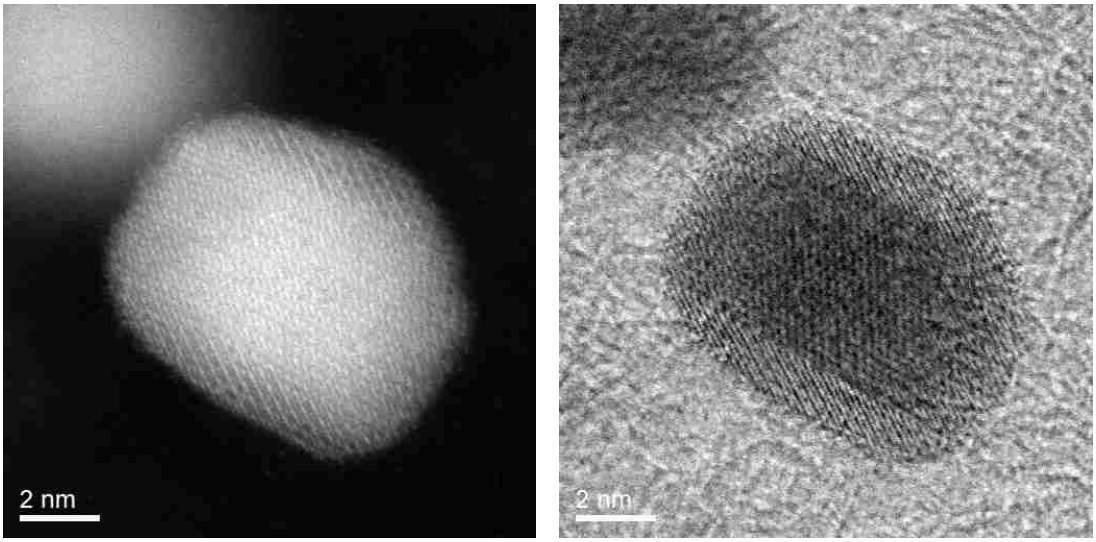

Figure 49 ACEM STEM image taken at ORNL showing the cahnge crystalline structure. The structure changes the contrast of the PtRe particles seen on the Norit Carbon heated to 900°C.

4.4 PtRe Conclusion

It was shown by ACEM and EDS analysis that the pure Vulcan and Norit Carbon supports were different in structure, but chemically very close in composition. The Vulcan Carbon contained larger primary particles and stacked regions of carbon while the Norit Carbon consisted only of roughened disordered structure (edge sites). The atomic species of Re adsorbed to these edge sites giving a large population of atomic species, giving evidence that edge sites can provide a more stable region for atomic adsorption. The differences in structure also determined if the deposited Pt and Re metals would disperse homogeneously or not.

The Pt and Re on the Vulcan Carbon support still remained heterogeneous in distribution after reaction and continued to maintain that distribution after heat

treatments. A loss in Re was also measured after reaction and can be explained by the small amount of edge sites/adsorption sites and the presences of a volatile Re species.

It was determined by EDS and STEM on the JEOL at UNM that the Norit Carbon after reaction evenly dispersed half of the Re in atomic species and in the particles, while the Pt preferred to be in particle form (~1.5nm). The highly dispersed atomic Re could be due to the Re being easily oxidized on the surface edge sites, making ReO_x on the surface as the distinct separated atomic species[56].

After reducing heat treatments to 700°C and 900°C of the PtRe on Norit Carbon after reaction, the Re became unstable and sintered with the already present Pt particles. This sintering was due the change in carbon structure imaged with the carbon first becoming more stacked then amorphous. There is also the possibility of the ReOx reducing in the heated environment which may cause the Re to be less stable.

The presence of Pt nanoparticles with a dispersed atomic Re species that form an inter-metallic after heating are seen to be the opposite of simulated results calculated by Helfensteyn[57] and Guofeng[58]. The simulated results calculated that Pt would prefer the lowest coordination number and adsorb to already formed Re particles at the kinks or step edges. The particles from simulation shown below reveal how the Pt would adsorb, first making a shell covering the Re atoms in the core. This calculation was seen to be completely opposite compared to our experimental results where Re was determined to be the atomic species present with the Pt preferring to make particles. The difference may be due to the restrictions on the simulation and also to our Pt and Re interactions with the carbon.

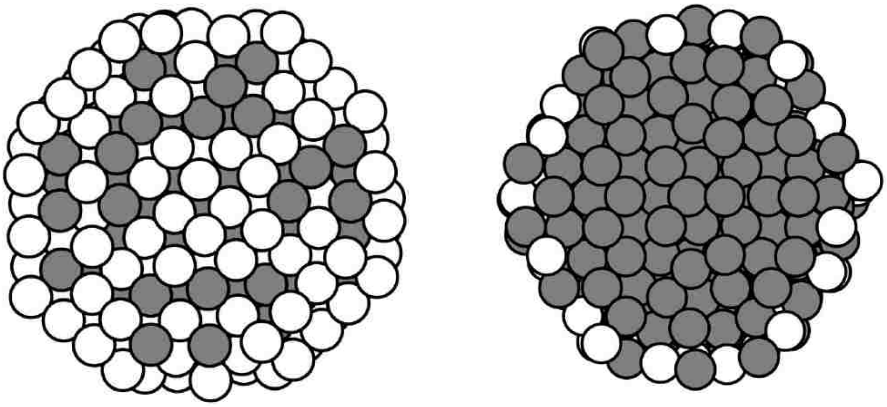

Figure 50 Monte Carlo simulation by Guofeng[58]: The left nanoparticle has a completely covered platinum (white) shell when the composition is $Pt_{75}Re_{25}$, while the particle on the right is $Pt_{25}Re_{75}$.

The results of the experiments revealed how a carbon structure with numerous edge sites can aid in dispersing both Pt and Re. It was also seen that high temperature treatments which change the carbon structure and reduce the Re make the atomic Re species unstable and make it favorable to sinter with the Pt particles, making an inter-metallic. Additional studies performed (Appendix B) with metals other than Re on carbon has also shown how the support helps disperse that metal species.

CHAPTER 5

5 The Stability of a Ni/MgA_2O_4 Catalyst

5.1 Introduction

The steam reforming of methane is one of the key processes in the production of synthesis gas and hydrogen [59]. This process has witnessed an increase in demand due to the growing need for energy and clean fuels with processes such as Fischer-Tropsch Synthesis[60], hydrodesulfurization and with the push towards a hydrogen economy[61]. A nickel based catalyst is the catalyst of choice for methane steam reforming. The catalyst has to endure high temperatures of up to 900°C and pressures of up to 40 bar. While enduring such harsh conditions the catalyst is susceptible to poisoning, coking, and sintering which can result in a dramatic loss in active surface area. Sintering is often seen as the major irreversible cause of catalyst deactivation and therefore a mechanistic understanding is essential for developing catalysts with longer lifetimes. Metal particle sintering occurs via particle migration and coalescence or Ostwald Ripening[7].

Current understanding of sintering suggests two dominant, and distinct, mechanisms of sintering: Ostwald ripening, wherein smaller particles diminish or vanish and larger particles grow in size, and migration and coalescence, wherein diffusive mobility of particles and ensuing collisions amongst them causes a growth in particle sizes. In as much as both the mechanisms lead to an overall increase in average size and decrease in surface area, theoretical analysis of these mechanisms has shown that it is

possible to identify the underlying mechanism of sintering based on the shape of particle size distributions and the kinetics of decay in surface area.

Particle sizes evolve during sintering and give rise to distributions with asymmetric shapes. Granqvist and Buhrmann argued that the distribution arising from migration and coalescence can be described by a log-normal model [9] which has a distinct peak at smaller particle sizes and a long tail towards larger particle sizes. On the other hand, the distribution arising from ripening of particles is shown to have a shape with a tail towards smaller particle sizes and a peak at larger particle sizes, such that the maximum particle size observed is either 1.3 or 1.5 times the size of the most abundant particles, depending on the limiting conditions of ripening. So, given these differentiated manifestations in the particle size distributions, a lot of studies have been able to predict the mechanism of sintering in their respective systems. However, there have been differences in opinion about this methodology of mechanism prediction, and far too many of the observed distributions appear to indicate migration and coalescence mechanism of sintering [21]. Even in the case of $Ni/MgAl_2O_4$ such predictions indicate migration and coalescence to be occurring predominantly[62].

Yet another manifestation of a difference in mechanism appears in the kinetics of decay of surface area of sintering particles. The decay in surface area of supported Ni during sintering has been studied earlier for MSR conditions [14, 15]. Employing theories of particle migration and coalescence and theories of ripening of particles a universal power-law model of kinetics of surface area has been developed [17]. Of key interest in this model is the exponent "*n*" that is dependent on the dominant mechanism of sintering. Typical values of "*n*" are between 3-5 for ripening and between 2-13 for

migration and coalescence[7]. In these two studies [14, 17] on surface area of supported Ni particles this exponent was noted to decrease from a high value to a low value over the duration of sintering. As such, both these studies concluded that sintering during initial stages (characterized by large exponent "*n*") was dominated by particle migration and coalescence. Subsequent sintering was claimed to be happening through ripening. There were some aspects of these two studies on surface area of Ni particles that are different, but the kinetics behavior was similar. However, a more direct corroboration such as observation of ripening of particles and migration and coalescence of particles causing sintering is lacking in these two studies.

In the light of aforementioned limitations of earlier studies on sintering in $Ni/MgAl_2O_4$, a different study is needed that utilizes current advances in high resolution microscopy to probe sintering mechanisms in parallel; direct observation of behavior of individual particles, and collective behavior of system parameters such as particle size distributions and surface area. In the absence of in-situ experiments most of the mechanisms noted in model as well as realistic catalysts are either deduced or inferred. .

Direct observation of events characteristic of the mechanisms responsible for particle sintering are few and insufficient in information. Baker demonstrated that catalyst observation under high temperature were possible[26] and under a gaseous environment [25]. The work by Crozier et al [63] also performed in-situ TEM observations of sintering, but they relied on observations before and after high temperature treatments. More recently, using the advanced in-situ microscope available at Haldor Topsøe A/D, Hansen[28] was able to capture real-time sintering events at a high resolution at conditions approaching those of steam reforming of methane. The

work focused on the later stages of sintering, when most of the small particles had already disappeared due to experimental limitations and focus of that research.

In the present study, an in situ environmental microscopy having a combination of high spatial resolution for probing extremely small nanoparticles and a fine temporal resolution for probing fast events will be employed in our study of sintering. We employ an industrially relevant system consisting of Ni particles supported on $MgAl_2O_4$ under steam reforming conditions and study events during the early stages of catalyst sintering. Direct probing of particles and events involving particles will form our basis for analyzing the mechanism of sintering in this catalyst system. In addition, these analyses will be compared with established methods of prediction of sintering mechanisms, as discussed earlier, to highlight the limitations of those methods. Further arguments on these limitations will be made using results from deterministic and probabilistic (Monte Carlo) simulations of ripening of supported nanoparticles.

5.2 Experimental

5.2.1 Catalyst Preparation:

In-Situ experiments were performed on a twice impregnated 12wt% $Ni/MgAl_2O_4$ catalyst using environmental transmission electron microscopy (ETEM). A twice impregnated (~12wt%) Ni on spinel was used instead of a typical industrial 1wt% in order to increase the number of particles that could be characterized and to increase the likelihood of recording a sintering event. The increase in the Ni amount should not greatly affect the overall sintering behavior, as mentioned by Sehested[16]. A nickel

formite precursor was added to a $MgAl_2O_4$ support ($5m^2/g$) via wet impregnation to obtain a ~12wt% Ni catalyst. The sample was then calcined in air to get a NiO on the support. The catalyst was later reduced in the microscope to get a $Ni/MgAl_2O_4$ catalyst. Previous EELS experiments performed at Haldor Topsøe A/S[28] on a 22wt% $Ni/MgAl_2O_4$ sample proved the Ni oxide had completely reduced to Ni metal.

5.2.2 In-Situ Experiments:

The measurements were perfomed using a Philips CM300 FEG ETEM working at 300kV at the industrial catalyst company Haldor Topsøe A/S in Lyngby, Denmark. The microscope was fitted with a GIF200 and Tietz F114 camera for both normal imaging and Energy Filtered imaging and for low intensity image collection. It was possible to perform TEM imaging at pressures of up to 4mbar under *in-situ* conditions and temperatures of up to 750°C while obtaining a resolution of .14nm.

Plasma-cleaned stainless steel grids were used for mounting the powder as they are inert to the conditions used during the sintering process. A new grid was used for each experiment and the grids were simply "dipped" into the catalyst powder (no ethanol used) and then mounted onto a GATAN heating holder. The GATAN holder was used due to its inertness to experimental conditions in the TEM chamber, especially in any type of oxidizing conditions. The TEM grid was held in place with a washer and screw made specifically for the holder. The holder heating element was controlled with a controller box, capable of reading out the grid temperature and executing a desired ramp rate. The holder was also equipped with connections to a small water pump for cooling

and maintaining a stable temperature. The affect of temperature and pressure on the sample grid itself can be seen in Appendix A.

The samples were imaged at different points in the experiment: directly with no environmental treatment, after a reduction in 1.8mbar H_2 at 500°C for 30minutes, after the introduction of 1.8mbar H_2O at 500°C (3.6mbar total 1:1 H_2:H_2O), and finally after reaching a temperature of 750°C at 3.6mbar 1:1 H_2:H_2O. All temperature ramp rates were set to a rate of 50°C/min for consistency. Additional experiments were also performed with a maximum temperature of 650°C to test for sample reproducibility. The introduction of each gas was measured by mass spectrometry.

All images were obtained using the TIETZ camera due to its ability to obtain images at low beam dose compared to the GIF camera. The movies and images collected had a wide variety of collection times and were optimized to get the best imaging possible at that particular point in time. All images obtained were analyzed using Digital Micrograph and the contrast and brightness would be enhanced to increase the quality of the image. Each particle contributing to the calculations and PSD was measured twice, and the nominal average of that number was the one plotted. An average of 200 particles were counted for each sample at each stage of image collection. The deviation of the measurement varied from .1-.5nm depending on the size of the particle and the quality of the image. The magnifications used during image collection varied from x60k up to x360k. Particle size distributions and "before and after" image sets were collected at a magnification of x100k, while particle shape analysis at a profile view used a magnification of x240k or higher as seen in figure 50.

The movies recorded could be varied in their collection rate depending on what the user desired, from an image being collected every 100-500miliseconds. The process of movie collection could be started and ended at the user discretion, giving us the choice of when, what area, and for how long a movie should be collected. The movies themselves were recorded at many different stages of the experiment, including times of reduction, after the introduction of water, and after reaching the desired temperature. In our studies we would focus on the time period of when the sample had just reached temperature (750°C) under 3.6 mbar H_2O:H_2 and up to three hours after that to determine and record the actual sintering mechanisms. The movies could be separated into their individual image frames and analyzed using Digital Micrograph.

Experiments were also performed with the beam off during the long ageing times, and also with it on. There was no difference measured in particle behavior or PSD when comparing the two methods of collecting information. The support on the other hand ($MgAl_2O_4$) did appear to change and deform after pro-longed exposure to high intensity beam conditions.

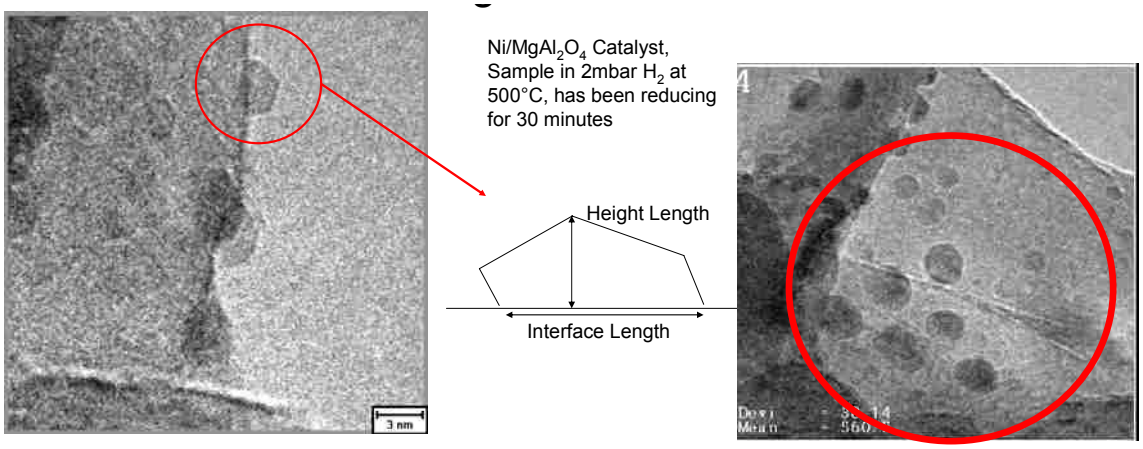

Figure 51 Left: Typical image used for particle shape analysis. Right: Standard image used for a Particle Size Distribution. Sample is of the Ni/$MgAl_2O_4$ catalyst after reduction for 30min in 2mbar H_2.

5.3 Results for 650°C experiments

The nickel catalyst was first imaged as is with no environmental treatment to obtain images of the support and to assure that there was enough catalyst on the sample grid. The sample was then exposed to 2mbar H_2 in-situ while the beam was off. Once the gas pressure had stabilized, the holder was heated to 500°C at 50°C/min. Once the temperature reached 500°C the sample was left to reduce for 30 minutes under those conditions. The beam was then turned on and the images were taken at varying magnifications after the reduction had completed. 2mbar H_2O was then introduced into the system after the reduction images were collected. A mass spectrometer was used to monitor the amounts of H_2 and H_2O in the system during the entire experiment. Images were again taken after the pressure of the H_2O had stabilized in the system. After this, the temperature was ramped up to 650°C at 50°C/min. Images were then taken immediately after the temperature had reached 650°C and the sample was stable enough

to be imaged (~10minutes). Thirty minutes after the first image was taken, images were taken of the same area (before and after images). A pathway of where images were taken can be seen in the diagram below, which is the same for the imaging performed at 750°C.

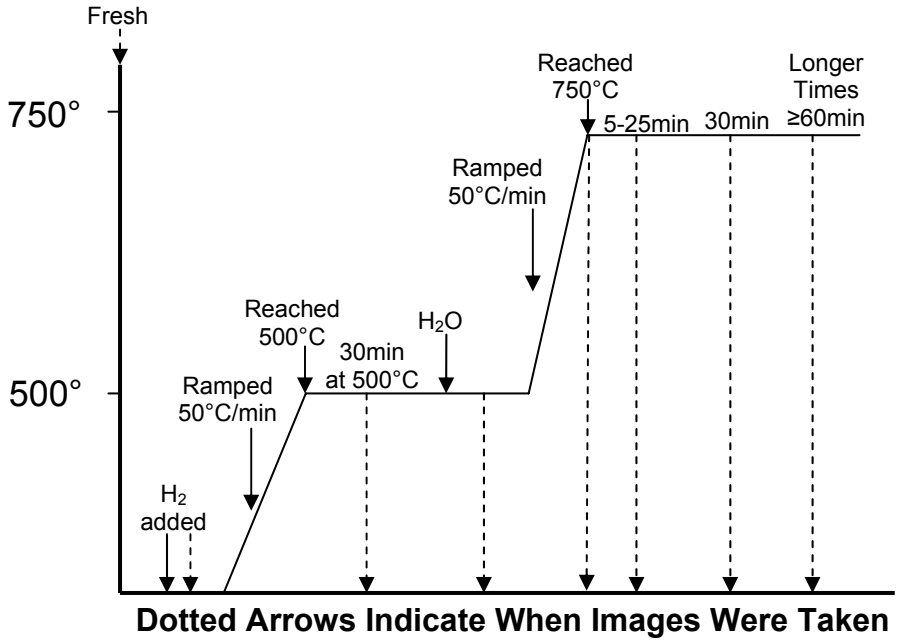

Figure 52 Points at when images could be taken during the *in-situ* experiments on Ni/$MgAl_2O_4$ are indicated by the dotted arrows

The experiments performed with a maximum sintering temperature of 650°C in with 4mbar 1:1 H_2:H_2O resulted in a slight shift in the PSD to a larger particle size with a tail skewed to large particles and almost no particles below a diameter of 3.5nm were seen as shown in the figure below. This result was expected as previous experiments had revealed similar behavior at varying sintering temperatures[16, 17, 39, 59]. The log normal type particle size distribution was continuously seen throughout the sample just after the temperature had reached 650°C with instances when larger particles (>5nm)

were seen on the support near areas of dense populations of small particles. Observations of the sample directly after reaching 650°C revealed an increase in Ni particle size with an average particle size of about 5.6nm. After 30 minutes of exposure to conditions the Ni particles continued to increase in size, with a broader distribution as a result.

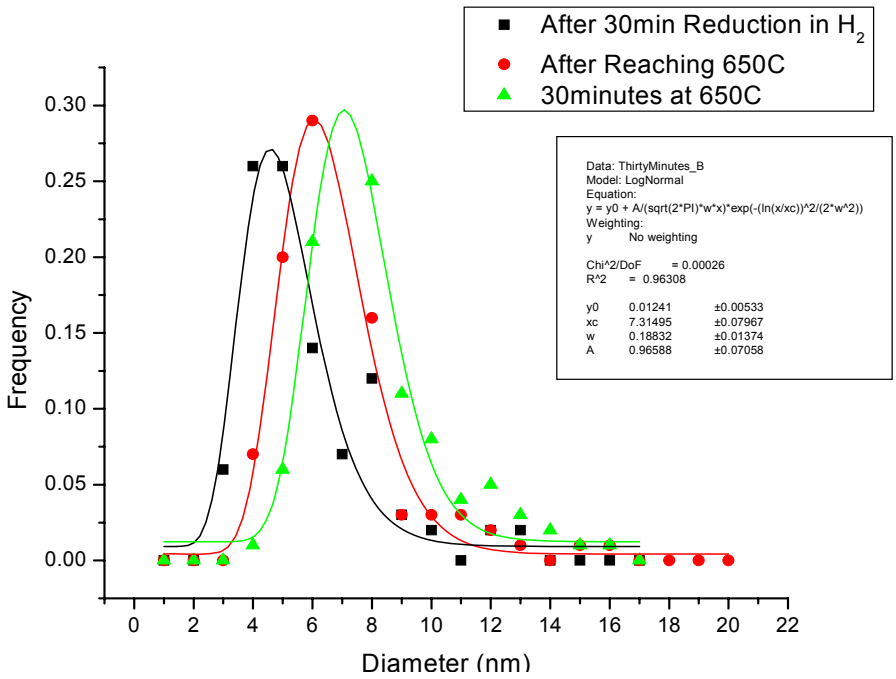

Figure 53 Particle Size Distribution of Sample a 12wt% Ni/$MgAl_2O_4$; □ Reduced for 30min at 500°C in 2mbar H_2, ○ After reaching 650°C in 4mbar 1:1 H_2:H_2O, and Δ after 30min at 650°C in 4mbar 1:1 H_2:H_2O. All distributions have a tail towards larger particles and have been fitted with a Log-Normal function (Eq 4.1).

The before and after images taken revealed several particles ($d \geq 5nm$) that had remained in the same location after 30 minutes of exposure to the environmental conditions. The particles shown in figure 53 also grew in size after 30 minutes, while particles with a smaller diameter had disappeared. A calculation of the amount of Ni in this area revealed that almost all of the Ni in the "before" image had remained in that area according to the "after" image. The formation of "new" larger particles can explain why

the total amount of Ni remained the same, as the images give evidence that the small Ni particles had either coalesced into larger particles or ripened away at the expense of the already present larger particles.

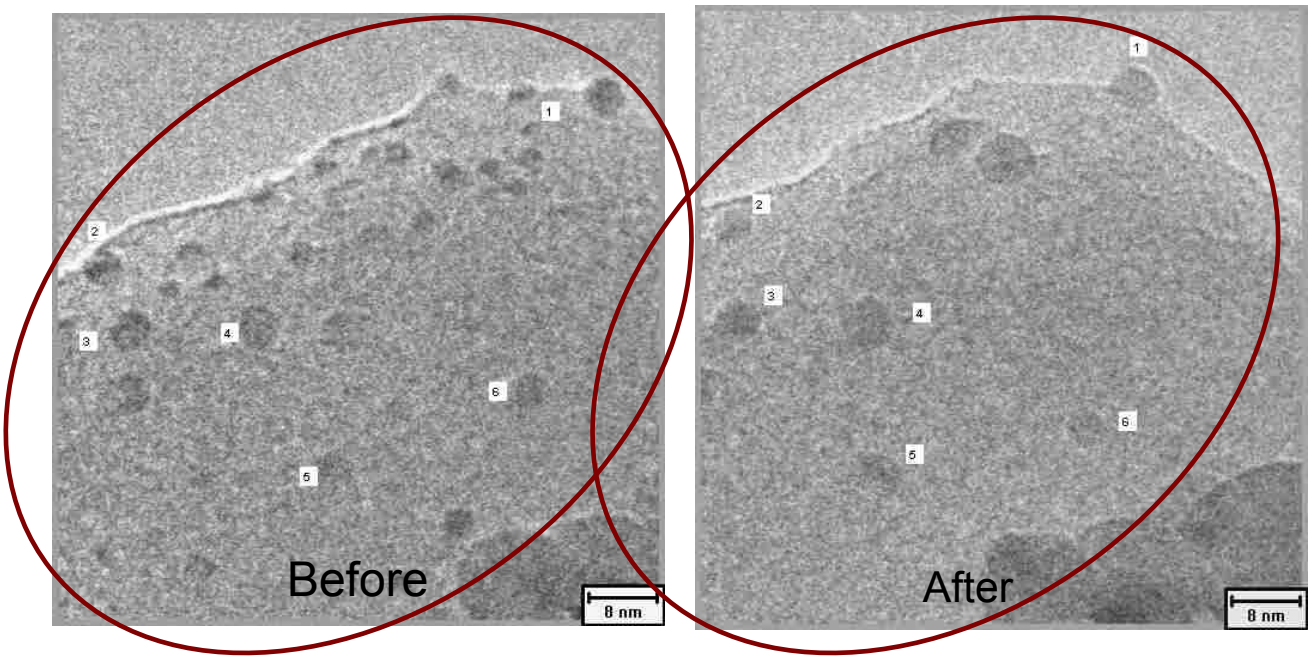

Figure 54 Images of Sample TEM2761 before and after exposure to 4mbar H_2:H_2O 1:1 at 650°C for 30minutes. The red circles indicate the area included in the Ni amount calculation. Before = $1.1x10^{-17}$g, and After = $1.2x10^{-17}$g.

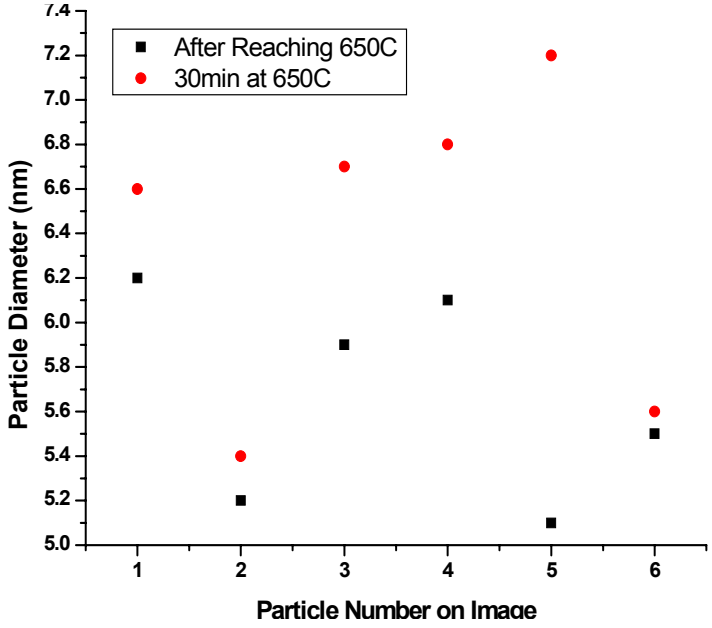

Figure 55 Particle diameter of stable particles on above images after sintering in 4mbar H_2:H_2O 1:1 at 650°C 30minutes. All particles that have remained in the same location have grown in size.

5.4 Results for 750°C experiments

As in the above 650C experiments, the same catalysts, holder, and mounting procedures were used, and all ramp rates were set to 50°C/min. The sample was reduced in 1.8mbar H_2 at 500°C for 30 minutes with the beam off. After the reduction process 1.8mbar H_2O was then added and the temperature was ramped to 750°C where images were obtained immediately after reaching temperature and after designated periods of time. The pressures of the gasses inside the system were lowered slightly from 2mbar each to 1.8mbar each. This lower pressure was used in order for the heating holder to achieve the temperature of 750°C, as heat was being taken away from the holder by the gases. The ratio of H_2:H_2O was still 1:1 as in all previous experiments, but total pressure was to be 3.6mbar instead of 4mbar.

The PSD for the 750°C experiments revealed the same shift in meant towards larger particles along with a skewed tail toward the right. An increase in broadness was also seen as the temperature and time increased as shown in the figure below. Similar results were reproduced under the same conditions on over 20 samples.

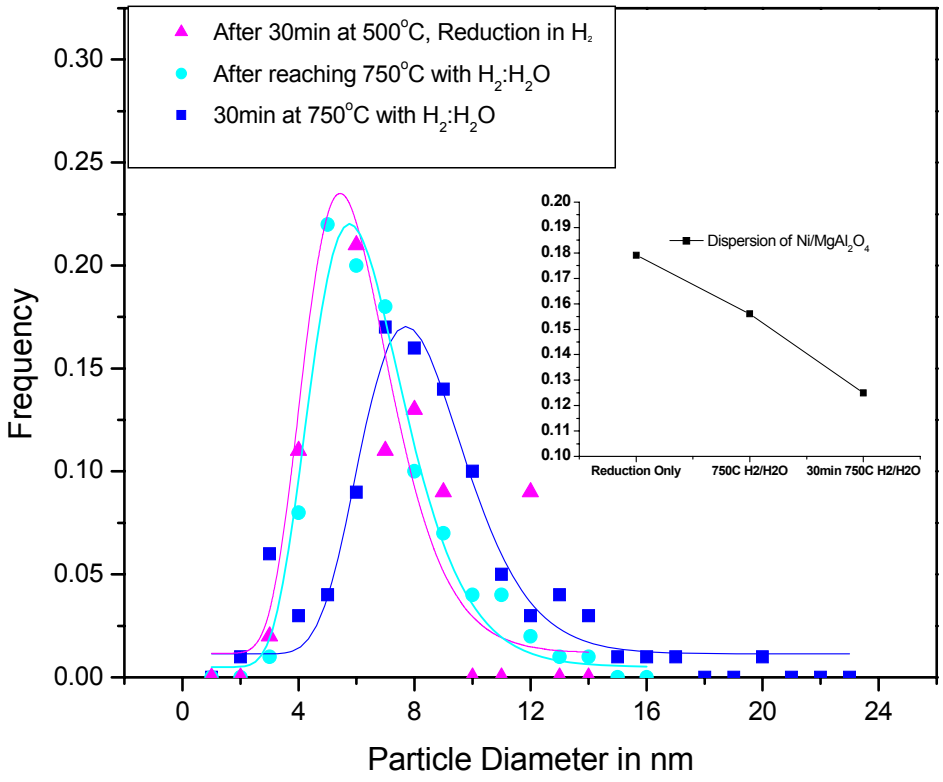

Figure 56 PSD of Sample TEM2788 12wt% Ni/$MgAl_2O_4$; Δ Reduced for 30min at 500°C in 1.8mbar H_2, ○ after reaching 750°C in 3.6mbar 1:1 H_2:H_2O, and □ after 30min at 750°C in 3.6mbar 1:1 H_2:H_2O. All distributions have been fitted with a Log-Normal function. The inset graph is a plot of the dispersion of the average Ni particle size.

Before and after images were also obtained for the samples at 750°C. These samples were not only aged for 30 minutes but up to 3 hours in some instances to determine longer ageing sintering behavior. The images revealed the same phenomena as

the previous experiments performed at 650°C. A number of particles (>5nm) were stable on the surface after an entire ageing period of 2 hrs, while other particles disappeared or moved to another location on the sample as shown in Figure 57. Particles were seen to grow, remain constant in size, or slightly decrease in size over time. Some modification of the images (cropping) were performed in order to maintain the same amount of area included in each image.

Repeated experiments revealed the same type sintering as shown in Figure 58. Assuming a spherical particle, mass was closely conserved, as it was calculated to be $1x10^{-17}$g on the before image and $0.7x10^{-17}$g on the after image, but the surface area had dropped significantly. This was seen repeatedly on many samples. The small decrease or increase in mass was usually seen due to our assumption in our calculation that all particles were spherical from start to end and also to the fact that mass could have been transferred outside the imaged area. An example of this can be calculated using the particle circled in Figure 58. By measuring the contact angle and radius of the particle, the volume can be calculated [6]. The volume of the circled particle was seen to increase by close to 50%, showing how a particles shape and presence in an image may affect the Ni mass calculation.

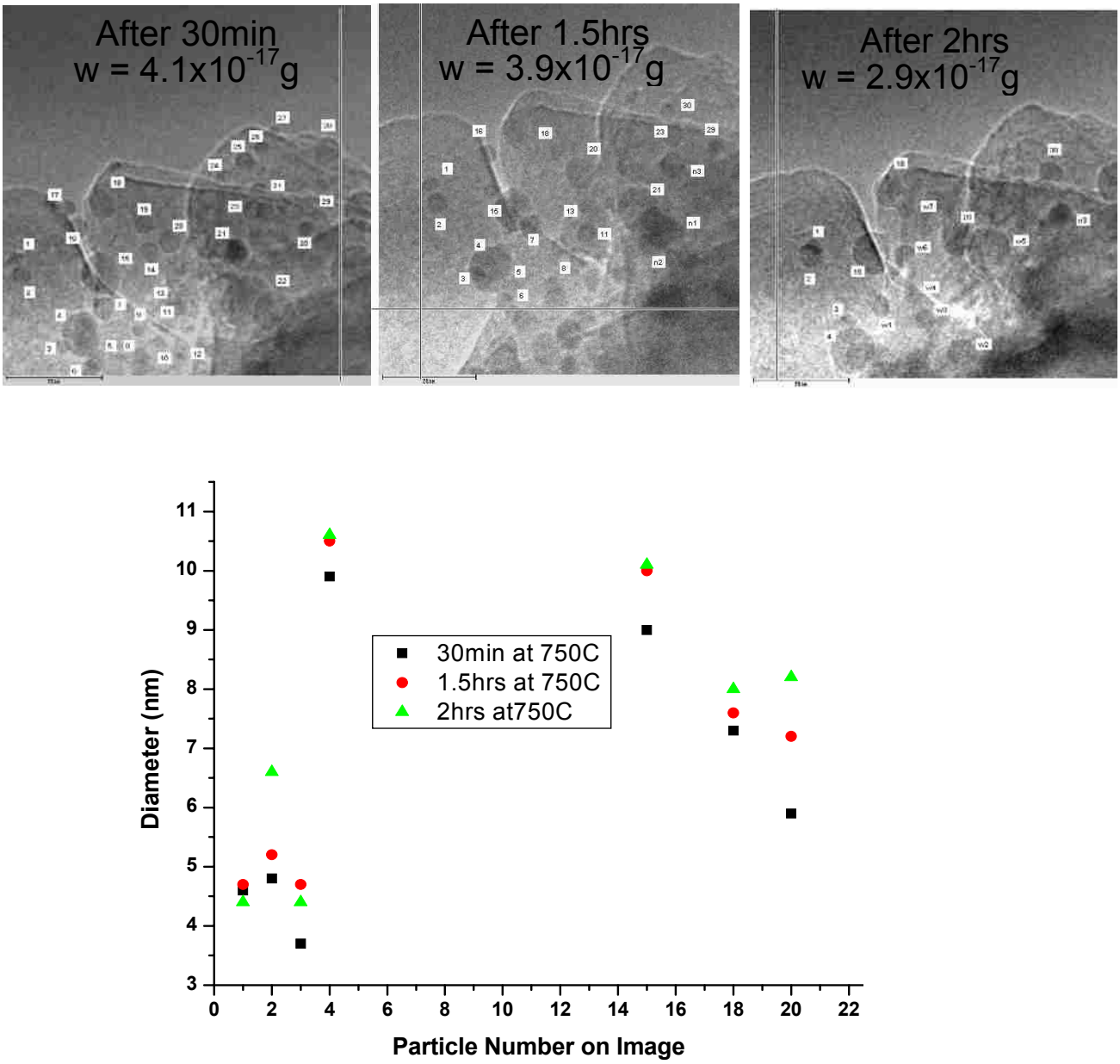

Figure 57 Top: Series of images of a specified area for Sample TEM2870 at 750°C with 3.6mbar 1:1 H_2:H_2O. w is the calculated amount (grams) of Ni catalyst in the same cropped area. Bottom: The corresponding graph shows the difference in size for individual particles corresponding to the above series of images.

The results at 750°C indicated that again no Ni was being lost to the vacuum and that a Log Normal PSD would be the result of heating under these conditions, indicative of coalescence as the dominant sintering mechanism. It was also seen that small particles (<3.5nm) were disappearing or rather sintering much more quickly than compared to experiments at 650°C, again providing evidence that smaller particles may be highly mobile[7] on the surface at these temperatures and sintering rather quickly. The dramatic loss in surface area, as calculated below, was also the result as recorded in previous experiments [14, 15].

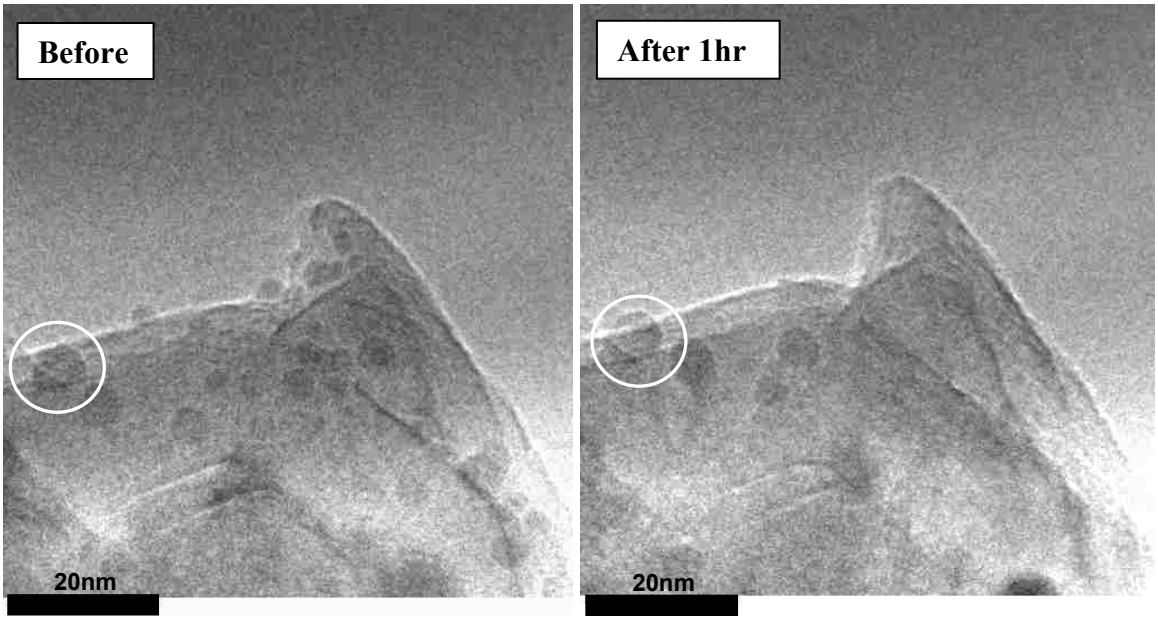

Figure 58 Typical before and after series of images performed in-situ, (1:1) H_2O:H_2 3.6mbar, for our Ni/$MgAl_2O_4$. The image to the right was taken 1 hour after the initial picture (left) was taken (after reaching 750°C). Note

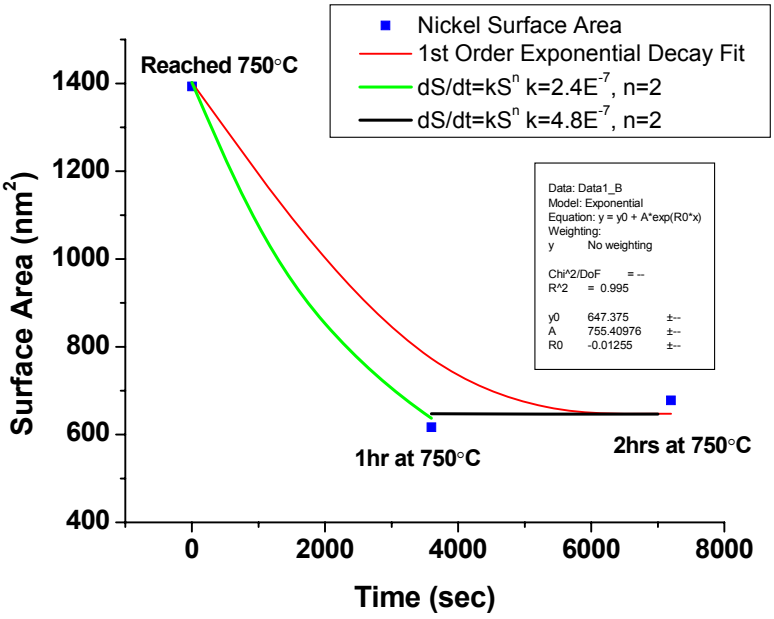

Figure 59 Calculated Ni surface area of in Figure 57 above with both an exponential decay fit and kinetic rate loss fit with a value of n=2.

The drop in surface area was fit to the power rate law, discussed in the previous chapter, in its integrated form (Eq 5.1) with a value of n=2. This is consistent with Ostwald Ripening being the dominant mechanism of sintering, but a problem arises as the PSD is consistent with coalescence behavior. Also note, the value of k was changed in order to calculate a better fit to the data. This change gives more evidence on how just measuring surface area loss may not be suitable enough to determine the exact sintering mechanism. The contradiction in data compared to theory resulted in the need for actual observation of the sintering mechanism in this system, only made possible by movies.

$$\left(\frac{D_o}{D}\right)^{n-1} = kD_o^{n-1}(n-1)t + 1 \qquad \textbf{(5.1)}$$

Molecular simulations of a collection of supported particles have also been performed to determine if the loss in surface area we are observing could be simulated. These simulations were performed in a Monte Carlo (MC) scheme based on a simple 3-D lattice gas model with *only ripening* as the possible sintering route, as that is what we are calculating by the power rate law.

At regular intervals of MC steps an enumeration of lattice sites is done to determine the nanoparticles composed of neighboring lattice sites occupied by the atomic species. The surface area of a nanoparticle is evaluated as the number of vacant lattice sites that have at least 3 sites occupied by atoms comprising these nanoparticles. Details on this analysis can be found in an earlier article on sintering of a dendritic nanosheet by Challa[64].

Before discussing the results of simulation it is relevant to point out that the starting distribution of particles was taken from a different metal/support/conditions system. Nevertheless, qualitative trends from these simulations should still be applicable to the $Ni/MgAl_2O_4$ sintering example. It can be seen that according to the simulation, a dramatic loss in surface occurs at the very beginning stages of the sintering process with the rate slowing over time. This matches not only our data, but previous work as well, giving evidence that ripening may be the mode of catalyst deactivation, but only direct observations can used to determine the exact mechanism.

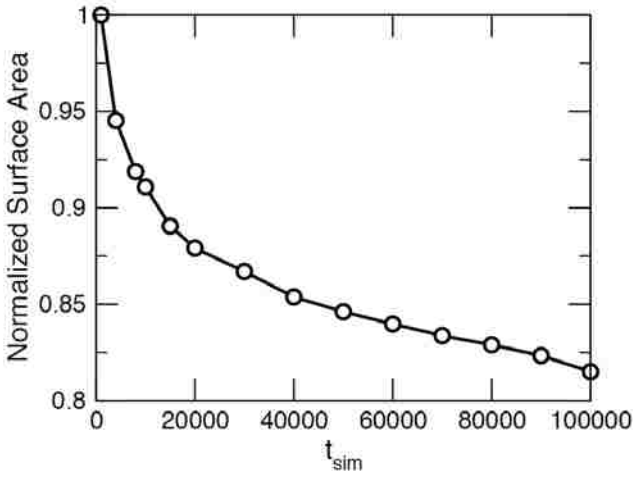

Figure 60 A Monte Carlo simulation revealing a sudden loss in particle surface area as seen in our experiments. The time (x-axis) is a MC simulated time.

5.5 Movies: Ripening with Coalescence (Seconds-Milliseconds)

The images and shape analysis above gave evidence that smaller particles were disappearing at a fast rate, but the method of sintering could not be determined from this data alone. Movies had to be made and image series had to be captured with shorter time intervals if any definite conclusion could be made. The next samples prepared and analyzed were put through the same conditions as the 750°C samples above. The only difference from the samples above and these samples were the amount of movies taken (up to 14 per sample) and shorter time intervals between series images (~8minutes compared to 30minutes). Before and after images were initially used to determine when exactly the sintering was taking place in that first half-hour after reaching 750°C. With the time period known, the movie recordings could be more accurately focused.

In Figure 61 below, the smaller particles are again seen to disappear at a fast rate while the larger particles remained either immobile or grew in size.

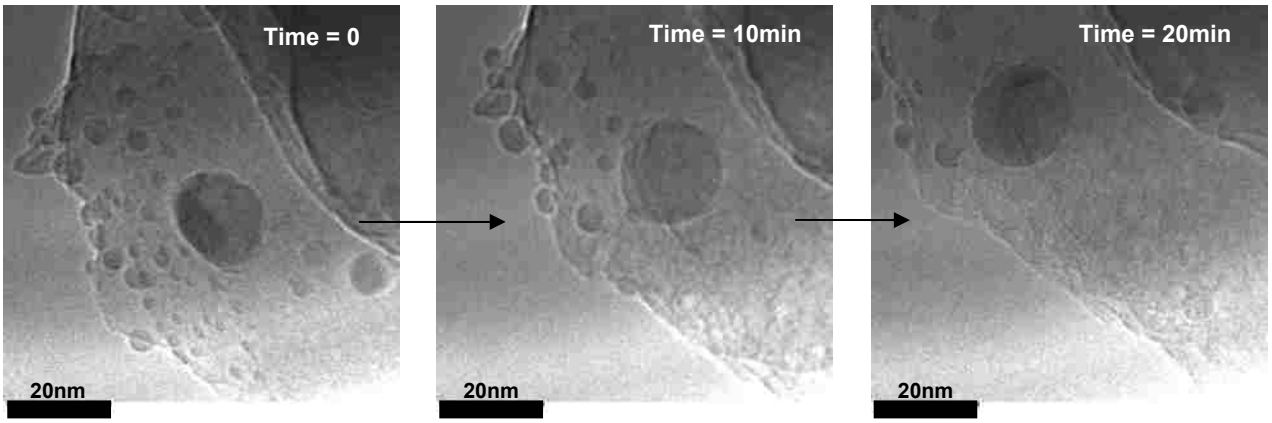

Figure 61 Series of images for sample TEM2894 in 3.6mbar 1:1 H_2:H_2O. The first image (left) was taken as soon as T=750°C was reached. The center image is 8 minutes after the first image, and the right image is taken 8 minutes after the center one. The smaller particles can be seen disappearing while the larger ones remain on the support.

This behavior was seen in multiple areas on the same sample in addition to other TEM samples where shorter time intervals were taken. According to the short time intervals as in the above figure small particles were sintering as soon as temperature was reached and up to 8-10 minutes after that. After this allotted time all the small particles (<3.5nm) disappeared and had sintered into larger ones. This meant any movies recorded would have to focus on the time period of when temperature had just been reached, and up to ten minutes after that to reveal conclusive evidence on which sintering mechanism was dominant.

5.5.1 Coalescence Movies

Movies initially were recorded 5 minutes after reaching 750°C due to the instability of the sample after being heated to such a high temperature. After 5 minutes of heating the coalescence of larger particles (>4nm) was observed and captured in the movie recordings. When the movies were examine frame by frame, it was calculated that the distance migrated by each of these larger particles was about its own diameter in length, seen before by Baker[25]. According to equation (eq. xp=root d) a particle with a radius of 3nm (d=6nm) should migrate a distance of around 110nm using a=.23, Do=300cm^2/sec, Q=159kJ/mole, and T=1023K[14]. In fact, no large migration distance was witnessed during the first 8 minutes after reaching temperature no matter the size of the particle. The migration and coalescence events would occur randomly to particles of a diameter of 4nm or larger on the flat support surfaces and on the edges. When the event did occur, the particle would only migrate a short distance and then remain immobile for quite some time.

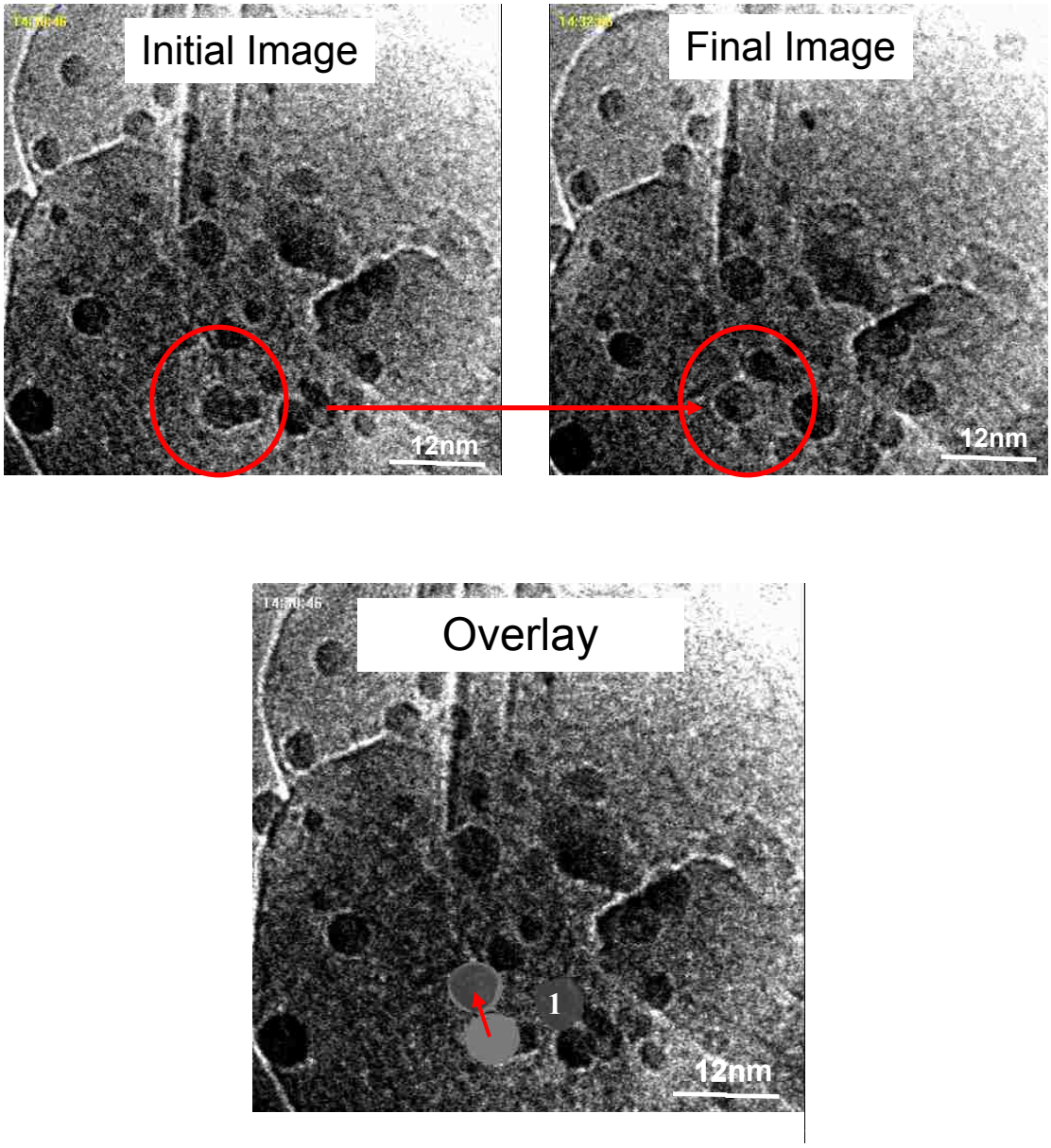

Figure 62 Frames of a recorded movie showing a coalescence event at 750°C in 3.6mbar H_2:H_2O. When the initial and final images are over-layed, it can be measured that the migrating particle moves about 6nm in length. A group of 3 particles were also seen to coalesce and make a new particle (1) on the surface.

5.5.2 Ripening Movies

The movie 6e for TEM 2890, shown below, revealed shocking evidence that particle ripening and particle coalescence were both occurring at the same time on the catalyst once temperature was obtained (750°C). Smaller particles (<3.5nm) would ripen quickly on the support while remaining immobile, and larger particles (>4nm) were seen to migrate and sometimes coalesce. A particle size distribution was made to capture the change in its distribution over the movie length. As shown below in Figure 64, the PSD begins to develop a larger tail towards smaller particles, which disappears and gives a more predictable log normal distribution.

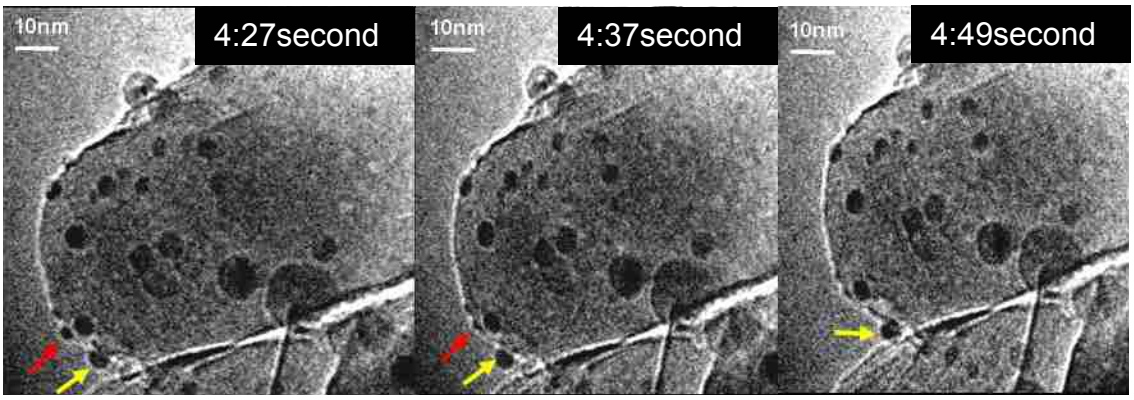

Figure 63 Movie stills for sample TEM2890 at 750°C with 3.6mbar 1:1 H_2:H_2O. The time interval between image 1 and 2 is .1sec and the time interval between image 2 and 3 is .1sec. The smaller particle (pointed out with red) can be seen ripening while a larger particle (pointed out with yellow) migrates and coalesces with another particle.

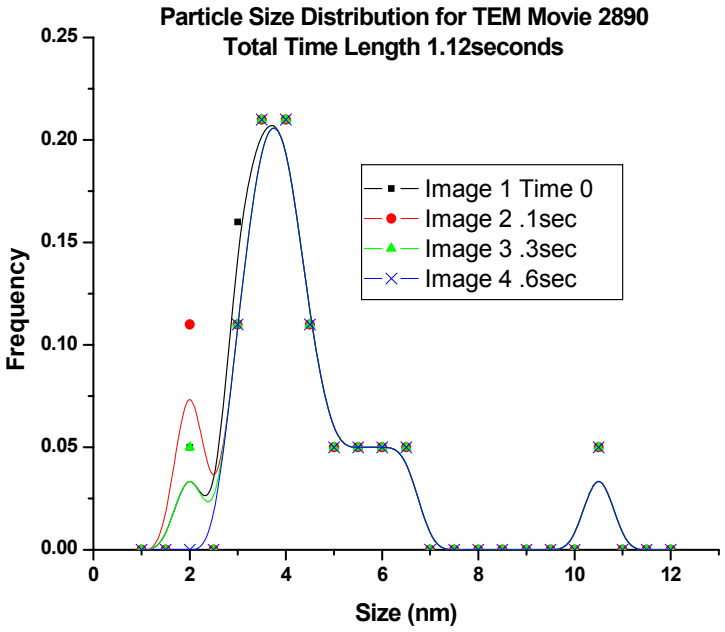

Figure 64 A progressive PSD for sample TEM2890 at 750°C with 3.6mbar 1:1 H_2:H_2O for Figure 62 over a time period of less than 1 second. □ is at Time =0, ○ = .1 seconds elapsed, Δ = .3 seconds elapsed, and x = .6 seconds elapsed. The PSD develops a tail towards small particles for a short time period, before becoming Log Normal in shape.

The ripening events can be seen much more clearly at a higher magnification as seen in Figure 65. The smaller Ni particle ripens away quickly to surrounding larger particles, and is not actually highly mobile on the surface. It was also calculated that the ripening events occur suddenly and rapidly, often with the particle disappearing in 200 milliseconds. Quick and sudden ripening behavior was not only captured in a particular area, but in multiple areas on multiple samples as graphed in Figure 66 below. In figure 66 the particles were measured to reach a size of about ~1.5nm before they suddenly disappeared by the time the next image was captured, revealing a large exponential decay once the particle reaches a determined size.

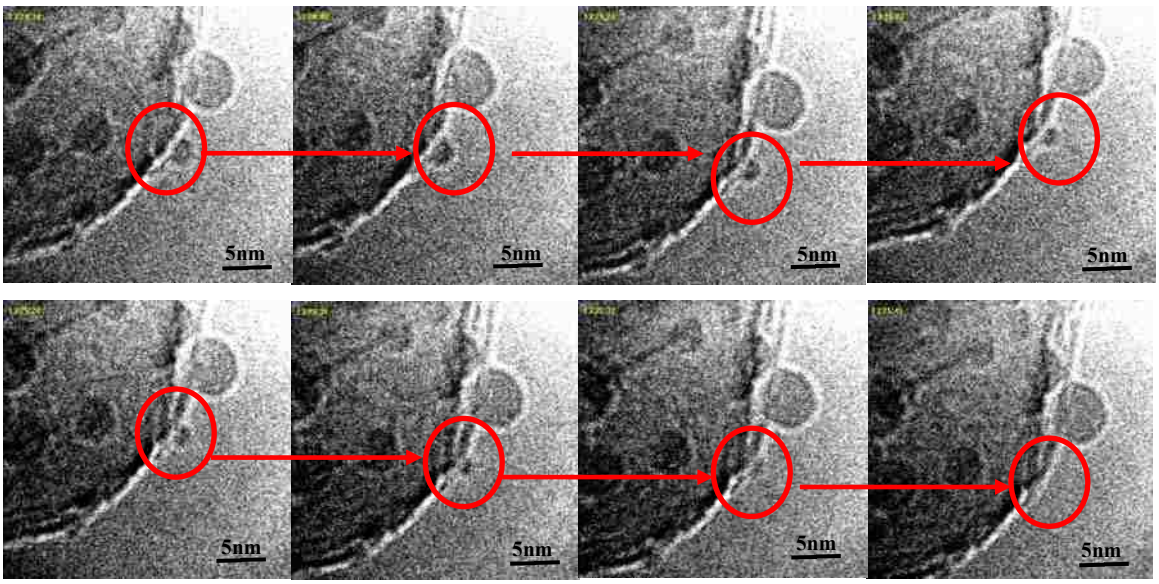

Figure 65 Movie stills taken from movie 6e of experiment TEM2902 at 750°C with 3.6mbar 1:1 H_2:H_2O. It was seen that the particle, roughly ~2.5nm, ripened away in a time period of less than 1 second.

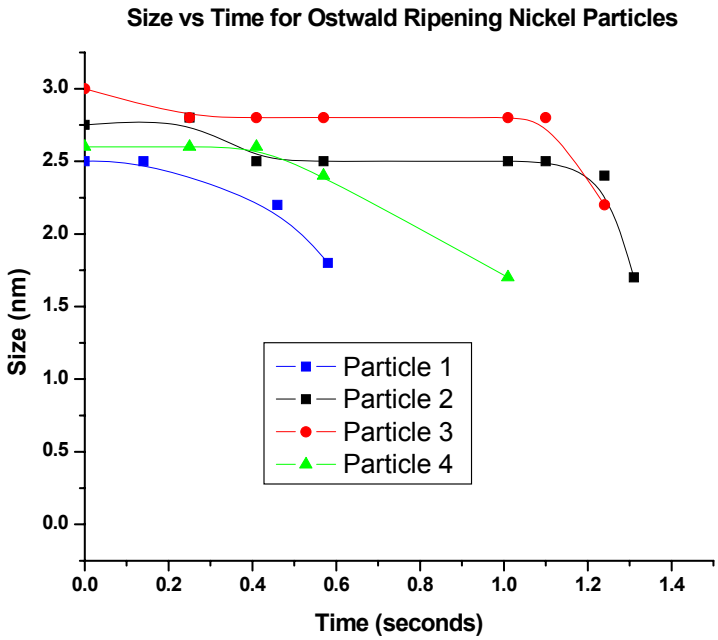

Figure 66 Size vs. Time for Ni particles ripening in reproduced experiments with the same 12wt%Ni/$MgAl_2O_4$ catalyst powder under 3.6mbar H_2O:H_2 1:1 at 750°C. Particle 1 is from Figure 65 above.

The sudden drastic decay in particle size was compared to and closely matched Monte Carlo simulations with ripening restraints seen below in Figure 67. In order to confirm that indeed ripening is occurring as opposed to particle migration and coalescence, the sizes of six particles in close proximity were tracked in the simulation. The size evolution of these particles clearly shows that small particles are diminishing and large particles are growing. Two things are notable about the small particles being tracked. One can observe an almost uniform rate of decrease in size initially and this rate accelerates when the particles become smaller than a critical size. This is a consequence of the enhancement of vapor pressure due to small radius of curvature (Kelvin relation) of these particles. The growth of the larger particles is steady as might be associated with incorporation of adatoms into these particles. Also, the growth plot does not display any jumps that might be associated with coalescence events. We also do not see any jumps in

size of any Ni particles when the ripening event occurs. Thus, it can be concluded that ripening is the mode of sintering in these simulations and in experiment for small particles. Additional analysis, such as the trajectories of centers-of-mass of these same six particles (not shown) over the course of the simulation, indicates that the particles are localized, with displacements much less than their size or inter-particle distances. This further corroborates the ripening mode of sintering for the smaller particles (<3.5nm).

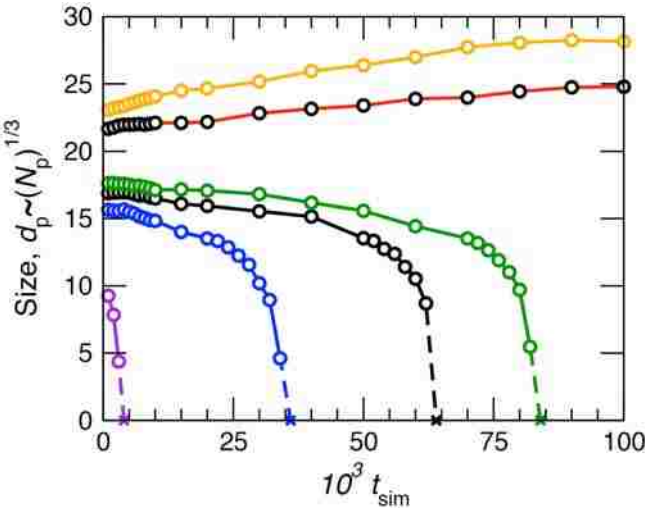

Figure 67 Monte Carlo (MC) simulation of larger particles growing at the expense of the smaller particles. Note MC Time is simulated time. Provided by S.R. Challa.

With a higher magnification used, the role of beam affects came into question. Experiments were made with varying beam intensities to conclude that the beam was not causing the ripening behavior captured. The differences from image to image were small compared to those from experiments, which were intentionally varied to determine beam affects. Experiment TEM2902 used low beam intensity throughout the experiment, while experiment TEM2900 used a variation in beam intensities, and experiment TEM2894 maintained a high intensity throughout the whole experiment. This can be seen in the

average beam intensities seen in Table 3 below. The intensity did vary slightly from image to image (up to 10%), but it still did not effect the sintering behavior.

Table 3 Beam Intensities for three different experiments put under 3.6mbar 1:1 H2:H2O at 750°C. TEM2902 has the lowest while TEM2894 has the highest. All three experiments saw coalescence and ripening behavior.

Average Beam Intensities for Series at 750°C in e/nm^2				
Magnification	**110kx**	**150kx**	**200kx**	**270kx**
TEM2894	22608.2	-	-	-
TEM2900	16201.9	-	32725.9	73627.5
TEM2902	13999.1	9323.7	-	38363.5
2902/2900	0.8640411	-	-	0.521049

The evidence of a combination of ripening and coalescence was seen on multiple samples under the same conditions. The same behavior was also seen with varying beam intensities. The absence of this sintering phenomenon with varying beam intensities also gives evidence that the sintering is not influenced by the beam. Movies were taken of particles ripening and disappearing from a straight on view (top) in addition to a profile view, to confirm the particles are not just moving into the support. Thinner regions of the material that have been imaged also confirm that the particles are not "hiding" behind the support.

Although ripening was seen, it was not determined how the particles were going to ripen on the surface. Recorded in Figure 65, the particle ripened in a fashion that maintained its shape, shrinking from all directions. Additional movies obtained reveal

variances in behavior, where the particle seemed to ripen from the "top" of the particle while maintaining the length of its particle-support interface (an illustration is shown below). In Figure 69, a series of images taken from a movie illustrate how the ripening process of a particle may vary, as the third ripening event shows a particle maintaining its particle-support interface length throughout the ripening process. Further analysis was needed to determine how the shape of the particles may affect the ripening and coalescence process.

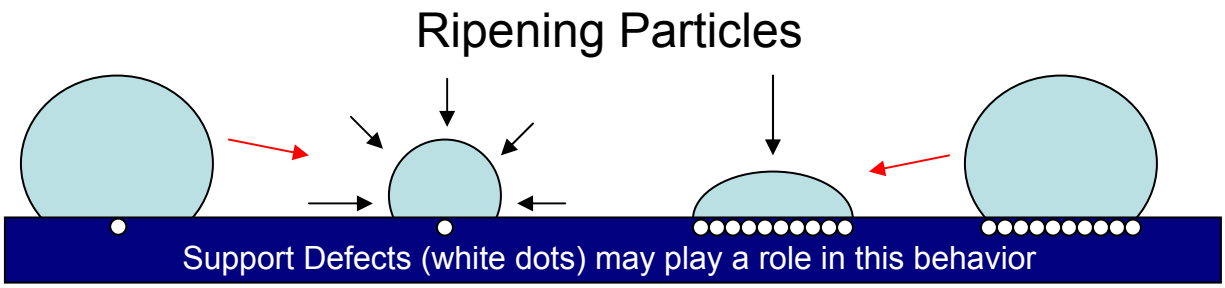

Figure 68 The particle on the left ripens from all directions (shrinks maintaining its aspect ratio), while the particle on the right maintains the same particle-support interface length, and ripens from the top only.

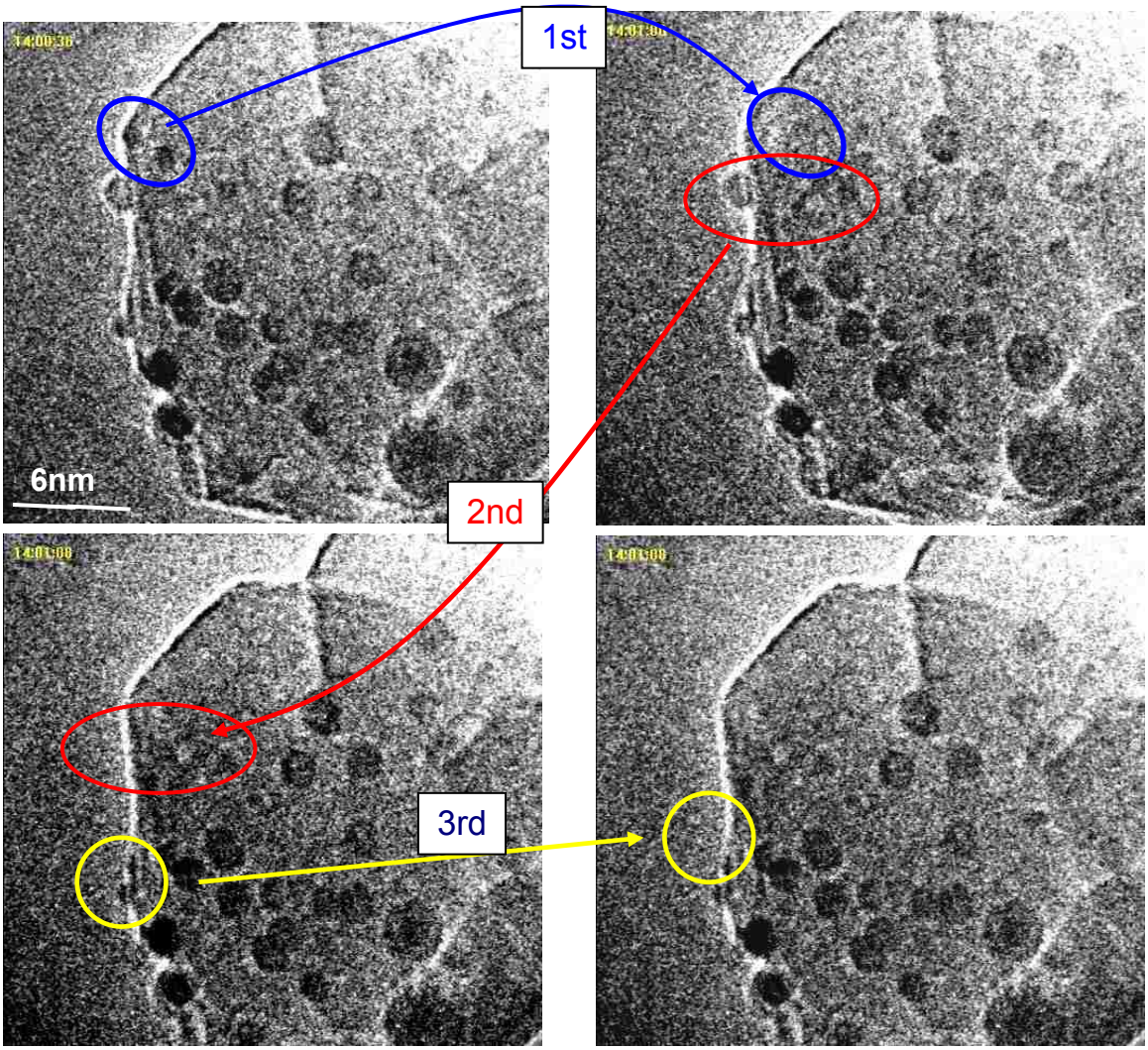

Figure 69 Multiple ripening events (3) of 5 particles occurring on Ni/$MgAl_2O_4$. The entire movie takes place in less than 2 seconds. Of the particles on the profile view, a particles ripens (2nd event) from all directions while the other from top to bottom (3rd event).

5.6 Shape Analysis and Work of Adhesion

The shapes of the particles were studied under the various stages of heating in order to determine if particle mobility, stability, and ripening were not only dependent on size but also of the work of adhesion to the support. Images were taken at a higher magnification than for a PSD and only particles with a profile view "on top" of the support were included in the calculations. The images themselves were collected at various times of the experiment, to determine how the rise in temperature or introduction of water may affect this behavior.

Ni particles were seen to be more hemispherical in shape after the reduction cycle at 500°C in 1.8mbar H_2 and also after the introduction of 1.8mbar H_2O. The particles became more spherical after the sample was ramped to 750°C under 3.6mbar 1:1 H_2:H_2O. The work of adhesion of the particles to the support was calculated in order to determine if the adhesion of the particles to the support would decrease as the shape changed. To do this we used the Dupre` equation below

$$W_{adh} = (1 - \frac{\gamma^*}{\gamma_0}) \cdot \gamma_0 = (1 - \frac{b}{a}) \cdot \gamma_{(111)} \qquad \textbf{(5.2)}$$

with γ_{111} =2.01 J/m^2 as the Ni (111) surface energy. The ratio of the effective interface energy, γ^*, and the metal free surface energy, γ_o, can be substituted using the geometry of the particle on the support[30, 65] as shown below.

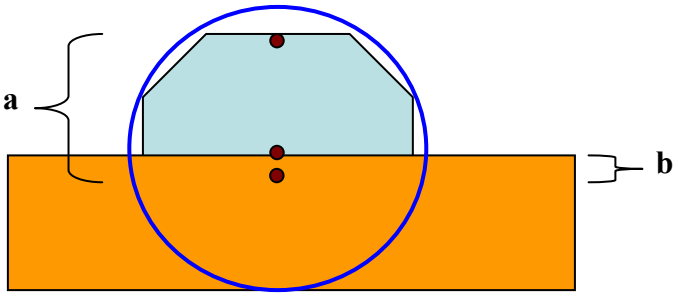

Figure 70 Schematic of how measurement was performed for our Ni particles to determine the work of adhesion using the Wulff construction.

Essentially, the radius of the circle is defined as *a*, with the center of the particle to the support defined as *b*. The Ni (111) face was used as it is the overall majority of faces seen in this experiment as well as the lowest energy in this case. As the temperature is increased from 500°C to 750°C under 3.6mbar H_2:H_2O, it was measured that the work of adhesion overall decreases with the increasing size of the particle and as more spherical in shape the particles became.

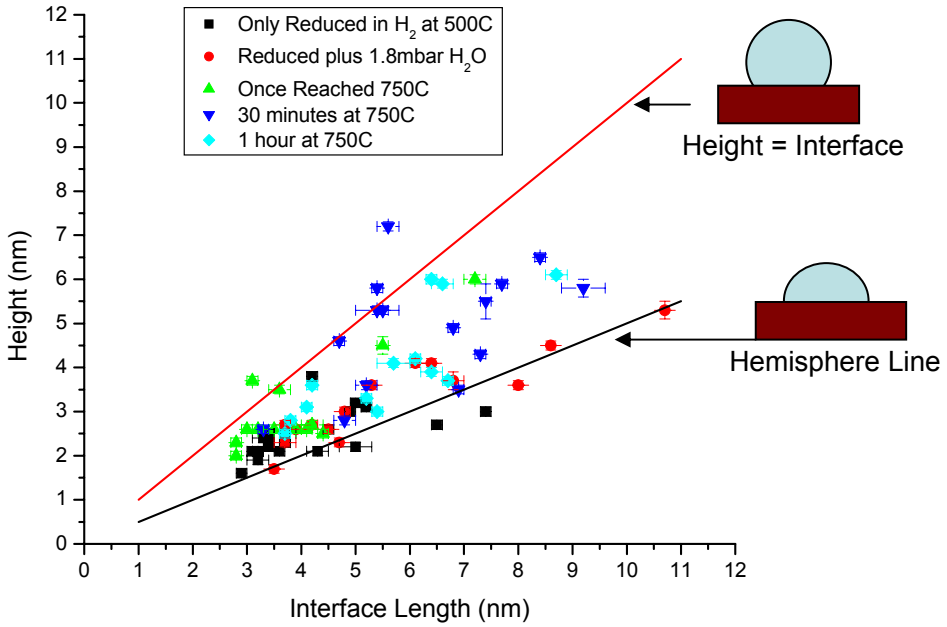

Figure 71 Height vs. Interface Length for Nickel particles on 12wt% Ni/$MgAl_2O_4$ TEM2794 exposed to various conditions.

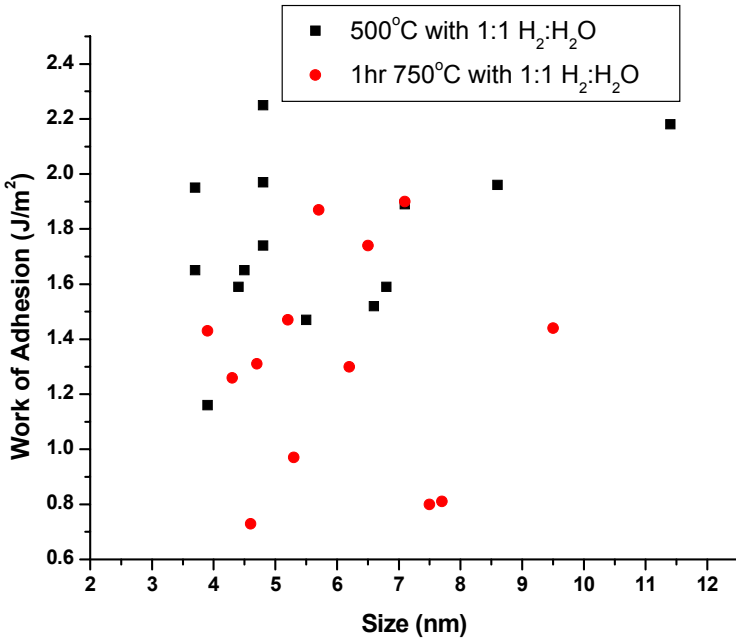

Figure 72 The calculated work of adhesion of Ni sample TEM2794 after being reduced for 30 minutes in 1.8mbar H_2 and the introduction of 1.8mbar H_2O, and after ageing for 1 hour at 750°C under those atmospheric conditions.

An additional experiment was performed for shape analysis after 3hrs of sintering to determine if the data scattered from over the 30 minute period could be furthered refined, and to determine if longer ageing periods would result in a more spherical shape. After 3hrs of ageing, a majority of the particles (all of varying sizes) had evolved into shape where the particle interface length was equal to the particle height (just short of being a complete sphere). Additional calculations were made on the contact angle of these particles to show that majority of them had an angle greater than 90°.

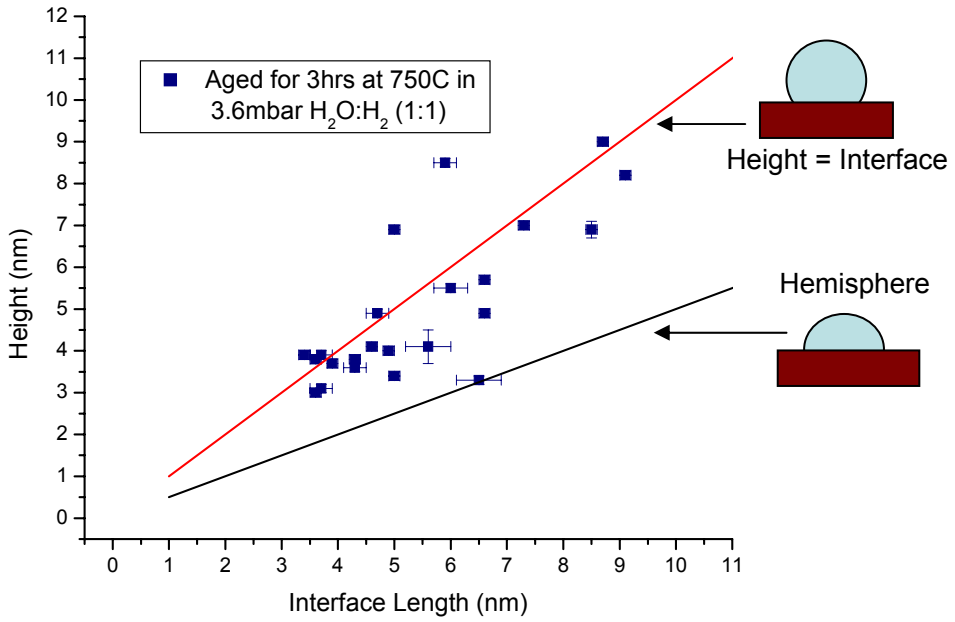

Figure 73 Height vs. Interface Length for Ni particles on Sample TEM2834 heated for 3hrs under 1:1 3.6mbar H_2:H_2O. The particles become more spherical in shape over time.

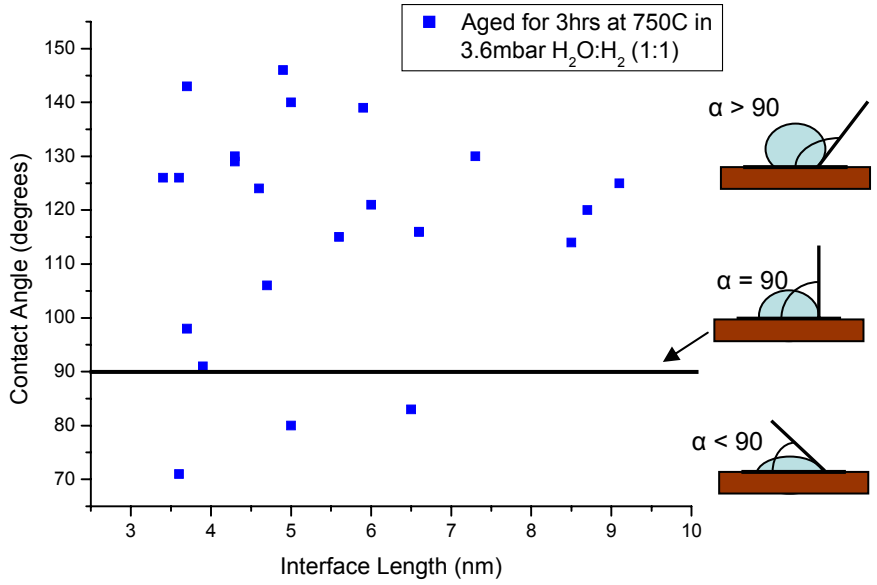

Figure 74 Contact Angle vs. Interface Length for Ni particles on Sample TEM2834. A majority of the particles lie above the 90° line, indicating a more spherical shape.

Previous work by Hansen[66] had shown a Cu particle changing morphology after the introduction of H_2O into the microscope, specifically more spherical. After the

H_2O was removed, the Cu particle returned back to its crystalline shape. We also performed this type of experiment to determine if the morphology of the particles was heavily dependent on H_2O being present. Shape analysis had been performed on a sample aged at 750°C for 1 hour under 3.6mbar 1:1 H_2:H_2O, which was left in vacuum overnight, and then re-reduced the next day in 1.8mbar H_2 at 500°C to record if the particles would return to their more adhering hemispherical morphology. The analysis in Figure 75 revealed that the particles maintained their shape (similar to additional experiments carried out for 1hr) even after this cool down and re-reduction process.

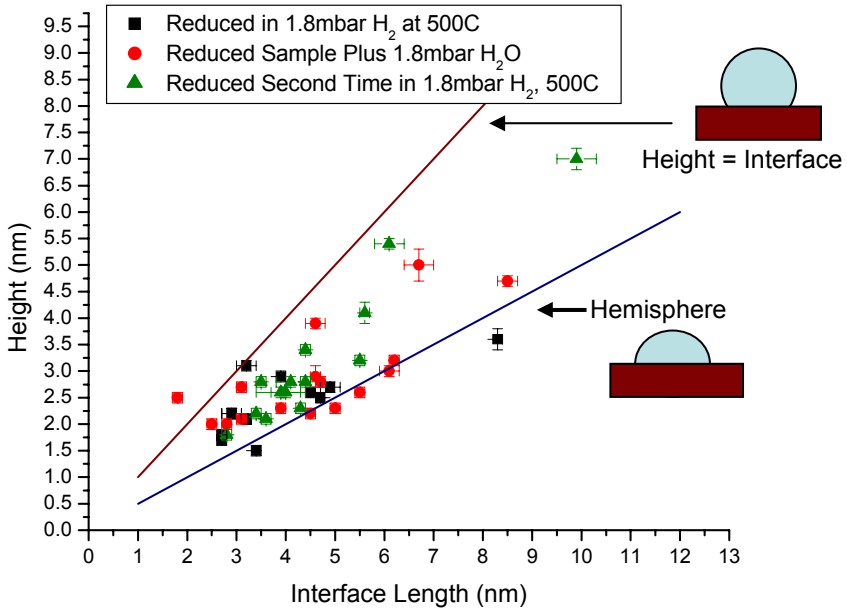

Figure 75 Height vs. Interface Length for Ni particles on Sample TEM2819 to test for particle morphology after reheating. The second reduction was performed 24hrs later, after the sample cooled under high vacuum conditions.

5.7 Discussion

It was calculated that the PSD for our Ni catalyst experiments were log normal in shape and developed a skewed tail towards larger particles over longer ageing times. A dramatic loss in surface area was seen to occur in the first 10 minutes after a temperature of 750°C under the H_2 and H_2O environment. Evidence from imaging an area over time indicated that the Ni was remaining on the support and not being lost to vacuum, and only sintering was occurring. The ripening of small particles was captured by movie recordings time and again, no matter where on the support the small particles were accumulated. It was also measured that ripening occurred with both low and high beam intensity at different magnifications on numerous samples. The variations in beam intensity gave the conclusion that the ripening behavior was not the result of the beam bombarding the sample, but rather only a result of the high temperature and gaseous environment. The coalescing of larger particles was also observed on the same samples, with the migration length measuring to be equal to the particle diameter. The migration was random in nature and only occurred to particles larger than ~4nm. With a combination of the two processes occurring it is possible to produce a log normal PSD as shown below.

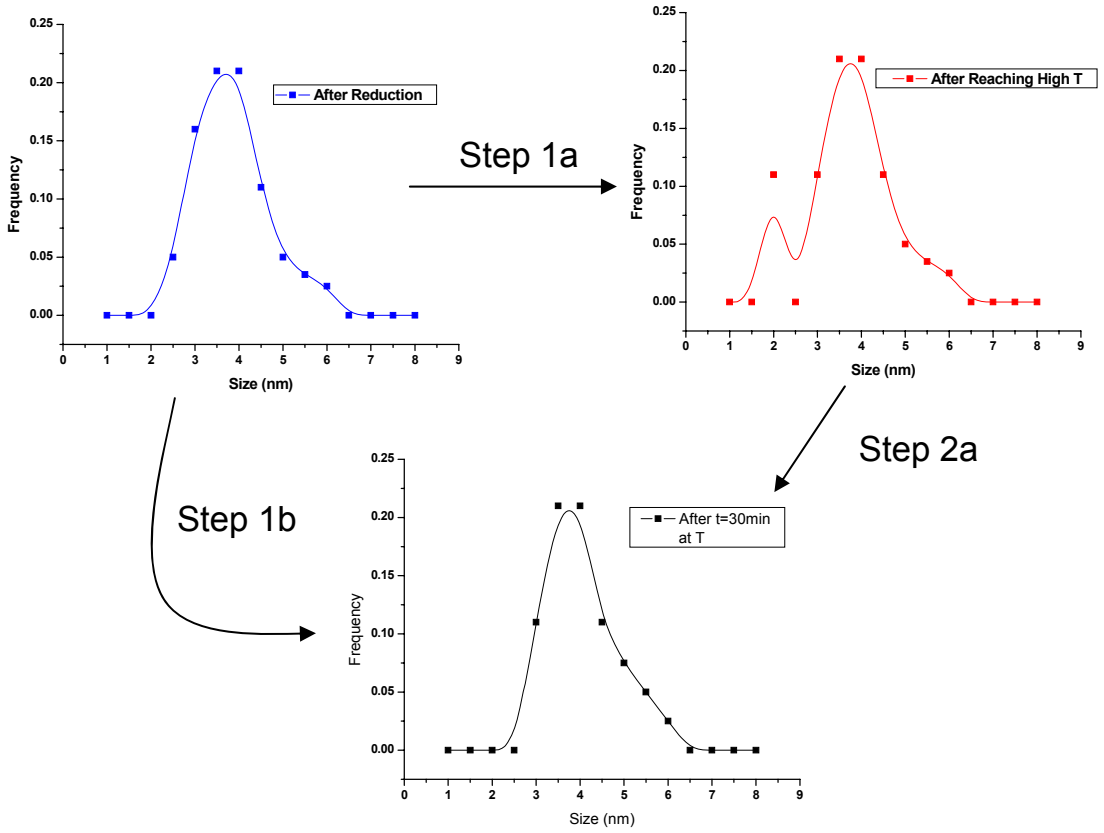

Figure 76 A schematic of an ageing PSD resulting in a log normal distribution. By focusing on experiments as soon as temperature was reached, Steps 1a and 2a were observed in-situ. Without such experiments, only Step 1b could be recorded.

With small particle sintering occurring so quickly, a PSD would not be affected over long times, hence only a log normal would be produced as the LSW (ripening) model would only be observed for a short period, with the actual event occurring in less than a second. This is evidence why longer ageing times and after long reduction periods only log normal distributions were observed, with the conclusion that only coalescence was occurring. The fast ripening of the small particles can be explained by the increase in chemical potential with decrease in size. Once those small Ni particles reach a certain size, the loss becomes exponential and those particles ripen at an extremely fast rate.

Since our sample and many catalyst samples are saturated with small particles (high dispersion) at the beginning stages of experiment, and these particles ripen and sinter at a fast rate, it would explain the sudden loss and dramatic decrease in surface area as soon as the catalyst is exposed to harsh conditions.

Small particle ripening behavior was modeled using Monte Carlo Simulations, showing that the disappearance would be extremely fast as soon as the particle reaches a certain size. It also revealed that the increase in size on larger particles could not clearly be seen if smaller particles ripen to a much larger particle, similar to our experimental results.

It was also seen that the small particles could ripen in two different ways either as a whole, maintaining the same aspect ratio, or from the top to bottom, maintaining its particle-support interaction length. This particle support interaction is evidence that the particle support interface (a defect site) is of great importance and may give reason to why smaller particles are almost immobile on the support when compared to larger particles. The support interaction may be stronger and more significant on smaller particles and may "hold" them in place on the support restricting particle migration.

According to the shape analysis, the shape of all particles tends to become more spherical in shape the longer the sample is under experimental conditions. The high temperature and introduction of water seem to be the elements contributing to this result, either by limiting the number of sites the atoms can adhere too, or by making an OH-metal species that is more mobile causing instability. With a limited number of sites to adhere too, the particles may become more spherical over long term ageing as the entire defect site is already occupied by other atoms or by other attached groups (OH, O). Once

the particle becomes large enough and spherical in shape (decreased adhesion), it is capable of detaching itself from that support; hence the particle simply rolls over once (its particle diameter). With a large enough density of particles, small migration steps would result in particle-particle interaction (coalescence) resulting in a skewed tail in a PSD towards larger particles.

Support defects determine how the particle is ripening on the surface, while the rate is determined by the size of the particle. Future models for accurately describing the sintering mechanism will have to include particle density, site density, particle wetting, and particle-support interaction in order to confirm and predict how the particles are sintering and how they will behave over time. Additional experiments can also be made with additional gasses, a higher temperature, and the use of new TEM in-situ cells capable of reaching pressures of up to 760 Torr.

Chapter 6

6 Conclusions and Future Work

The sintering and stability of three different catalysts were studied in order to gain mechanistic insight on what can cause instability in a catalyst that can lead to sintering. It was measured on flat model samples that direct evaporation of Palladium nanoparticles at 900°C could not account for the metal lost. Particle interactions with the support enhance the adatom concentration and hence increase the amount of evaporated metal. The increase in evaporation reveals the importance of particle-support interactions, and stresses the study of the support for each desired reaction. The study also provided evidence that the atom transfer and diffusion process in the ripening of particles is the dominant form of particle growth while vapor phase transport may only play a small role. Powdered 7wt%Pd/Al_2O_3 sintering studies at 900°C revealed an increase in particle growth when water vapor was introduced, leading to the belief that support structure change and hydroxyl groups could have formed on the Pd particles, making the atoms more mobile. The samples aged in vacuum gave evidence that support changes can influence particle stability and size with no other type of chemical reactions (gas or water).

The affect of Carbon structure on the stability of PtRe nanoparticles and adatoms were studied and lead to the conclusion that the more roughened and finely broken up structure of the Norit Carbon would provide numerous adsorption sites for the metal to adsorb to. The Vulcan Carbon was seen to be more graphitic, with less adsorption sites,

giving a heterogeneous distribution of particles with little dispersed atomic species. The degree of this can be seen after the samples were put through reaction conditions.

The sites on Norit appeared to form at the ends of the nanosized Carbon structures (edges), with particles forming where numerous sites were in close proximity to each other. With an increase in the amount of sites the tendency for the particles to sinter was less, and a higher dispersion was achieved. From EDS analysis it was seen that the dispersed species was entirely made of Re, with Pt having a tendency to form particles with a small amount of Re species, opposite of known simulations. After heating experiments to both 700°C and 900°C on Norit, it was measured that Re was agglomerating with the already present Pt particles, making intermetallic particles. The support was seen to become more graphitic over the temperature treatments, leading to the belief that the more graphitic carbon support and a more volatile Re species have lead to sintered particles bimetallic in composition. Current work in DFT has shown that a 50:50 mixture of Re and Pt can be stable even though the known stable crystalline structure is FCC for Pt and HCP for Re. This work is currently being written up and further DFT with XRD studies are being performed for this system.

In-Situ heating experiments on a ~14wt% Ni/$MgAl_2O_4$ catalyst revealed a large loss in surface area at the early stages of heating with the presence of H_2 and H_2O. Movie and image analysis revealed that the Ni was not evaporating off the support but simply sintering at a fast rate. Further work and movie capture at the early stages of heating revealed the Ostwald Ripening of smaller particles (<3.5nm) which occurred in matter of seconds, consistent with Monte Carlo Simulations. The movies also showed larger Ni particles (>4nm) moving and coalescing on the support. The observations were

contrary to the previous literature and theory, which assumed the opposite behavior based on calculation. The ripening of small particles and coalescence of larger particles still led to a log normal type distribution over time, again confirming that sintering mechanisms can not be clearly identified with only particle size distributions.

Although the studies above provided fundamental insight of the stability and sintering behavior of nanoparticles, the work could be further explored with new projects to answer additional questions and to bring further conclusions to the above data. Variations in the flat model support species could be performed in order to determine the effect the support has on the stability of the nanoparticles and also the diffusion and sintering processes. DFT modeling can be used to determine the difference in energies between the metal-metal bond and the metal-support bond, to further clarify why various supports affect the metal differently. The PtRe and Pt-M (metal) samples on Carbon can be put through a CO or Water Gas Shift reaction study in order to see the effect the Carbon structure has for these reactions. Different carbon supports could also be used and/or one carbon support could be used with and without chemical treatments in order to produce functional groups on the surface. The addition of these groups may affect the stability and dispersion of the metal catalyst. DFT could also be performed to determine why the edge sites adsorb the atomic species and keep them stable as compared to a support without edge sites. In-Situ studies could be performed at atmospheric pressure (due to further advancements in technology) in order to determine if pressure affects the stability. Simulation can also be performed of the possible defect sites that may determine particle stability, mobility, and ripening behavior.

Appendix A: Chapter 3

Appendix A.1 Pd on Al_2O_3-Flat Model Samples

Three flat model supports were heated and the Pd particles were measured to grow. The three different supports used, Al_2O_3, ZrO_2, and SiO_2 are shown in the figures below. The largest growth was seen on Al_2O_3, with the average size after ageing being 69nm. Vacuum experiments were also performed on the Pd/ZrO2 sample under the same conditions as the Al_2O_3 sample see in the figure below.

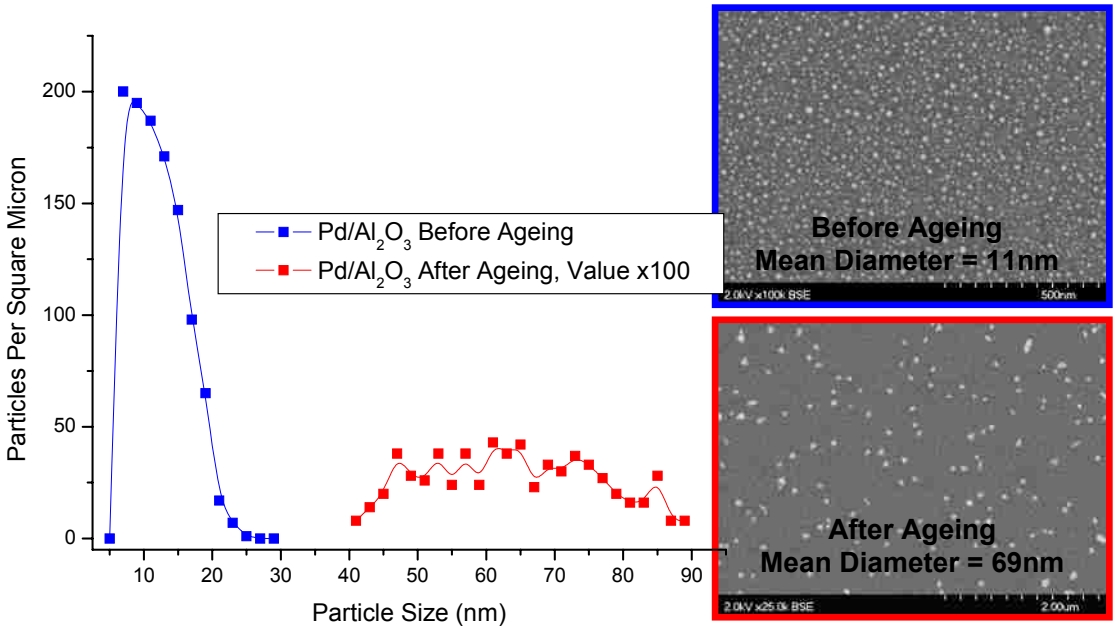

Figure 77 Pd/Al_2O_3 flat model heating results. Sample was heated at 900°C for 12hrs under Nitrogen gas environment. The mean diameter grows from 11nm to 69nm

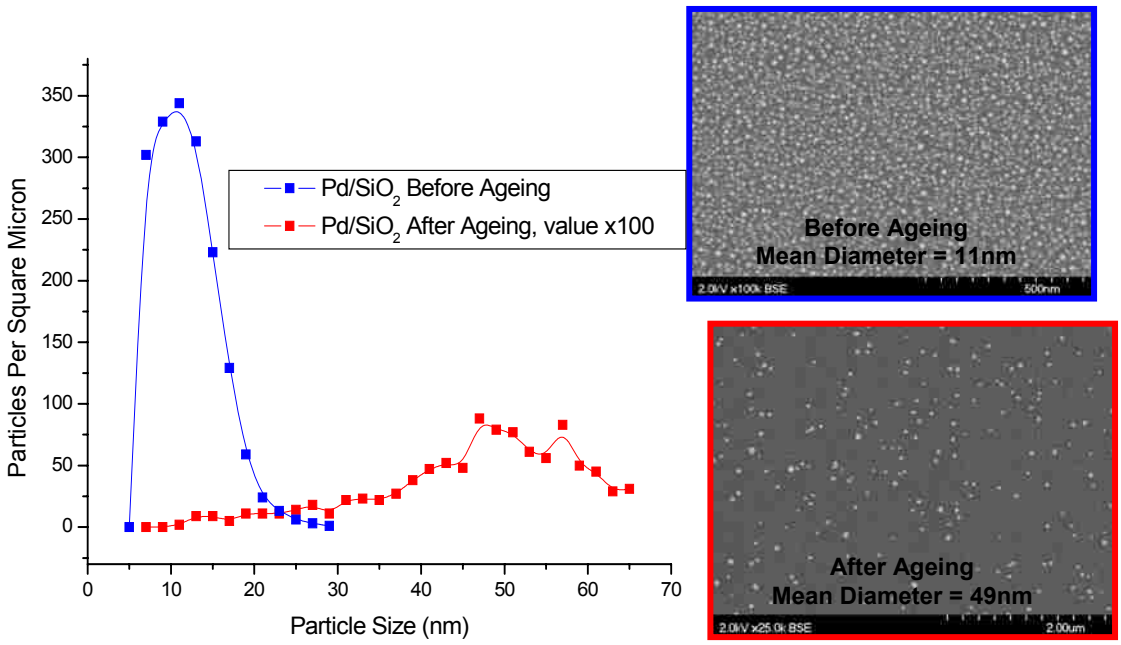

Figure 78 Pd/SiO_2 flat model heating results. Sample was heated at 900°C for 12hrs under Nitrogen gas environment. The mean diameter grows to 49nm

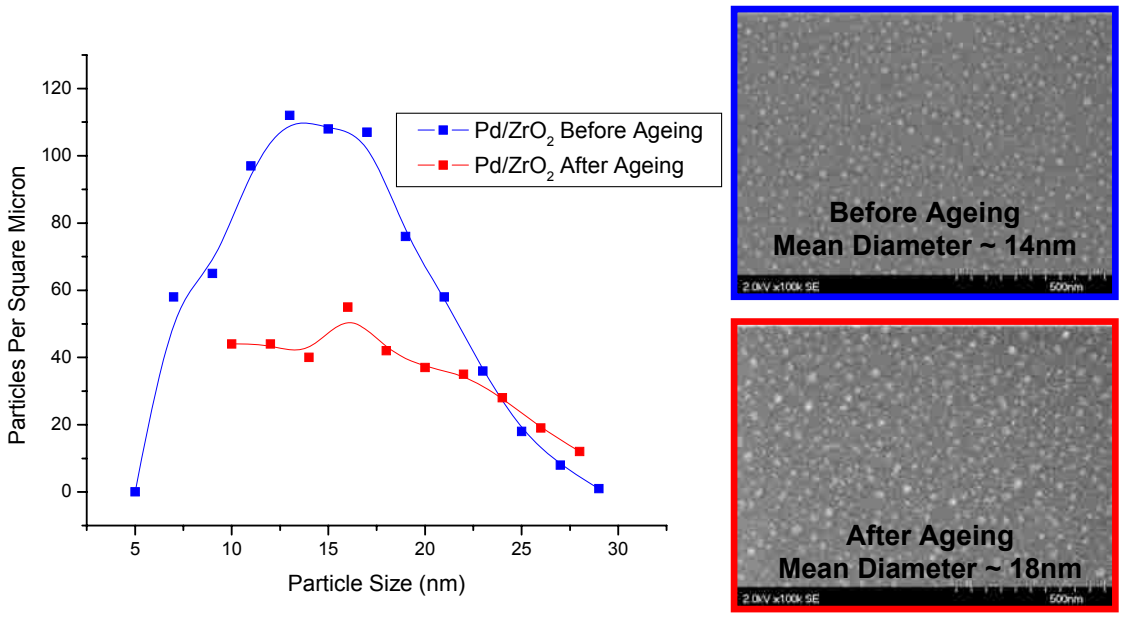

Figure 79 Pd/ZrO_2 flat model heating results. Sample was heated at 900°C for 12hrs under Nitrogen gas environment. The mean diameter grows to 18nm

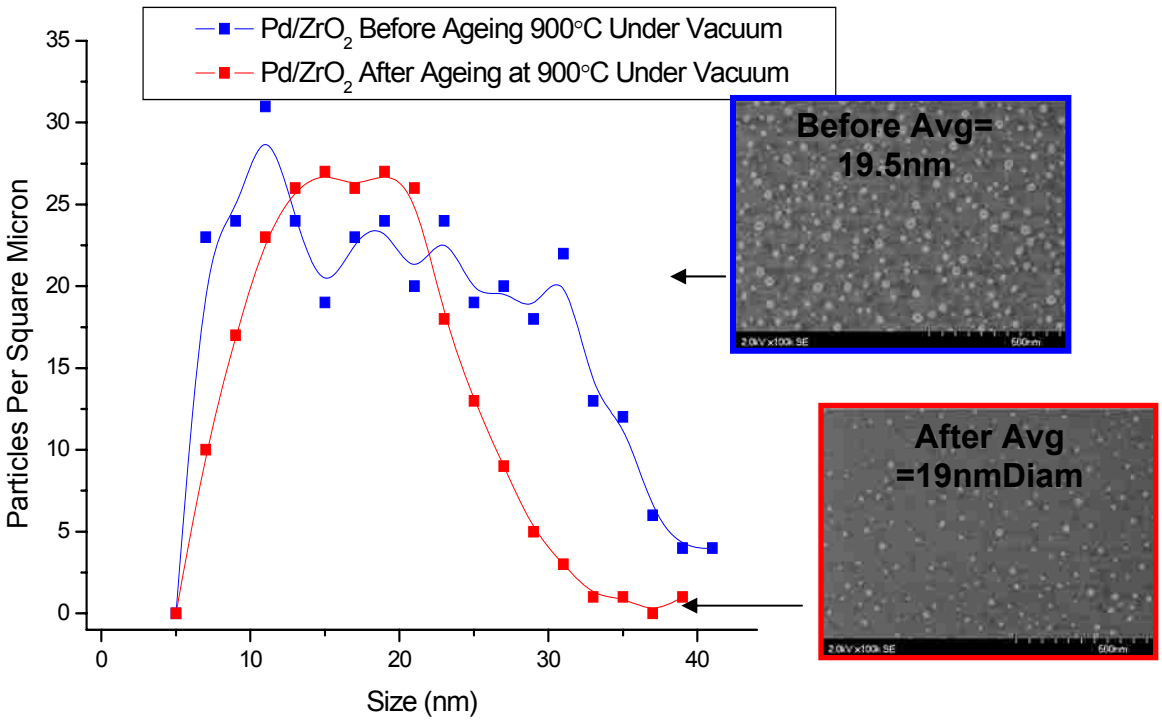

Figure 80 A vacuum heat treatment to 900°C under N_2 on a model Pd/ZrO_2 sample. The average size was not seen have a large change, but particle density and actual particle count was measured to decrease.

Our evaporation model did not accurately predict the loss of Pd on ZrO_2 for the 30 minutes it was aged. The model, similar to the Al_2O_3 prediction, under predicted the amount of metal loss. There was also difficulty in fitting the data, as the particles made showed a wide distribution of particle sizes with no distinct fitting shape. Although the model did not accurately predict the metal lost, the loss wasn't as dramatic as seen on Al_2O_3. Giving a relation that particle evaporation (i.e. diffusion) was not as pronounced on ZrO2 then on Al_2O_3 and also that the sintered particle size was much larger on Al_2O_3 compared to ZrO_2 gives a clue that particle diffusion transfer and diffusion is the most likely route for Ostwald Ripening.

Table 4 Values used for modeling the rate of Palladium evaporation.

Constants for Model	Value	Units
M	106.42	**g/mol**
R	8.3144	**J/mol*K**
T	1173.15	**K**
p*	6.35E-08	**Torr**
Ω	0.0147	**nm^3**
γ	4.797424416	**J/m^2**
k	1.381E-23	**m^2-kg/s^2-K**
ρ	1.2023E-20	**kg/nm^3**

Appendix A.2 Powder Pd/Al_2O_3 Promoted with La

Heat treatments and microscopy characterization was also carried out on an additional Pd/Al_2O_3 (gamma) catalyst promoted with La courtesy of Karl Karas at Delphi. The characterization followed the reducing heat treatments from 300°-900°C in H_2 with balance N_2. The resulting size distributions revealed only small change in average particle size over reducing heat treatments from 300°-700°C, with a large change seen at a reduction temperature of 900°C (table below).

Table 5 Size and Reduction temperature for Pd-Al_2O_3 with an added Lanthanum promoter.

Pd/Al_2O_3 Sample	Reduction Temperature	Average Particle Size
ejpred007	300	2.9
ejpred009	400	3.1
ejpred015	500	2.9
ejpred016	600	2.9
ejpred023	700	3.1
ejpred022	800	3.9
ejpred011	900	10

By using ACEM at ORNL, we were able to see single atomic species on the Al_2O_3 support (in figure below) even after the heat treatment at 900°C. The added La is seen to significantly reduce the rate of sintering, as compared to our Pd/Al_2O_3 catalyst seen in chapter 3. A conclusive result on why La has this affect on the Pd or the Al_2O_3 is still under investigation.

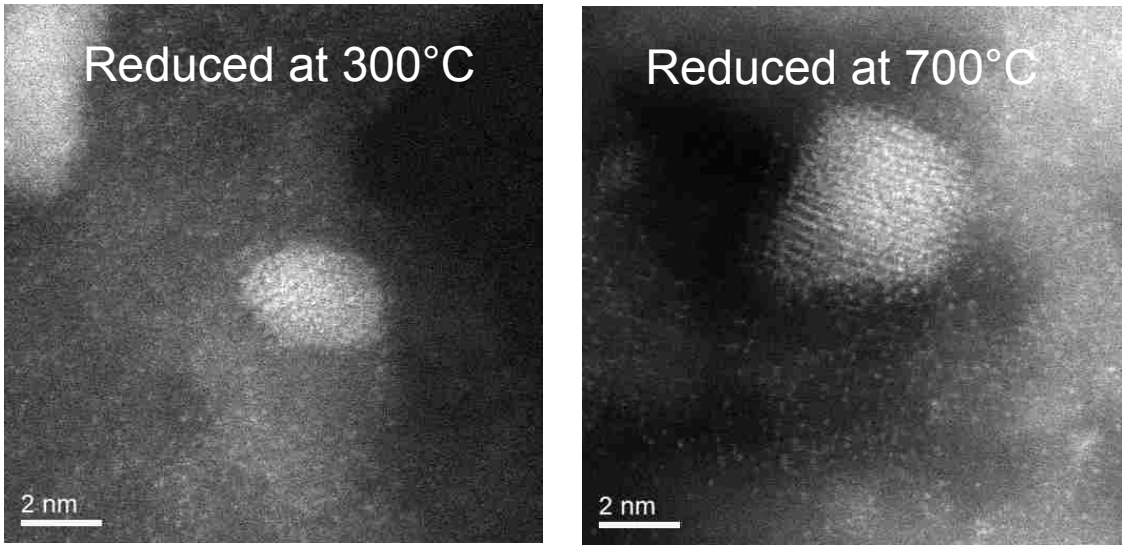

Figure 81 ACEM image taken at ORNL of the Pd/Al_2O_3 reduced at 300°C (left) and at 700°C (right). The La promoted catalyst is assumed to be the atomic species imaged on the support.

Appendix B: Chapter 4

Appendix B.1 5wt%Pt-2.5wt%Mo/Norit Carbon

Additional studies were performed with various Pt-M (M=metals) on carbon supports to answer the question if this highly dispersed species was only the result of Re being present. It was found when Molybdenum was used instead of Re, the end result was similar.

2.5wt% Mo and 5wt% Pt were deposited on Norit carbon. The sample was then reduced and passivated under similar conditions to that of the PtRe on Norit. The imaging and EDS analyses were performed in a similar manner to that of the 10wt%PtRe on Norit utilizing the same characterization techniques and capabilities. The sample was seen to have a highly dispersed species with the average particle size ~1.6nm as shown in the figure below.

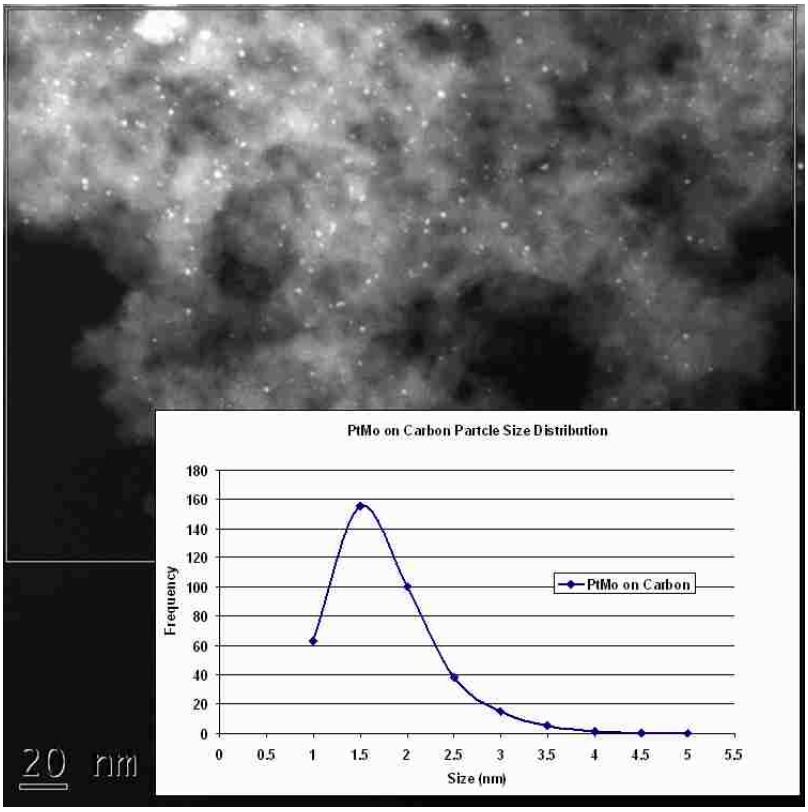

Figure 82 STEM image taken at the University of New Mexico of 5wt%Pt-2.5wt%Mo on Norit Carbon after being reduced and passivated. The average particle size was ~1.6nm with Log-Normal type PSD, similar to the10wt% PtRe on Norit Carbon discussed in chapter 4.

When the sample was analyzed using EDS, it was found that a low magnification with a broad beam that the sample contained many elements including Cl, Ca, and S. This was not surprising as the carbon itself contained Sulfur by itself already.

Table 6 EDS results for 5wt%Pt-2.5wt%Mo on Norit Carbon performed at low magnification in TEM mode. The sample contains many elements, but the overall average ratio for the Pt:Mo is 2:1 in wt% as initially deposited.

Element	Weight%	Atomic%
C K	87.31	94.83
O K	3.69	3.01
Mg K	0.12	0.06
Si K	1.3	0.61
S K	0.47	0.19
Cl K	0.2	0.07
K K	0.02	0.01
Ca K	0.48	0.16
Fe K	0.07	0.02
Cu K	3.86	0.79
Mo K	1.34	0.18
Pt L	1.15	0.08
Totals	100	

Average for Overall Analysis	
Element	**Weight%**
C	94.30
Mo	1.83
Pt	3.87

EDS performed at higher magnifications in STEM mode revealed a dispersion similar to that of the PtRe on Norit discussed in chapter 4. The particles appeared to be mainly composed of Pt with a small amount of Mo where areas of just the support revealed almost no or little Pt, with a consistent amount of Mo.

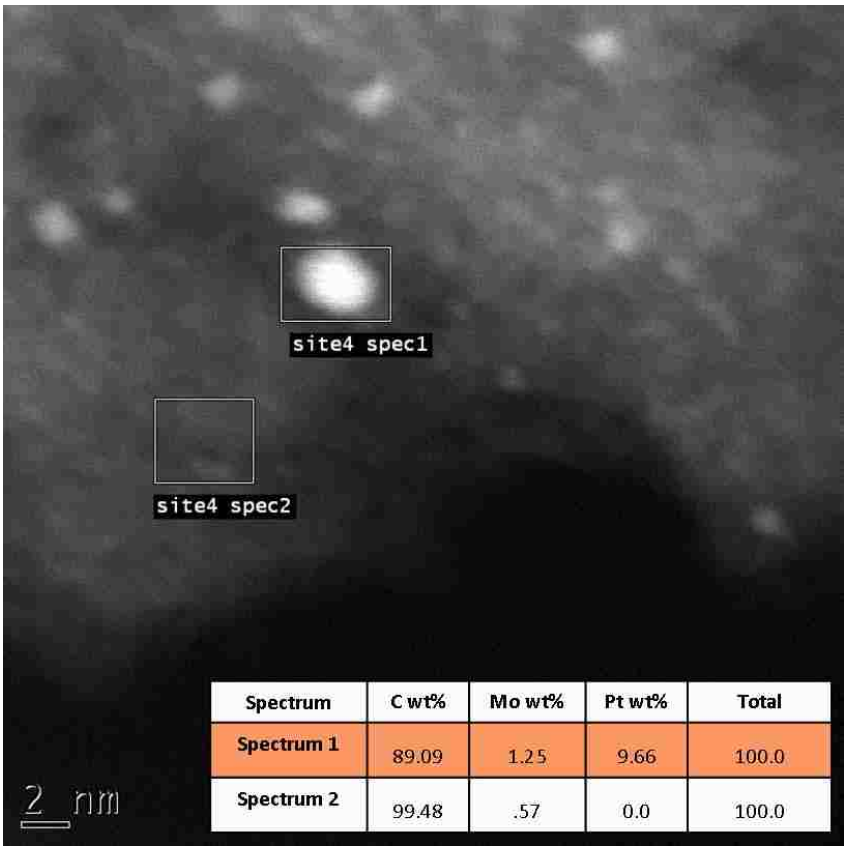

Spectrum	C wt%	Mo wt%	Pt wt%	Total
Spectrum 1	89.09	1.25	9.66	100.0
Spectrum 2	99.48	.57	0.0	100.0

Figure 83 STEM and EDS analysis of 5wt%Pt-2.5wt%Mo on Norit Carbon after being reduced and passivated. The particles are seen to be rich in Pt with some Mo, while the support by itself is seen only to contain Mo.

Particles in different regions of support revealed the same type of compositional species compared to various agglomerates. Particles are Pt rich with Mo, and areas void of particles tend to have Mo and little or no Pt.

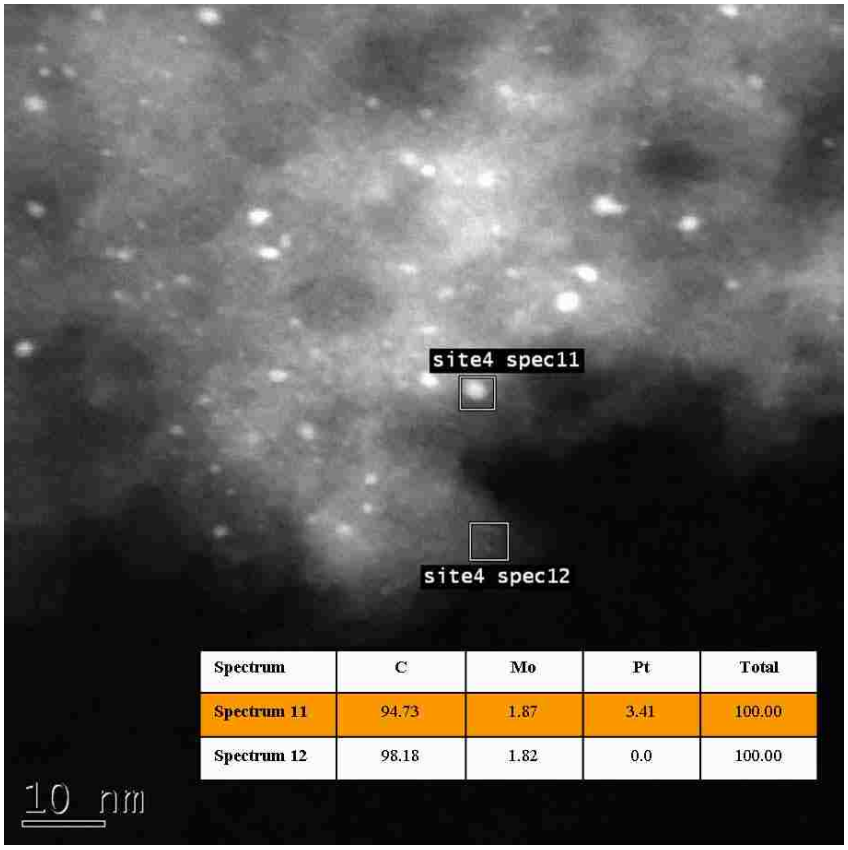

Spectrum	C	Mo	Pt	Total
Spectrum 11	94.73	1.87	3.41	100.00
Spectrum 12	98.18	1.82	0.0	100.00

Figure 84 Additional STEM and EDS analysis of 5wt%Pt-2.5wt%Mo on Norit Carbon. The particles are again seen to be rich in Pt with some Mo, while the support by itself is seen only to contain Mo.

The PtMo on Norit was similar to PtRe on Norit in that the Pt-M (metal) on the support was highly dispersed on the support while the Pt agglomerated into particles with a small amount of the added metal, M. Further analysis performed using the ACEM at ORNL confirmed the presence of atomic species on the support that could not be resolved with the microscope at UNM.

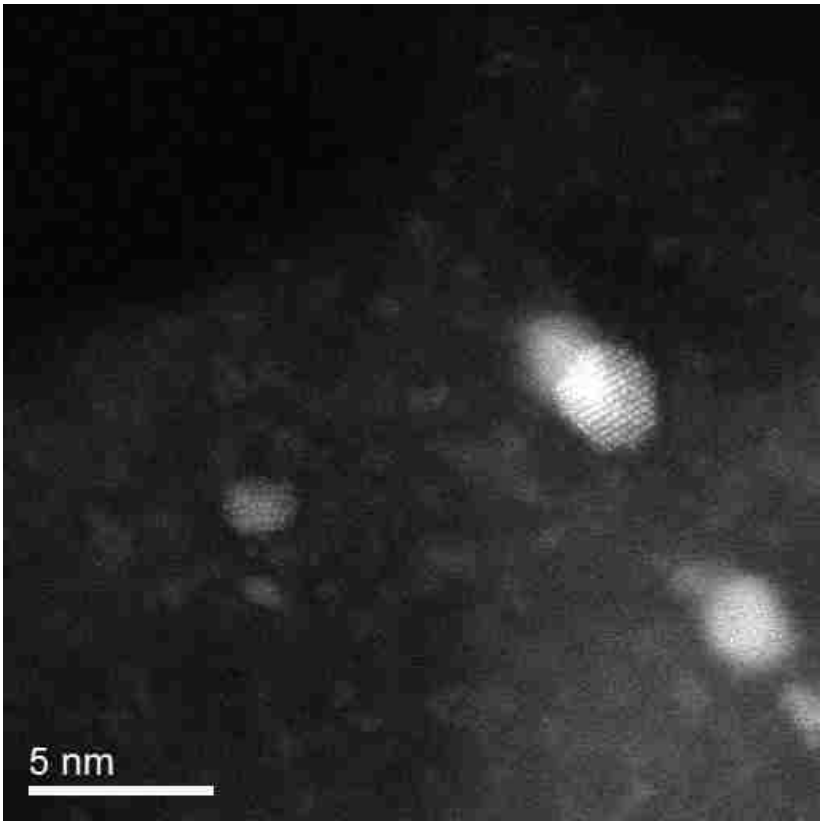

Figure 85 ACEM image taken at ORNL using the JEOL 2200FS. The image reveals small atomic species homogeneously spread all over the Norit carbon. The larger particles are mostly made of Pt.

With data from both microscopes it is evident that the dispersed species is Mo, similar to the dispersed Re species seen on our PtRe on Norit samples. The results provide further evidence that the Norit Carbon structure can highly disperse atomic species utilizing numerous amounts of atomic adsorption sites.

Appendix B-2 10wt%PtFe on Carbon

A 10wt% PtFe on Carbon was analyzed to determine if the different Carbon support structure would provide similar dispersed species. Additional analysis was also performed on the imaged PtFe particles to determine if a oxide was present that may provide enhancements during catalytic reactions.

This sample was made via evaporative impregnation of a acetone/ethanol solution of $Fe(NO_3)_2$ and H_2PtCl_6 on a pre-treated, acetylene derived carbon black. The carbon black was first pretreated by partial combustion in a muffle furnace. After the evaporation of the solvent, the catalyst was dried at 100°C and then reduced in H_2 at 450°C and passivated with 2% O_2 in He. No pre-treatments at reaction conditions were performed. Images (dark field images) were put through processing (smoothing) and lattice spacings were measured by producing individual FFT of the measured particle.

The carbon black showed graphite planes in an onion like structure. Overall, at low magnification the sample distributed particles similar to that of the Vulcan Carbon, with particles agglomerating at the edges of larger carbon particles (outer "onion"). Higher magnification images were generally taken from the particles at the edge since their surfaces could be clearly seen. The overall number average of the particle size was measured to be ~2.3nm.

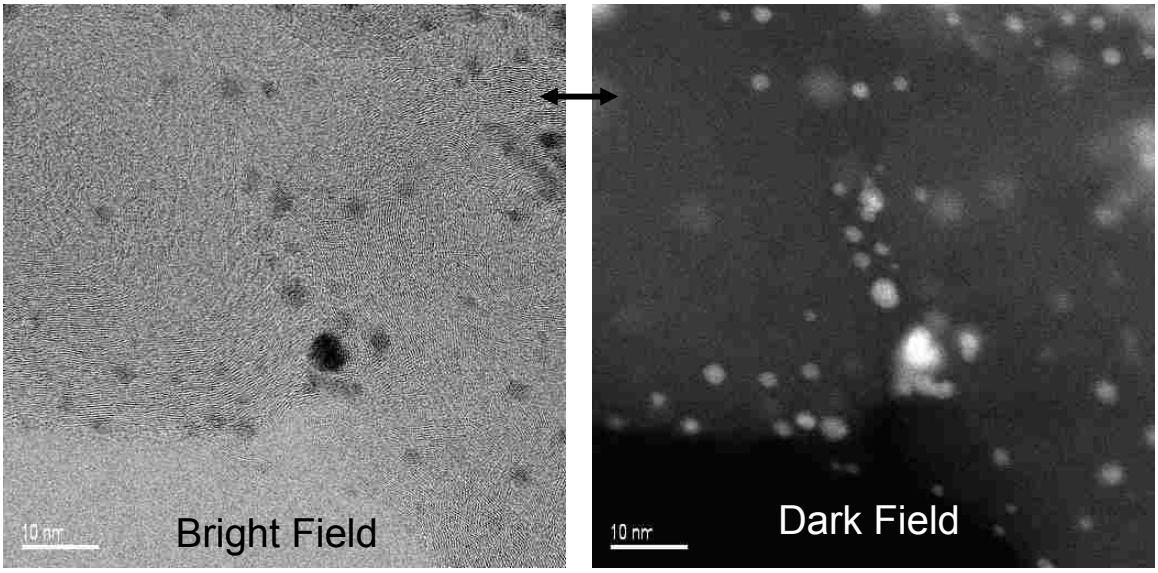

Figure 86 ACEM images taken at ORNL of 10wt%PtFe on Carbon. The left bright field image provides structural information about the carbon while the right dark field image gave good particle count statistics.

Similar to the structures seen in chapter 4, the more structured Norit contained a more uniform highly dispersed atomic species while this sample did not, similar to the PtRe on Vulcan, did not.

At higher magnifications, we were able to see characteristic layers on the surface of particles. This layer did not appear to be amorphous carbon, which can be often found on the surface of metal particles from contamination due to hydrocarbons in the vacuum. These over layers are partially crystalline and resemble passivation layers on iron F-T catalysts. The smaller ($\leq$ 3nm) particles directly on the carbon support (not in profile view) proved difficult to image due to the carbon support graphite lattice fringes that dominated the bright field images

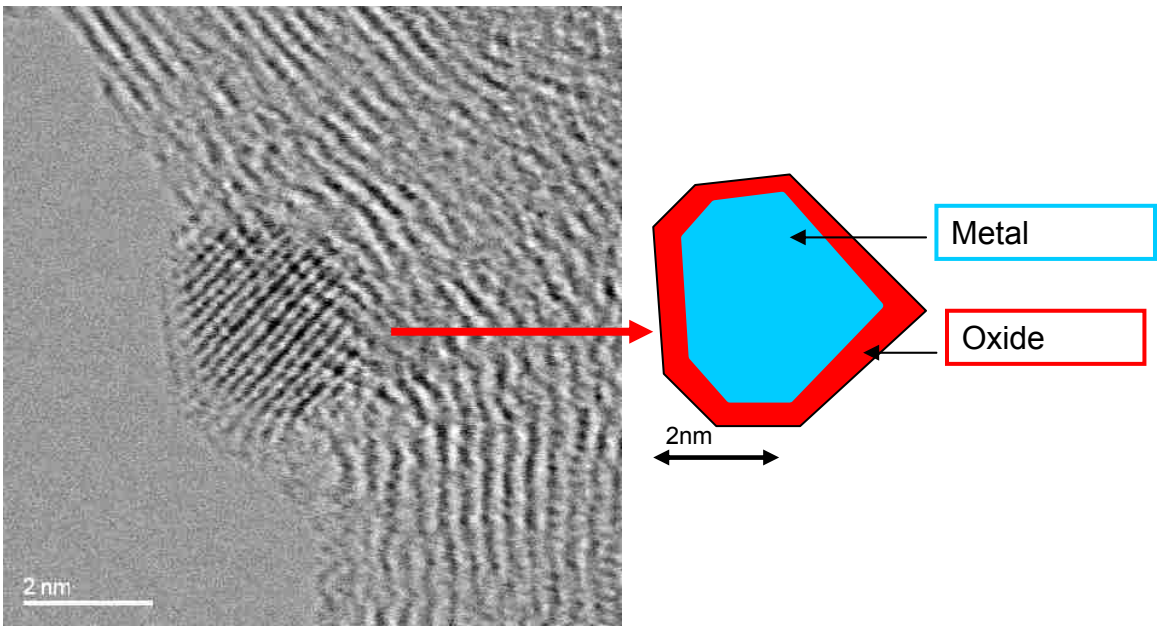

Figure 87 Left is a bright field image taken with the ACEM at ORNL. An oxide layer is present surrounding the particle. Right is a drawing further enhancing the contrast seen in the image. The oxide layer is thin and has the same contours as the particle.

Particle analysis was also performed to determine the type of crystalline structures the particles were forming in order to give evidence that the particles were mostly composed of Pt, Fe, or both forming a true bimetallic. Images captured showed evidence that a mixture of all these particles existed over the entire support.

. Dark field images clearly showed the metallic particles as well as the internal structure. Note that the different internal structure between the various particles may indicate the presence of PtFe intermetallic structures. Some particles would show no internal structure as they were out of focus, due to the limited depth of focus of the microscope. Various larger particles (~4nm) had an area of higher contrast (~1nm)

typically not in the center of the particle, an example of that can be seen in the figures below.

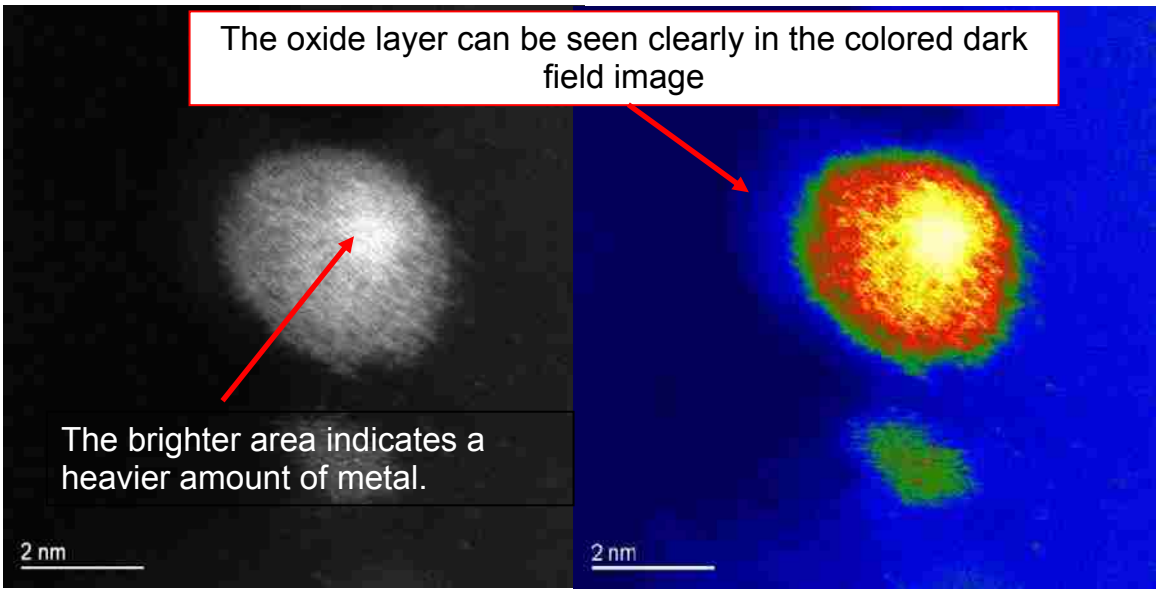

Figure 88 ACEM dark field mage taken of a particle at an edge that shows clearly a dense core, presumably Pt, possibly surrounded by a PtFe shell. The right enhanced dark field image shows the surface layer (presumably iron oxide).

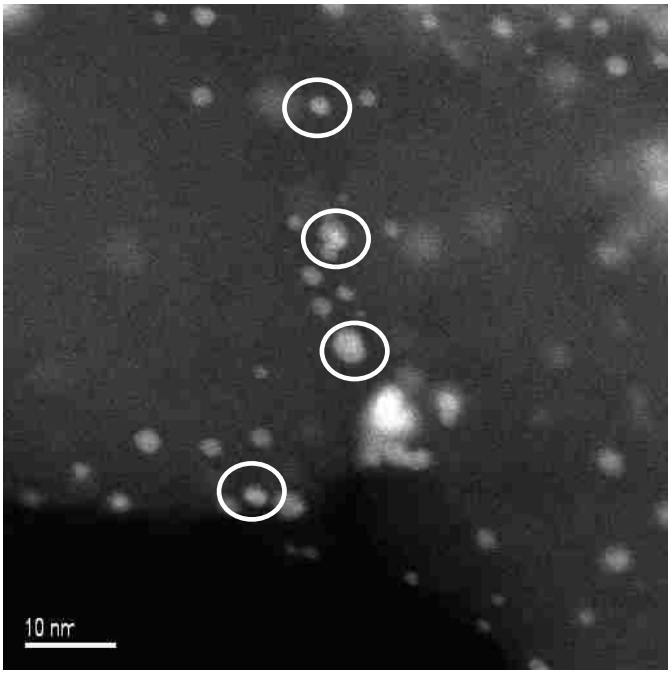

Figure 89 Many PtFe core shell particles were found on the carbon support. The circled particles were all of the core shell type.

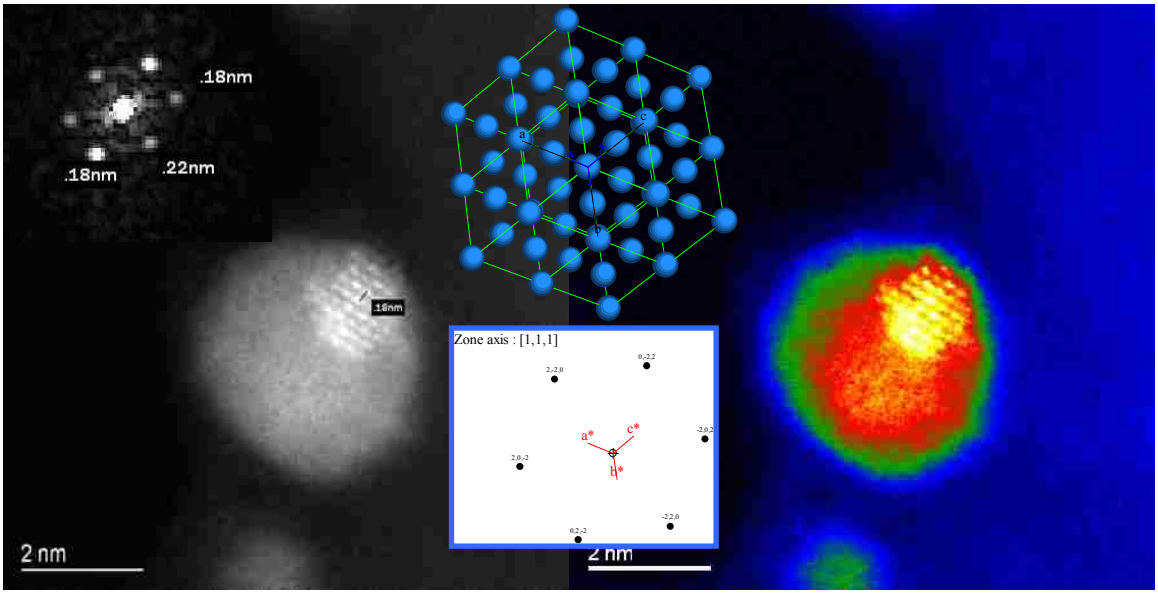

Figure 90 Due to the small focus of the probe, the structure of the core was imaged. Notice how the surrounding layer is out of focus. The inner structure is matching an FCC Pt structure viewed down the [1,1,1] zone axis.

It was found that the lattice spacings were similar to that of Pt FCC for the internal core of the core-shell type particles. Structures with defined rows of contrast were also imaged on the support (seen below). These structures were also measured to be FCC like[67], but the distinct differences in contrast has led to the belief that they are intermetallic with rows of Pt and Fe giving the particles their unique contrast.

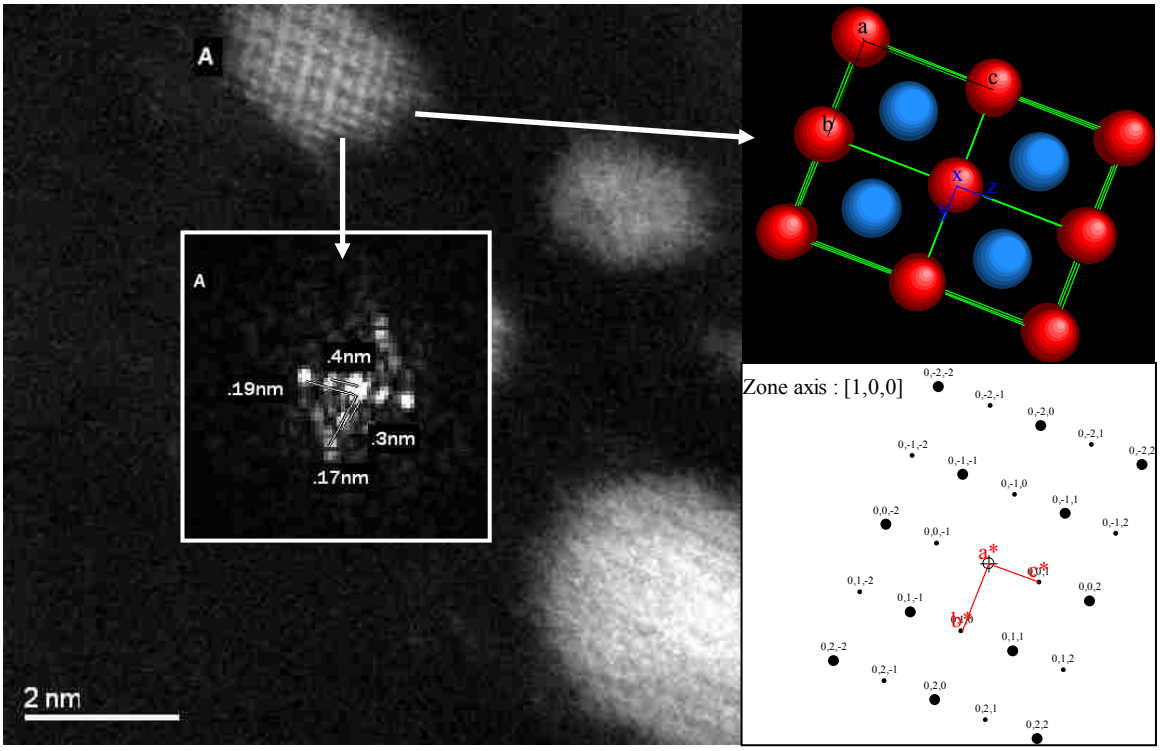

Figure 91 ACEM dark field image of a PtFe particle on carbon. The particle structure has distinct rows of contrast, indicating that it cannot be just one metal.

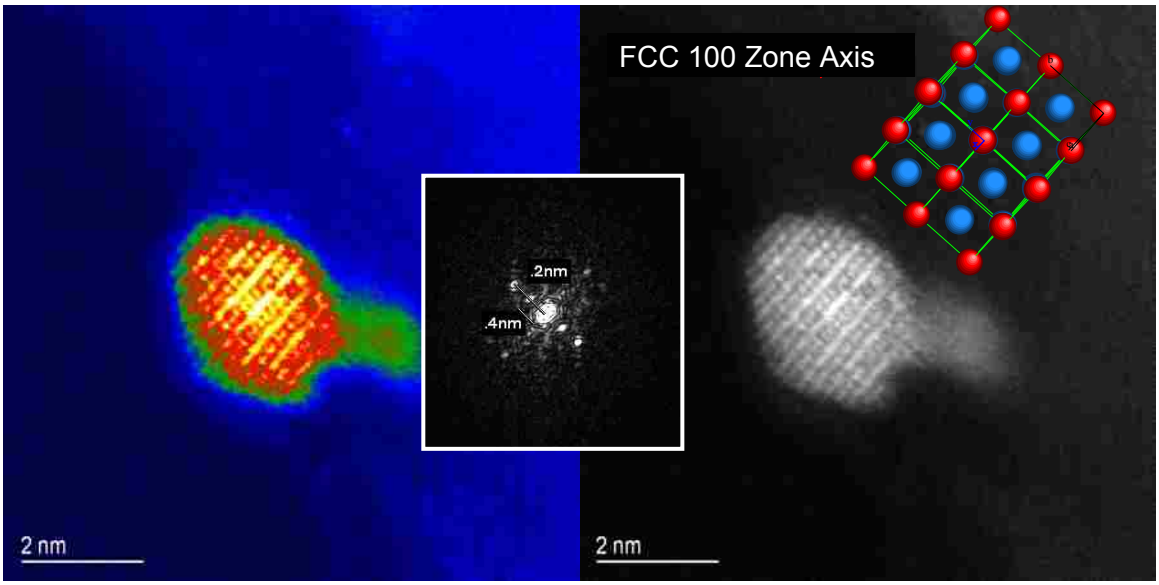

Figure 92 An additional PtFe particle reveals two different layers of contrast in the dark field image. The spacing is similar to an FCC structure.

The information obtained revealed the carbon structure was not as highly dispersed as the other Pt-M (metals) found on the Norit Carbon. This is due to the more graphitic structure of the carbon used. Additional particle analysis revealed an oxide layer surrounding the PtFe particles which did appear to be amorphous, providing evidence that the oxide can be Fe-Oxide. Due to the capabilities of the high resolution ACEM, we were able to identity distinct rows of contrast in numerous PtFe particles, revealing the nature of the intermetallic. The presence of both the oxide layer and intermetallic structure of the particles may aid in a reaction, especially in the water-gas shift reaction. Further characterization studies could be performed on this catalyst after reaction to determine if these species are stable, and whether or not the oxide or intermetallic remains.

Appendix C: Chapter 5

Grid Heating in In-Situ Studies

An additional heating problem may also be analyzed in the future to confirm that the correct temperatures are being measured. Evidence (grid images below) has shown that there is a temperature gradient across the TEM grids while heating under our desired conditions. Future work could be done on determining the actual grid temperature throughout the experiment. So far, experimentally, two 50 mesh TEM grids have been used to sandwich the sample grid instead of the normal single spacer ring above the sample grid. This has helped in distributing the heat from the outside of the grid (where the heat is generated) to the interior. This does not seem to have interfered with our experiments so far, as the temperature needed can endure an error up to 1-2°C.

Figure 93 Optical microscope image of TEM grids after experiments of Ni/$MgAl_2O_4$ heated to 750°C at 1:1 H_2:H_2O 3.6mbar. The left grid is from an experiment using the spacer ring, while the grid on the right used the two 50 mesh grids.

References

1 Chorkendorff, I. and Niemantsverdriet, J.W. *Concepts of modern catalysis and kinetics*. (Wiley-VCH, Weinheim, 2007).

2 Froment, G.F. and Waugh, K.C. Dynamics of surfaces and reaction kinetics in heterogeneous catalysis : proceedings of the international symposium, Antwerp, Belgium, September 15-17, 1997. (Elsevier, Amsterdam; New York.

3 Lifshitz, I.M. and Slyozov, V.V. THE KINETICS OF PRECIPITATION FROM SUPERSATURATED SOLID SOLUTIONS. *Journal of Physics and Chemistry of Solids*, 1961, **19**(1-2), 35-50.

4 Gruber, E.E. CALCULATED SIZE DISTRIBUTIONS FOR GAS BUBBLE MIGRATION AND COALESCENCE IN SOLIDS. *Journal of Applied Physics*, 1967, **38**(1), 243-&.

5 Somorjai. *Principles of Surface Chemistry*, 114.

6 Chakraverty, B.K. Grain Size Distribution in Thin Films-1. Conservative Systems. *Journal of Physics and Chemistry of Solids*, 1967, **28**, 2401-2412.

7 Wynblatt, P. and Gjostein, N.A. Supported metal crystallites. *Progress in Solid State Chemistry*, 1975, **9**, 21.

8 Wynblatt, P. PARTICLE GROWTH IN MODEL SUPPORTED METAL-CATALYSTS .2. COMPARISON OF EXPERIMENT WITH THEORY. *Acta Metallurgica*, 1976, **24**(12), 1175-1182.

9 Granqvist, C.G. and Buhrman, R.A. Ultrafine metal particles. *Journal of Applied Physics*, 1976, **47**(5), 2200-2219.

10 Wanke, S.E. SINTERING MECHANISM OF SUPPORTED METAL-CATALYSTS. *Journal of Catalysis*, 1977, **46**(2), 234-237.

11 Flynn, P.C. and Wanke, S.E. MODEL OF SUPPORTED METAL CATALYST SINTERING .1. DEVELOPMENT OF MODEL. *Journal of Catalysis*, 1974, **34**(3), 390-399.

12 Flynn, P.C. and Wanke, S.E. MODEL OF SUPPORTED METAL CATALYST SINTERING .2. APPLICATION OF MODEL. *Journal of Catalysis*, 1974, **34**(3), 400-410.

13 Granqvist, C.G. and Buhrman, R.A. *Journal of Catalysis*, 1977, **46**, 238.

14 Richardson, J.T. and Crump, J.G. Crystallite size distributions of sintered nickel catalysts. *Journal of Catalysis*, 1979, **57**(3), 417-425.

15 Bartholomew, C.H. and SORENSEN, W.L. SINTERING KINETICS OF SILICA-SUPPORTED AND ALUMINA-SUPPORTED NICKEL IN HYDROGEN ATMOSPHERE. *Journal of Catalysis*, 1983, **81**(1), 131-141.

16 Sehested, J., Carlsson, A., Janssens, T., Hansen, P. and Datye, A. Sintering of nickel steam-reforming catalysts on MgAl2O4 spinel supports. *Journal of Catalysis*, 2001, **197**(1), 200-209.

17 Sehested, J. Sintering of nickel steam reforming catalysts. *Journal of Catalysis*, 2003, **217**, 417-426.

18 Teixeira, A. and Giudici, R. Deactivation of steam reforming catalysts by sintering: experiments and simulation. pp. 3609-3618 (Pergamon-Elsevier Science Ltd, 1999).

19 Teixeira, A. and Giudici, R. A Monte Carlo model for the sintering of Ni/Al2O3 catalysts. pp. 789-798 (Pergamon-Elsevier Science Ltd, 2001).

20 **Lee, H.H.** KINETICS OF SINTERING OF SUPPORTED METAL-CATALYSTS - THE MECHANISM OF ATOM DIFFUSION. *Journal of Catalysis*, 1980, **63**(1), 129-137.
21 **Datye, A.K., Xu, Q., Kharas, K.C. and McCarty, J.M.** Particle size distributions in heterogeneous catalysts: What do they tell us about the sintering mechanism? , pp. 59-67 (Elsevier Science Bv, 2006).
22 **Kaganovskii, Y.S., Beke, D.L. and Yurchenko, S.P.** SHIFT OF THE BOUNDARY OF A BEADED THIN-FILM CAUSED BY EVAPORATION. *Surface Science*, 1995, **339**(1-2), 233-240.
23 **Goeke, R.S. and Datye, A.K.** Model oxide supports for studies of catalyst sintering at elevated temperatures. *Topics in Catalysis*, 2007, **46**(1-2), 3-9.
24 **Herrera-Zaldivar, M., Valenzuela-Benavides, J. and Pal, U.** Coalescence of palladium nanoparticles assembled on carbon and SiC surfaces: STM and STS studies. pp. 144-149 (Elsevier Science Bv, 2006).
25 **Baker, R.T.K., Harris, P.S. and Thomas, R.B.** Direct Observation of Particle Mobility On A Surface In A Gaseous Environment. *Surface Science*, 1974, **46**, 311.
26 **Baker, R.T.K., Thomas, C. and Thomas, R.B.** CONTINUOUS OBSERVATION OF PARTICLE-SIZE BEHAVIOR OF PLATINUM ON ALUMINA. *Journal of Catalysis*, 1975, **38**(1-3), 510-513.
27 **Bithell, E.G., Doole, R.C. and Goringe, M.J.** ON THE EXTRACTION OF HIGH-QUALITY DATA FROM REAL-TIME TRANSMISSION ELECTRON-MICROSCOPY EXPERIMENTS. pp. 172-183 (Elsevier Science Bv, 1994).
28 **Hansen, T.W.** Sintering and Particle Dynamics in Supported Metal Catalysts. *Ph.D. Thesis*, 2006.
29 **Williams, D.B. and Carter, C.B.** *Transmssion Electron Microscopy*. 1996).
30 **Wagner, J.B.** In situ transmission electron microscopy of catalyst particles. *NBIfAPG* (University of Copenhagen, 2002).
31 **Liu, J.Y.** Scanning transmission electron microscopy and its application to the study of nanoparticles and nanoparticle systems. *Journal of Electron Microscopy*, 2005, **54**(3), 251-278.
32 **Hetherington, C.** Aberration correction for TEM. *Materials Today*, 2004, **7**(12), 50-55.
33 **Topsoe, H.** Developments in operando studies and in situ characterization of heterogeneous catalysts. *Journal of Catalysis*, 2003, **216**(1-2), 155-164.
34 **Boyes, E.D. and Gai, P.L.** Environmental high resolution electron microscopy and applications to chemical science. *Ultramicroscopy*, 1997, **67**(1-4), 219-232.
35 **Scott, R.W.J., Datye, A.K. and Crooks, R.M.** Bimetallic palladium-platinum dendrimer-encapsulated catalysts. *Journal of the American Chemical Society*, 2003, **125**(13), 3708-3709.
36 **Chorkendorff, P.D.I. and Niemantsverdriet, P.D.J.W.** Front Matter. *Concepts of Modern Catalysis and Kinetics*, pp. i-xvii2005).
37 **Langmuir, I.** The vapor pressure of metallic tungsten. *Physical Review*, 1913, **2**(5), 329-342.
38 **Campbell, C.T., Parker, S.C. and Starr, D.E.** The effect of size-dependent nanoparticle energetics on catalyst sintering. *Science*, 2002, **298**(5594), 811-814.

39 Sehested, J., Gelten, J.A.P., Remediakis, I.N., Bengaard, H. and Norskov, J.K. Sintering of nickel steam-reforming catalysts: effects of temperature and steam and hydrogen pressures. *Journal of Catalysis*, 2004, **223**(2), 432-443.
40 Harris, D.J., Young, D.J. and Trimm, D.L. THE SINTERING OF ALUMINA BASED CATALYSTS. *Abstracts of Papers of the American Chemical Society*, 1983, **185**(MAR), 62-INDE.
41 Choma, J., Burakiewicz-Mortka, W., Jaroniec, M., Li, Z. and Klinik, J. Monitoring changes in surface and structural properties of porous carbons modified by different oxidizing agents. *Journal of Colloid and Interface Science*, 1999, **214**(2), 438-446.
42 Aksoylu, A.E., Faria, J.L., Pereira, M.F.R., Figueiredo, J.L., Serp, P., Hierso, J.C., Feurer, R., Kihn, Y. and Kalck, P. Highly dispersed activated carbon supported platinum catalysts prepared by OMCVD: a comparison with wet impregnated catalysts. *Applied Catalysis a-General*, 2003, **243**(2), 357-365.
43 Xie, J.N., Zhang, N.Y. and Varadan, V.K. Functionalized carbon nanotubes in platinum decoration. pp. S5-S8 (Iop Publishing Ltd, 2006).
44 Wang, Y., Xu, X., Tian, Z.Q., Zong, Y., Cheng, H.M. and Lin, C.J. Selective heterogeneous nucleation and growth of size-controlled metal nanoparticles on carbon nanotubes in solution. *Chemistry-a European Journal*, 2006, **12**(9), 2542-2549.
45 Schlogl, R. Carbons. *Handbook of Heterogeneous Catalysis*, 2008, **2**, 122.
46 Suzuki, H. Experimental Evidence of Stability of Pt Clusters on and in Carbon Particles. *Japanese Journal of Applied Physics*, 2005, **44**(19), 3.
47 Kunkes, E.L., Simonetti, D.A., Dumesic, J.A., Pyrz, W.D., Murillo, L.E., Chen, J.G. and Buttrey, D.J. The role of rhenium in the conversion of glycerol to synthesis gas over carbon supported platinum-rhenium catalysts. *Journal of Catalysis*, 2008, **260**(1), 164-177.
48 Kunkes, E.L., Soares, R.R., Simonetti, D.A. and Dumesic, J.A. An integrated catalytic approach for the production of hydrogen by glycerol reforming coupled with water-gas shift. *Applied Catalysis B: Environmental*, 2009, **90**(3-4), 693-698.
49 Soares, R.R., Simonetti, D.A. and Dumesic, J.A. Glycerol as a Source for Fuels and Chemicals by Low-Temperature Catalytic Processing13. *Angewandte Chemie International Edition*, 2006, **45**(24), 3982-3985.
50 Nichols, G., Byard, S., Bloxham, M.J., Botterill, J., Dawson, N.J., Dennis, A., Diart, V., North, N.C. and Sherwood, J.D. A review of the terms agglomerate and aggregate with a recommendation for nomenclature used in powder and particle characterization. *Journal of Pharmaceutical Sciences*, 2002, **91**(10), 2103-2109.
51 Corporation, C.
52 Fachini, E.R., Diaz-Ayala, R., Casado-Rivera, E., File, S. and Cabrera, C.R. Surface Coordination of Ruthenium Clusters on Platinum Nanoparticles for Methanol Oxidation Catalysts. *Langmuir*, 2003, **19**(21), 8986-8993.
53 Trzebiatowski, W. *Bull. Acad. Pol. Sci. Ser. Sci. Chim.*, 1954, **2**(37).
54 Okamoto, H. Binary Alloy Phase Diagrams. 1990, **2**.
55 Gontard, L.C., Dunin-Borkowski, R.E., Gass, M.H., Bleloch, A.L. and Ozkaya, D. Three-dimensional shapes and structures of lamellar-twinned fcc nanoparticles using ADF STEM. *Journal of Electron Microscopy*, 2009, **58**(3), 167-174.

56 Kunkes, E.L. Reaction and Characteriztion Studies of the Conversion of Biomass-Derived Carbohydrates on Supported Metal Catalysts. *Ph.D. Thesis*, 2009.
57 Helfensteyn, S. and Creemers, C. Preferential segregation to the step edges on Pt-Re catalyst particles. *Surface Science*, 2002, **507-510**, 783-788.
58 Guofeng, W., Van Hove, M.A., Ross, P.N. and Baskes, M.I. Monte Carlo simulations of segregation in Pt-Re catalyst nanoparticles. *Journal of Chemical Physics*, pp. 5410-5422 (American Institute of Physics, 2004).
59 Rostrup-Nielsen, J.R., Sehested, J. and Norskov, J.K. Hydrogen and synthesis gas by steam- and CO2 reforming. *Advances in Catalysis, Vol 47*, pp. 65-139 (Academic Press Inc, San Diego, 2002).
60 Bromfield, T.C. and Vosloo, A.C. Recent advances in the development of Fischer-Tropsch catalysts at Sasol. pp. 29-34 (Wiley-V C H Verlag Gmbh, 2003).
61 D.O.E., B.E.S.A.C.a.U.S. Basic Research Needs to Assure a Secure Energy Future. *Report*, 2003, **February**.
62 Sehested, J., Gelten, J.A.P. and Helveg, S. Sintering of nickel catalysts: Effects of time, atmosphere, temperature, nickel-carrier interactions, and dopants. *Applied Catalysis a-General*, 2006, **309**(2), 237-246.
63 Liu, R.J., Crozier, P.A., Smith, C.M., Hucul, D.A., Blackson, J. and Salaita, G. In situ electron microscopy studies of the sintering of palladium nanoparticles on alumina during catalyst regeneration processes. pp. 77-85 (Cambridge Univ Press, 2004).
64 Challa, S.R., 2009.
65 Vesborg, P. Studies of Cu/ZnO-based catalysts under methanol synthesis conditions. *Ph.D. Thesis*, 2006.
66 Hansen, P.L., Wagner, J.B., Helveg, S., Rostrup-Nielsen, J.R., Clausen, B.S. and Topsøe, H. Atom-Resolved Imaging of Dynamic Shape Changes in Supported Copper Nanocrystals. *Science*, 2002, **295**, 2053-2055.
67 Qian, Y.D., Wen, W., Adcock, P.A., Jiang, Z., Hakim, N., Saha, M.S. and Mukerjee, S. PtM/C catalyst prepared using reverse micelle method for oxygen reduction reaction in PEM fuel cells. *Journal of Physical Chemistry C*, 2008, **112**(4), 1146-1157.